Some Absorbing Examples

Of The

Ionospheric Effects Of Solar Phenomena

Novel Methods, Observations, and Interpretations.

Mathew James Beharrell, MSci

A Thesis Submitted for the Degree

of Doctor of Philosophy

September 2009

Space Plasma Environment And Radio Science
Lancaster University, UK.

SOME ABSORBING EXAMPLES

OF THE

IONOSPHERIC EFFECTS OF SOLAR PHENOMENA

MATHEW JAMES BEHARRELL, MSCI

A Thesis Submitted for the Degree

of Doctor of Philosophy

SEPTEMBER 2009

Abstract

By many varied and complex means, an ever active and dynamic Sun instils disturbances in Earth's ionosphere. This thesis presents examples of effects driven by solar electromagnetic radiation, and by the solar wind.

In the first of three pieces of work a method of inversion provides the effective collision frequency profile in the D-region, from a combination of incoherent scatter radar, and riometer data. The deduced collision frequency above EISCAT, Tromsø, for a period in November 2004, matches with that calculated using NRLMSISE-00, during both active (ap > 50), and quiet (ap < 50) conditions. Additionally, the validity of using the Appleton-Hartree equation with effective collision frequencies is confirmed for the calculation of absorption at high frequencies.

The second study concerns the ionospheric effect of a large solar flare. Measurements of X-ray flux from the GOES satellite are fitted to a semi-empirical spectrum, before being used, in combination with NRLMSISE-00, to calculate ionospheric profiles of electron production rates. The continuous slowing down method is then employed to simulate the high energy electron distribution function in the D-region. It is found that the increase in cosmic radio wave absorption during flare events is a result of the enhanced ionization, as opposed to a change in collision frequency due to elevated electron temperatures. The production rates are introduced to the SIC model, where the resultant electron density profiles agree with D-region EISCAT observations.

In the final work, a survey of ARIES data reveals evidence for a previously overlooked generation mechanism of high azimuthal wave number magnetospheric waves. The dispersion relations of small scale precipitation pulsations, observed with m-numbers as high as 380, expose the transference of energy in its journey from solar wind dynamic pressure variations. Previous studies of magnetospheric waves, together with data from the CAMMICE (MICS) instrument aboard the Polar spacecraft, provide support for the theory.

Declaration

The research presented in this thesis is my own work, except where explicitly stated, and has not been submitted for the award of a higher degree elsewhere. Some of the results have led to publications of the following scientific papers in refereed journals:

M. Beharrell and F. Honary, (2008),

A New Method for Deducing the Effective Collision Frequency Profile in the D-Region,

J. Geophys. Res., (113), A05303, doi:10.1029/2007JA012650.

C.-F. Enell, P. T. Verronen, M. Beharrell, J. P. Vierinen, A. Kero, A. Seppälä, F. Honary, T. Ulich, and E. Turunen, (2008),

Case Study of the Mesospheric and Lower Thermospheric Effects of Solar X-Ray Flares: Coupled Ion-Neutral Modelling and Comparison With EISCAT and Riometer Measurements,

Ann. Geophys., (26), 2311-2321.

M. Beharrell, A.J. Kavanagh, and F. Honary, (2010),

On the Origin of High m Magnetospheric Waves,

J. Geophys. Res., (115), A02201, doi:10.1029/2009JA014709.

Acknowledgements

I would sincerely like to thank my supervisor Farideh Honary, computer whiz Steve Marple, the very knowledgeable Andrews (Kavanagh and Senior), technical go-to Martin Grill, and everyone, past and present, in the Space Plasma Environment and Radio Science (SPEARS) group for their friendship and help. I am very grateful, for some excellent discussions and advice, to Lisa Baddeley [EISCAT], Mike Kosch [Lancaster], Esa Turunen [SGO Aeronomy Group], Pekka Verronen [Finnish Meteorological Institute], and my examiners, Michael Denton [Lancaster], Steve Milan [Leicester], and Richard Horne [BAS]. Most importantly, for their unwavering support, I would like to thank my parents, Colin and Ann Beharrell.

Contents

List of Figures

Chapter 1

The Solar-Terrestrial Environment

An introduction to ionospheric and solar-terrestrial physics.

1.1 Introduction

A plasma is an electrically-neutral gas containing charged particles, on which the additional forces of electromagnetism can act to produce an abundance of unique and remarkable characteristics. 99% of the matter in the visible universe exists as plasma, making it an important fundamental state. However, it is not naturally occurring on the surface of Earth. The closest naturally occurring plasma is found in the upper atmosphere, where it is ionized primarily by solar ultra-violet radiation, creating a region called the ionosphere. This region, with the surrounding near-Earth environment, provide an ideal laboratory for the study of plasma processes.

1.2 The Sun and the Solar Wind

1.2.1 Our star

The Sun is a rather unremarkable star. Like most, it belongs in the main sequence, an indication that it derives its energy by nuclear fusion of hydrogen nuclei into helium. It comprises around 99.86% of the mass in the solar system and emits $3.8 \times 10^{26}\,\mathrm{W}$ of electromagnetic radiation over a broad spectral range (Woolfson, 2000). At Earth orbit (1 A.U.) this amounts to almost $1.4\,\mathrm{kW\,m^{-2}}$, about half of which reaches the Earth's surface.

The solar spectrum approximates a black body at $5780\,\text{K}$, with numerous dips corresponding to the characteristic absorption frequencies of the major species of the solar atmosphere. Thus, the Sun has a white colour, which can be given a yellow hue by scattering in the Earth's atmosphere. During solar eclipses a thin outer layer, called the chromosphere, may be observed. It extends around $2000\,\text{km}$ above the visible surface, or photosphere, with a temperature of up to $50{,}000\,\text{K}$ (Abhyankar, 1977). Beyond the chromosphere, the solar corona reaches out into interplanetary space, with no apparent termination.

1.2.2   The solar wind

Simultaneous to the electromagnetic radiation, the Sun's strong magnetic field contributes to the ejection of a continuous stream of plasma from its outer layers, with frequent bursts of highly energetic particles. The solar wind consists mostly of protons and electrons, with varying speed, temperature, and density. Slow solar wind has a velocity of 300–$400\,\text{km}\,\text{s}^{-1}$, and a temperature of $\sim 1.5 \times 10^5\,\text{K}$, whereas fast solar wind, travelling at a velocity up to $750\,\text{km}\,\text{s}^{-1}$, and on very rare occasions up to $1000\,\text{km}\,\text{s}^{-1}$ (Kivelson and Russel, 1995), has a temperature of $\sim 8 \times 10^5\,\text{K}$ (Feldman et al., 2005). The fast solar wind is typically half as dense, and more steady, when compared to its slower counterpart.

These marked differences stem from very different regions of origin on the Sun. Fast solar wind is thought to be released from regions of open field lines, known as coronal holes, and accelerated through narrow funnels by magnetic reconnection (Tu et al., 2005). Sudden bursts of fast moving plasma, known as coronal mass ejections, can travel at speeds of up to $2000\,\mathrm{km\,s^{-1}}$. These are most often associated with solar flares, and can interrupt either slow or fast solar wind, often causing geomagnetic storms on encountering the Earth.
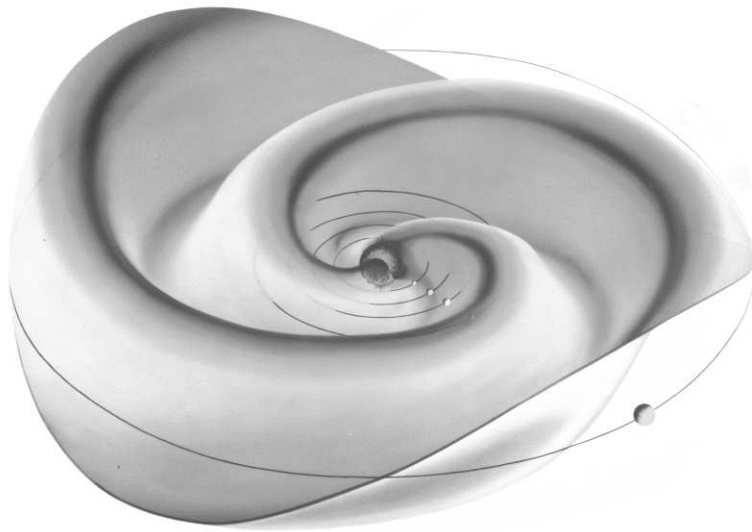
Figure 1.1: The heliospheric current sheet, including the positions of the first 5 planets (by NASA artist Werner Heil).

Regions of varying activity are scattered about the solar surface. In combination with the Sun's rotation around its axis, which has a shorter period at the equator than near the poles, this results in a periodic nature in many geophysical phenomena. One solar rotation takes 25.05 Earth days at the equator, and 34.3 days at the poles (Williams, 2004), but for geophysical purposes an average of 27 days is commonly used. The effect of the Sun's rotation on the solar wind is similar to that of a spinning garden sprinkler, and is known as the Parker spiral. Regardless of the spiral shape, the flow is in an outward direction, leading to regions of fast solar wind catching up with, and compressing, regions of slower solar wind.

The high conductivity in the solar wind plasma leads to a phenomena first introduced by Alfvén in 1942: the Sun's magnetic field is trapped within the plasma, or 'frozen in' (see e.g. Hargreaves (1992)). The magnetic field is carried with the solar wind through the solar system, where it is known as the interplanetary magnetic field (IMF). Figure 1.1 shows the related heliospheric current sheet, a surface within the solar system across which the IMF changes from inward to outward. This an important feature; when the IMF is directed southward, it can couple more readily with the Earth's magnetic field and drive substorms (Akasofu, 1964; Nakamura, 2006).

Changes in the dynamic pressure of the solar wind excite natural eigen-modes of oscillation in Earth's magnetospheric cavity, while velocity shear on the flanks of the magnetosphere can produces waves by means of the Kelvin-Helmholtz instability, predominantly at high solar wind speeds (Claudepierre, 2008). These large scale waves are investigated in chapter 5, as candidates for the driving source of small scale waves, often observed in the morning ionosphere.

1.2.3 Solar flares

The electromagnetic output of the Sun is remarkably constant at visible wavelengths, varying by less than 1% at solar maximum, the peak of the principal 11 years solar cycle. During solar minimum the variation is as little as 0.05% (Wilson et al., 1981). At shorter wavelengths this is not so. Sunspots are commonly observed throughout the solar cycle, although many more exist during solar maximum. They appear as visibly dark spots on the surface of the Sun. Within these regions, extreme amounts of energy are built up in distortions of the Sun's magnetic field, and released as solar flares in as little as a few hundred seconds. The magnitude of a flare may be classified on a scale of 1-4, according to the area of brightening when viewed in Hα light. However, since the launch of the GOES geostationary satellites, it has been common to label a flare according to the amount of X-ray radiation in the $0.1 - 0.8$ nm band, incident at $1R_E$.
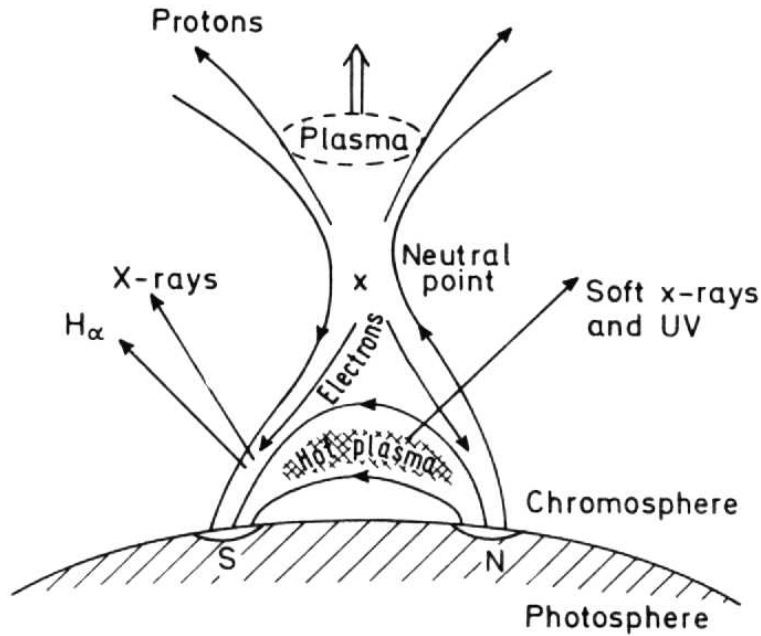
Figure 1.2: The mechanism of a solar flare, (after Piddington (1969)).

The spontaneous release of energy, typically amounting to some 10^{25}J, is primarily in highly energetic particles, with around a quarter released as electromagnetic radiation (Kopp et al., 2005). Bremsstrahlung X rays are produced as inwardly travelling electrons are decelerated by the dense chromosphere, whereas the ionization and subsequent recombination of hydrogen results in the Hα radiation, at 656.2 nm. Figure 1.2 illustrates the major processes involved. The emitted X-rays, unlike Hα radiation, have frequencies above the threshold for ionization of the major species in Earth's ionosphere, and thus contribute significantly to the ionization in the D-region. The ionospheric effect of an extremely large X-ray flare is subject of study in chapter 4.

1.3 The Magnetosphere

1.3.1 Regions of the magnetosphere

The magnetosphere is a region, close to the Earth, that is shielded from the solar wind by Earth's magnetic field. The deflection of the solar wind is due to its high conductivity, which, although responsible for freezing in the interplanetary magnetic field, acts to 'freeze out' the Earth's magnetic field. A balance exists between the solar wind dynamic pressure, and the magnetic pressure of Earth's dipole. In times of high solar wind pressure the boundary, or magnetopause, will move toward the Earth, increasing the magnetic pressure. The geocentric distance to the magnetopause varies between around 8 and $12\,R_E$, at the sub-solar point, with a typical distance of $10\,R_E$ under average solar wind conditions (Kivelson and Bagenal, 1998).

Figure 1.3 illustrates the main regions of the complex magnetosphere system. In the solar wind reference frame, the velocity of Earth is 'supersonic' with respect to any of the waves that can propagate in it. A shock front is formed at a widely varying distance from the magnetopause, which is typically 2 to $3\,R_E$, but can be significantly further at times of slow solar wind. Between the shock front and the magnetopause, in a region called the magnetosheath, the plasma is turbulent.

The polar cusps are a feature of Earth's dipole magnetic field that provide an easy entry point for particles of the solar wind. As regions that connect the magnetopause directly to the ground, they offer a pathway along which the solar wind particles do not need to cross any field lines.
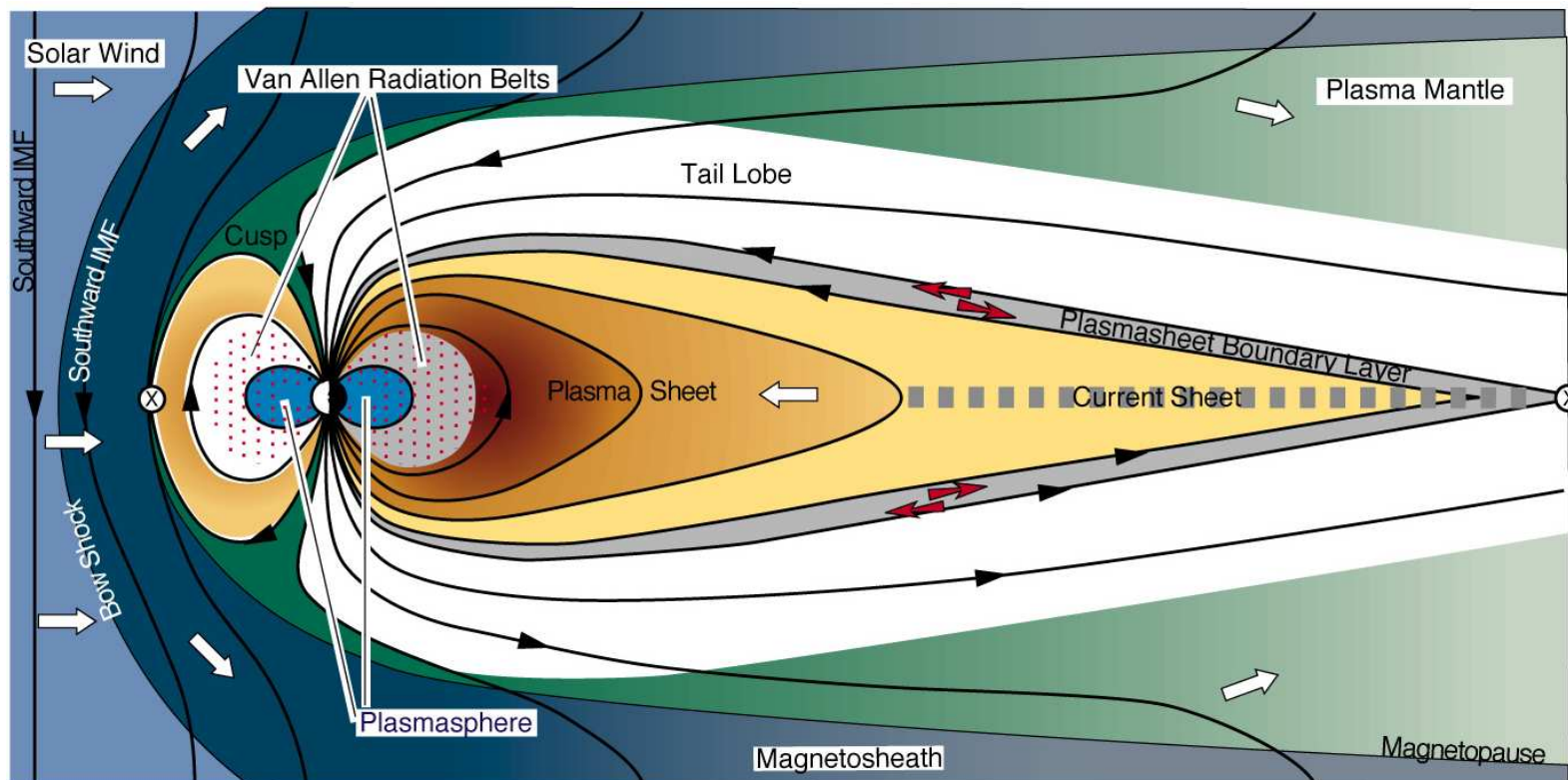
Figure 1.3: Earth's Magnetosphere, (illustration by T.W. Hill).

On the night-side, the passing solar wind stretches the magnetosphere into a long tail, or magnetotail, with a roughly circular cross section. The magnetic field in the northern lobe of the tail is directed away from the Earth, and in the southern lobe it is toward Earth. This configuration is necessarily supported by a current sheet between the lobes, with an enhanced plasma density acting to oppose the magnetic pressure of the lobes. The length of the magnetotail varies, as spontaneous reconnection events, known as substorms (see section 1.3.8), lead to the tip of the tail breaking away, and being carried off in the solar wind (Nakamura, 2006). A typical length of the tail magnetically connected to the Earth is $600R_E$ (Kivelson and Russel, 1995), however, field lines that have become disconnected have been shown to retain a tail-like geometry several thousand R_E downstream (Cowley, 1991).

Closer to Earth, ionospheric plasma at an altitude above 120 km, and predominantly on the day-side and near the poles, is capable of escaping to the magnetosphere along magnetic field lines (Barakat et al., 1987). At lower latitudes, geomagnetic field lines close within the plasmasphere, a region extending to between approximately 3 and 6 R_E at the equator, containing plasma of ionospheric origin, which is able to move between the hemispheres while maintaining a co-rotating footprint. The plasmasphere is relatively symmetrical in the azimuthal direction, except in the dusk sector where there is a prominent bulge (Carpenter et al., 1993). The size of the region is reduced following strong geomagnetic activity, when a cross-tail electric field acts to strip away the outer most part, leaving a sharply defined boundary. Beyond this boundary, which is known as the plasmapause, the plasma density falls by 2–3 orders of magnitude, and does not co-rotate with Earth.
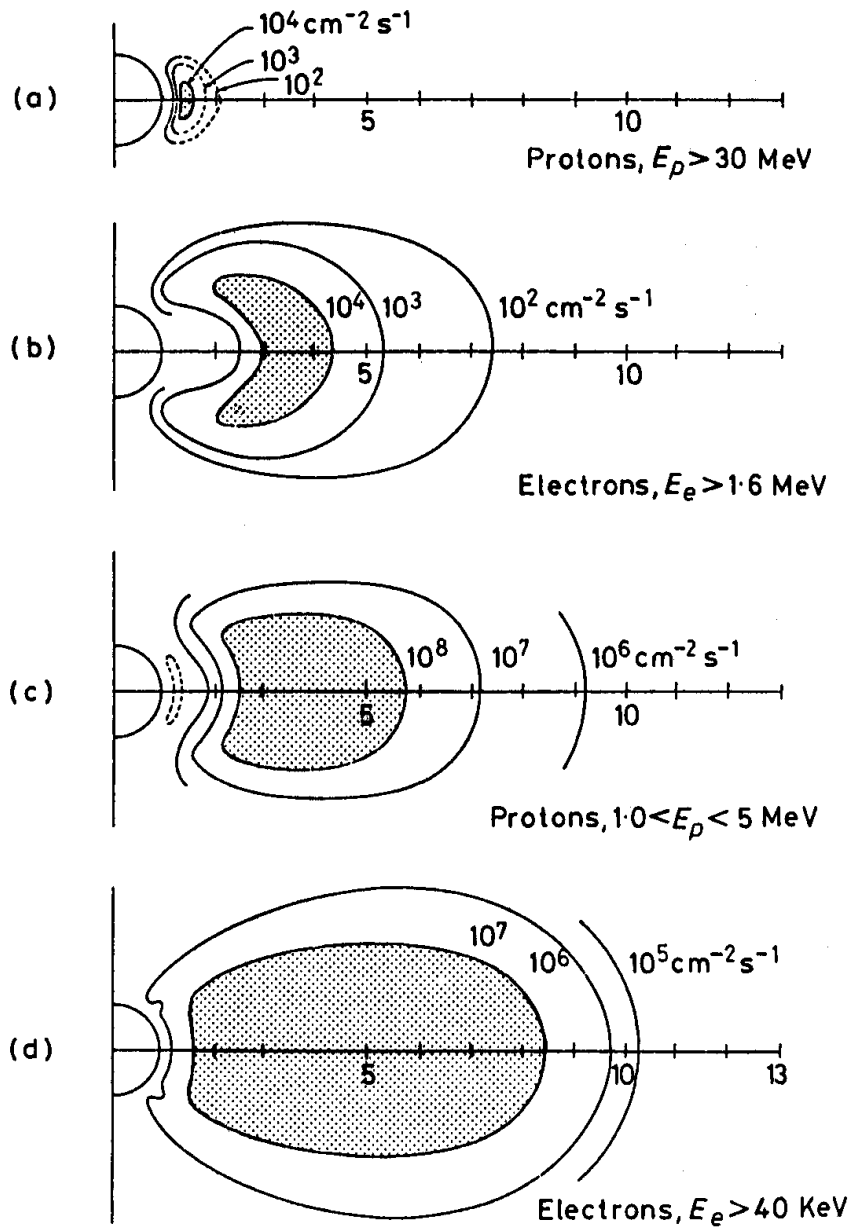
Figure 1.4: The Van Allen radiation belts, (after Hess (1968)).

Trapped on closed field lines, the Van Allen particles (van Allen and Frank, 1959) are the most energetic in the magnetosphere. The spatial distribution of the electrons and protons that comprise the Van Allen belts are illustrated in figure 1.4.

In general, higher energy particles are located closer to Earth. The electrons are the most variable, their distribution including a marked gap known as the *slot*.

1.3.2   Charged particle motion in Earth's magnetic field

Close to the planet, the Earth's magnetic field is, to a reasonable first approximation, a dipole field. The geomagnetic poles are located at 82.7°N 114.4°W (the Geological Survey of Canada, 2005 estimate), and 63.5°S 138.0°E (the Australian Antarctic Division, 2004 estimate).

In polar coordinates, the magnetic flux density in a dipole field, which has azimuthal symmetry, is given by

$$B(R, \Phi) = \frac{M}{R^3} \left(1 + 3\sin^2 \Phi\right)^{\frac{1}{2}}, \qquad (1.1)$$

(see e.g. Boyd and Sanderson (2003)) where M is the dipole moment, R is the radial distance from Earth, and Φ is the magnetic latitude. The equation describing a field line is

$$R = L\cos^2 \Phi, \qquad (1.2)$$

where L is the distance from Earth at which the field line crosses the equatorial plane, known as the McIlwain L parameter (McIlwain, 1961).

Charged particle dynamics

The motion of a charged particle, with charge q and mass m, in an electric field $\mathbf{E}$ and a magnetic field $\mathbf{B}$, is given by the Lorentz equation:

$$\frac{dm\dot{\mathbf{r}}}{dt} = q\left(\mathbf{E}(\mathbf{r}, t) + \dot{\mathbf{r}} \times \mathbf{B}(\mathbf{r}, t)\right).$$ (1.3)

In this form the momentum, $m\dot{\mathbf{r}}$, may be replaced by the relativistic equivalent when the velocity approaches the speed of light (Boyd and Sanderson, 2003).

If it can be assumed that the underlying background fields are much greater than those induced by the motion of the particles, Maxwell's equations may be used to derive consistent electric and magnetic fields.

$$\nabla \times \mathbf{E} \quad = -\frac{\partial \mathbf{B}}{\partial t}$$ (1.4)

$$\nabla \times \mathbf{B} \quad = \epsilon_0 \mu_0 \frac{\partial \mathbf{E}}{\partial t} + \mu_0 \mathbf{j}$$ (1.5)

$$\nabla \cdot \mathbf{E} \quad = \frac{q}{\epsilon_0}$$ (1.6)

$$\nabla \cdot \mathbf{B} \quad = 0$$ (1.7)

where $q(\mathbf{r}, t)$ and $j(\mathbf{r}, t)$ are the charge and current densities respectively. If the fields induced by particle motion are deemed significant a different approach is required. The aim of magnetohydrodynamic theory, see section 1.3.5, is to set up a self consistent description of a plasma, with induced fields taken into account.

A charged particle will follow a helical path in a uniform and constant magnetic field, gyrating around a field line while moving along it. Generally, but more slowly, the particle will also drift across the field lines. This description remains useful where the radius of gyration is small compared to the distance over which the magnetic field varies. In such a case the motion around the field is almost circular, and the overall motion can be described by the *guiding centre* of the particle. Within the magnetosphere, these three motions are generally of such different speeds they may be considered separately.

Cyclotron rotation

The radius, r_B, of the circular path is known as the Larmor radius, or gyroradius. It can be found by equating the Lorentz force

$$F = q \cdot \mathbf{v} \times \mathbf{B} \qquad (1.8)$$

with the centripetal force, $F = mv^2/r$, giving:

$$r_B = \frac{mv}{|\mathbf{B}|\,q}, \qquad (1.9)$$

where $\mathbf{B}$ is the magnetic flux density, and v, q, and m are the particle's velocity, charge and mass respectively. If the particle is moving along the field line, the angle between $\mathbf{B}$ and $\mathbf{v}$ is known as the *pitch angle*, α. Then:

$$r_B = \frac{mv \cdot \sin \alpha}{|\mathbf{B}|\,q}. \qquad (1.10)$$

Gyration around the field line occurs at an angular frequency independent of the gyroradius:

$$\omega_B = \frac{q\,|\mathbf{B}|}{m} \tag{1.11}$$

Equations 1.9 and 1.11 are valid for relativistic particles, provided that the relativistic mass is used:

$$m = m_0\gamma = m_0\left[1 - \frac{v^2}{c^2}\right]^{-\frac{1}{2}} \tag{1.12}$$

Betatron acceleration

The magnetic flux provides a purely centripetal force, which does not change the angular momentum of the particle, $mvr_B = mv_\perp^2/\omega_B$. However, the gyrofrequency is proportional to the magnetic flux density, and both are therefore proportional to the perpendicular kinetic energy of the particle:

$$E_\perp = \frac{1}{2}mv_\perp^2 \propto \omega_B \propto |\mathbf{B}|\,. \tag{1.13}$$
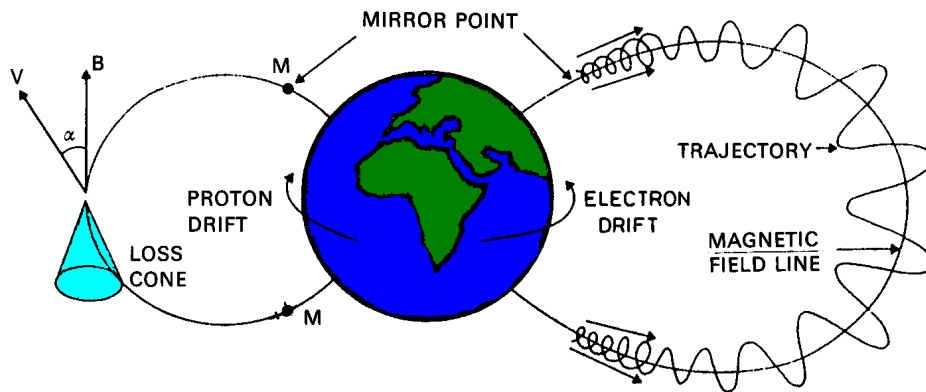
Figure 1.5: Bouncing and drifting motion of electrons and ions trapped on closed field lines, including the equatorial loss cone, (after Lemaire (1982)).

1.3.3   Trapping between mirror points

In a dipole field, the helical path of a charged particle along a magnetic field line will present an increasing magnetic flux density as the particle approaches the poles. The field, which is assumed to be static, does no work on the particle, but in accordance with equation (1.13), the perpendicular kinetic energy increases proportionally with the magnetic flux density. With motion along a magnetic field line there is therefore an invariance of the magnetic moment, $\mu = mv_\perp^2/2B$. The additional energy is provided by the parallel motion of the particle, $v_\parallel$, which is reduced. At a point known as the mirror point, where $v_\parallel = 0$, the particle changes direction, or 'bounces'. The force that effectively repels the particle from the magnetic poles is known as the *mirror force.*

Later (chapter 5) the effect of a non-static magnetic field is encountered. When magnetic field oscillations match the motion of charged particles, energy can pass from one to the other. Damping near a wave-particle resonance is a means by which large scale waves are observed to drive small scale waves in the magnetosphere.

The location of the mirror point is a function of equatorial pitch angle, α_{eq}, and is independent of energy (Boyd and Sanderson, 2003). Particles with smaller pitch angles bounce further from the magnetic equator, and particles with $\alpha_{eq} = 0$ will not bounce at all. There is therefore a limit in equatorial pitch angle, below which a particle will reach the dense atmosphere, subsequently being lost to collisions, before reaching the mirror point. In three dimensions this angle becomes a cone, and is known as the *loss cone*. Figure 1.5 provides an illustration of the bouncing, and drifting motion of charged particles, including the loss cone, and pitch angle.

1.3.4   Charged particle drift

Applying a force to a charged particle in a magnetic field produces a rather unintuitive result. If the force and magnetic field are not parallel, the particle will drift with a velocity, $\mathbf{v}$, perpendicular to both the field, $\mathbf{B}$, and the applied force, $\mathbf{F}$.

$$\mathbf{v} = \frac{\mathbf{F} \times \mathbf{B}}{q \left| \mathbf{B} \right|^2}. \tag{1.14}$$

If the force relates to an applied electric field, $\mathbf{E}$, the resultant drift velocity is independent of the mass, charge, and energy of the particle. It is known as the $\mathbf{E} \times \mathbf{B}$ drift.

$$\mathbf{v_{E \times B}} = \frac{q\mathbf{E} \times \mathbf{B}}{q \left| \mathbf{B} \right|^2} = \frac{\mathbf{E} \times \mathbf{B}}{\left| \mathbf{B} \right|^2}. \tag{1.15}$$

The straight-line inertia of a particle moving along a curved magnetic field line provides a centrifugal force, $F_c = mv^2/r_c$. The curvature radius is defined as $r_c = B/(\partial B/\partial R)$, where R is the geocentric radius. The velocity associated with this force is known as curvature drift. It is perpendicular to the centrifugal force, and to the magnetic field, with a magnitude of

$$v_c = \frac{mv^2}{qB^2} \cdot \frac{\partial B}{\partial R}. \tag{1.16}$$

Positive ions bouncing in Earth's dipole field will curvature drift westward, whereas electrons will drift eastward.

Magnetic field strength B_2

R_1

R_2

Magnetic field strength B_1

$(B_2 > B_1;$ therefore, $R_1 > R_2.)$
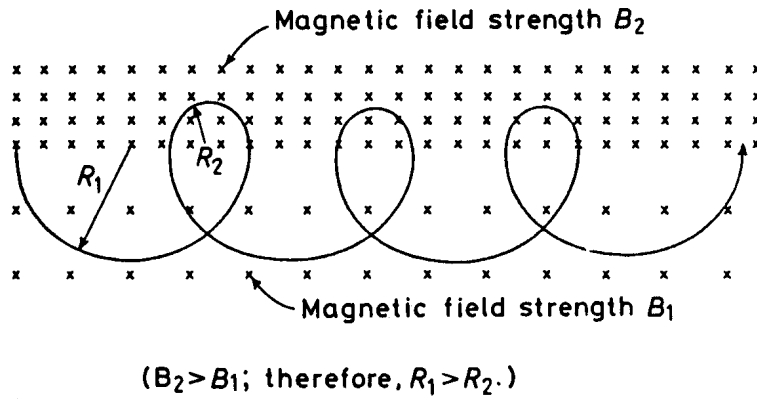
Figure 1.6: An illustration of magnetic gradient drift, (after Hess (1968)).

The gradient of the magnetic field strength, $(\partial B / \partial R)$, provides an additional drift mode. Aptly known as gradient drift, its mechanism is illustrated in figure 1.6. A particle traversing a more intense magnetic field will find its gyroradius reduced. In Earth's magnetic field the directions of gradient drift are the same as those for curvature drift, and the two effects are usually combined as the gradient-curvature drift (Solomon, 1975).

$$v_{gc} = \frac{v_c}{2} \cdot \left(1 + \cos^2 \alpha \right). \tag{1.17}$$

The opposing drift directions of electrons and protons are responsible for the westward *ring current*, which acts to reduce the magnetic field on Earth's surface, especially during times of high geomagnetic activity when particle fluxes are enhanced (Walt, 1994).

1.3.5   Magnetohydrodynamics

In the solar-terrestrial environment, the fields induced by particle motion will generally be significant. The MHD equations take this into account to form a self consistent macroscopic fluid description of a plasma. Several simplifying assumptions are necessary in the formation of such a model. The choice of some of these assumptions will depend on the particular brand of MHD in question. In the most simple case, plasma comprises negatively charged particles, and positively charged particles with much greater masses. It is therefore, at the very least, a two fluid problem. Although this leads to various phenomena not possible in a neutral fluid, a single fluid model is often utilized to successfully describe various plasma features.

Classical fluid dynamics provides a closed set of equations to which a force term, $\mathbf{F}$, is added to take account of the conducting nature of plasma:

$$\rho\mathbf{F} = q\mathbf{E} + \mathbf{j} \times \mathbf{B} \tag{1.18}$$

where ρ is the plasma mass density, and $\mathbf{E}$ and $\mathbf{B}$ are determined by Maxwell's equations. Given the existence of the current, $\mathbf{j}$, some flexibility in the single fluid approximation must be allowed. The usual practice is to adopt Ohm's law:

$$\mathbf{j} = \sigma\left(\mathbf{E} + \mathbf{u} \times \mathbf{B}\right) \tag{1.19}$$

where $\mathbf{u}$ is the velocity of a fluid element. It should be noted that this approach is not strictly valid without an inertial frame (constant $\mathbf{u}$).

By combining Ohm's law with Ampére's law, and substituting into equation 1.4, the induction equation is derived:

$$\frac{\partial \mathbf{B}}{\partial t} = \frac{1}{\sigma \mu_0} \nabla^2 \mathbf{B} + \nabla \times (\mathbf{u} \times \mathbf{B}) \tag{1.20}$$

1.3.6 Ideal MHD

Further simplification may be achieved by assuming quasi-static equilibrium. A plasma with local Maxwellian distribution functions has no heat conduction or viscosity. Dissipation is only possible through electrical conductivity in this case, which is known as *resistive MHD*. Removing dissipation altogether, by assuming infinite conductivity, leads to *ideal MHD*.

The ideal MHD equations are:

$$\frac{D\rho}{Dt} = -\rho \nabla \cdot \mathbf{u} \tag{1.21}$$

$$\rho \frac{D\mathbf{u}}{Dt} = (\nabla \times \mathbf{B}) \times \frac{\mathbf{B}}{\mu_0} - \nabla P \tag{1.22}$$

$$\frac{D\left(P\rho^{-\gamma}\right)}{Dt} = 0 \tag{1.23}$$

$$\frac{\partial \mathbf{B}}{\partial t} = \nabla \times (\mathbf{u} \times \mathbf{B}) \tag{1.24}$$

$$\nabla \cdot \mathbf{B} = 0 \tag{1.25}$$

where,

$$\mathbf{E} = -\mathbf{u} \times \mathbf{B} \tag{1.26}$$

$$\mathbf{j} = \frac{(\nabla \times \mathbf{B})}{\mu_0} \tag{1.27}$$

$$q = -\epsilon_0 \nabla \cdot (\mathbf{u} \times \mathbf{B}) \tag{1.28}$$

and the capital D represents a derivative performed on a fluid element.

The assumptions made in arriving at these equations include: non-relativistic particle energies; quasi-neutrality; strong collisions; and a large hydrodynamic length scale. In chapter 5 the ideal MHD equations are utilized to investigate cavity mode waves in the magnetosphere. Ideal MHD is commonly used throughout magnetospheric physics, however, a rigorous approach with respect to the absolute validity of the assumptions is beyond the scope of this thesis.

1.3.7   Waves in ideal MHD

In a homogeneous unperturbed plasma the ideal MHD equations support wave modes with dispersion relations

$$\omega^2 = k_{\parallel}^2 v_A^2 \tag{1.29}$$

$$\omega^2 = \frac{k^2}{2}(c_s^2 + v_A^2) \left[1 \pm (1 - \delta)^{1/2}\right] \tag{1.30}$$

where

$$\delta = 4\frac{k_\parallel^2}{k^2}\frac{c_s^2 v_A^2}{(c_s^2 + v_A^2)^2} \tag{1.31}$$

$k_\parallel$ is the component of the wave-number parallel to the magnetic field. $v_A = (B_0^2/\mu_0\rho_0)^{1/2}$ and $c_s = (\gamma P_0/\rho_0)^{1/2}$ are the Alfvén and sound speeds, respectively, in a plasma with underlying magnetic field strength B_0, pressure P_0, charged particle mass density ρ_0, and adiabatic index γ. For a derivation of equations 1.29 and 1.30, and for mathematical descriptions of some of the myriad of wave modes supported by plasmas, see e.g. Boyd and Sanderson (2003).

Equation 1.29 is the dispersion relation for shear Alfvén waves. In the ideal MHD approximation these are dispersionless. They propagate along the magnetic field and are analogous to plucked strings under tension, with a magnetic field line taking the role of a string. Indeed, if the magnetic tension B_0^2/μ_0 is equated with a string tension, the Alfvén velocity is the same as that for waves on an elastic string. The Alfvén mode is transverse, its displacement vector being perpendicular to B_0 and to k.

The second dispersion relation, equation 1.30, describes two compressional modes that result from combinations of magnetic pressure (the v_A terms), and plasma pressure (v_c). Since $0 \geq \delta \geq 1$, the plus sign provides a faster wave speed, and is therefore known as the fast magneto-acoustic mode, whereas the minus sign corresponds to the slow magneto-acoustic mode.

For perpendicular propagation ($k_\parallel = 0$) the slow mode does not exist, and the fast dispersion relation reduces to

$$\omega^2 = k^2(c_s^2 + v_A^2). \tag{1.32}$$

In the magnetosphere, shear Alfvén waves propagating along field lines are reflected by the high conductivity ionosphere in the northern and southern hemispheres, whereas compressional fast mode waves propagating perpendicular to the magnetic field are reflected by the low latitude ionosphere and an outer boundary, usually taken to be the magnetopause (Samson and Rankin, 1994).

Standing waves of each type resonate at eigenfrequencies dependent on the wave speed, and the length of the field line or size of the cavity. A coupling between the wave modes is known to occur where the resonant frequencies are close. In chapter 5 a theory based on drifting trapped particles in resonance with magnetospheric MHD waves is proposed as an origin of ionospheric precipitation pulsations with high azimuthal wave numbers (m numbers).

1.3.8 The substorm

Figure 1.7 shows the configuration of the magnetic field during southward and northward IMF (Dungey, 1961). Earth's dipole field is directed northward in the equatorial plane, allowing the field lines to connect with a southward IMF, in a process known as reconnection. At such times, the solar wind carries connected magnetic field lines from the day-side magnetosphere to the tail. The magnetic flux in the tail can not build up indefinitely and,
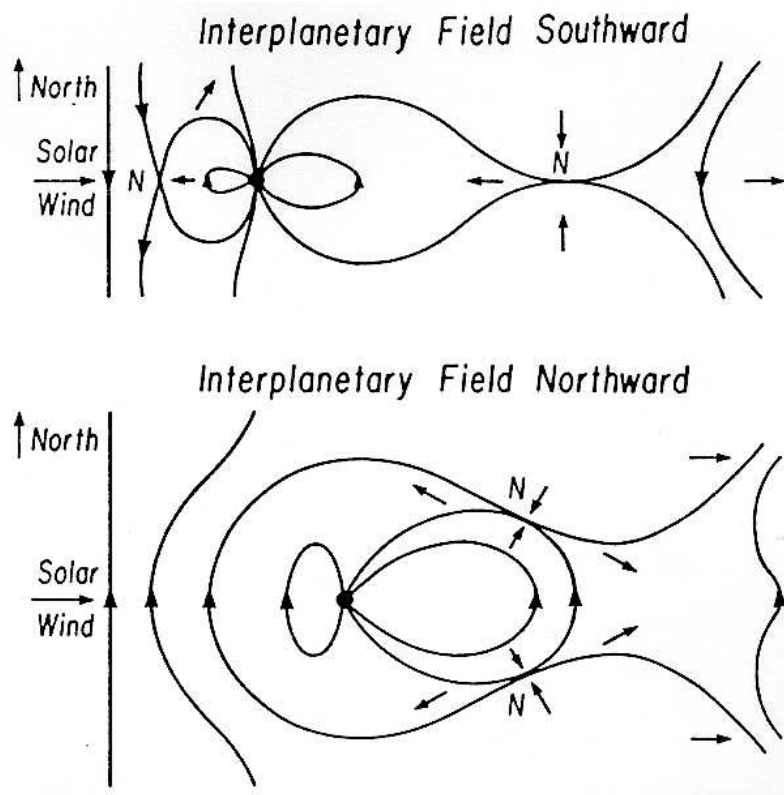
Figure 1.7: The Dungey (1961) reconnection model. During southward (top), and northward (bottom), interplanetary magnetic field.

after the *growth phase*, spontaneous reconnection in the magnetotail allows the field to snap back, while a structure of plasma and magnetic field, called a plasmoid, drifts away with the solar wind. The unloading of the tail is known as the *expansion phase*. High speed plasma flows earthward from the plasma sheet, and at geosynchronous orbit populations of high energy electrons are observed to be injected. Typically around 30–60 minutes later, the magnetosphere enters the *recovery phase*, in preparation for the next substorm. For a more detailed description of the substorm, see e.g. Nakamura (2006).

1.4 The Atmosphere

1.4.1 Regions of Earth's atmosphere

The neutral atmosphere is most commonly classified according to regions of temperature gradient, known as spheres. Much like regions of the magnetosphere, these are bounded by layers called pauses. The troposphere extends from the surface of Earth to an average altitude of around 8 km at the poles and 18 km at the equator. It is a region of high mixing, due to convection caused by solar heating of Earth's surface, and contains about 75% of the total mass of the atmosphere (Danielson et al., 2003). Within the troposphere the temperature falls with height at around 10 K/km or less. Above the tropopause is the stratosphere, where ultra-violet rays from the Sun, absorbed by ozone, are responsible for a positive temperature gradient with respect to altitude. The stratopause is located at the altitude of maximum temperature, at around 50 km, and is the lower boundary of the mesosphere, a second region of decreasing temperature. The mesopause boundary layer is the coldest part of the atmosphere, traditionally located at 85 km with a temperature of 180 K, although recent research, (Xu et al., 2007), has identified a second, stronger minimum at 100 km. The low temperature is a result of radiative cooling by CO_2, combined with very little absorption of solar UV rays. Air rising and subsequently cooling in the summer hemisphere, while descending and warming in the winter hemisphere, gives rise to a mesopause that is warmer in the winter than during summer, this is known as the mesopause anomaly (She et al., 1995).

Above the mesopause, heating by solar UV rays once again becomes significant in the thermosphere. Here temperature rises until becoming almost constant with altitude, but varying with time and solar activity, typically between $1000\,\mathrm{K}$ and $1250\,\mathrm{K}$. At thermospheric altitudes, neutral constituents divide into strata according to their molecular mass. For a more thorough description of Earth's atmosphere see e.g. Rees (1989).

The relationship between pressure variation and a change in altitude is given by

$$\frac{dP}{dh} = -nmg, \tag{1.33}$$

where P is pressure, h is altitude, g is gravitational acceleration, n is number density, and m is molecular mass. Utilizing the ideal gas law

$$P = nk_bT, \tag{1.34}$$

where k_b is Boltzmann's constant, and T is temperature, leads to the equation for hydrostatic equilibrium,

$$\frac{1}{P}\frac{dP}{dh} = \frac{-mg}{k_bT} = \frac{1}{H}, \tag{1.35}$$

where H is the scale height. If H is a constant, then

$$P = P_0 \exp\frac{-h}{H}. \tag{1.36}$$

where P_0 is the pressure at ground level.

However, in the terrestrial atmosphere the scale height is not constant, but increases with altitude from around 5 km at an altitude of 80 km, to approximately 75 km at an altitude of 500 km. This variation is due to higher temperatures, and lighter atmospheric constituents, at higher altitudes.
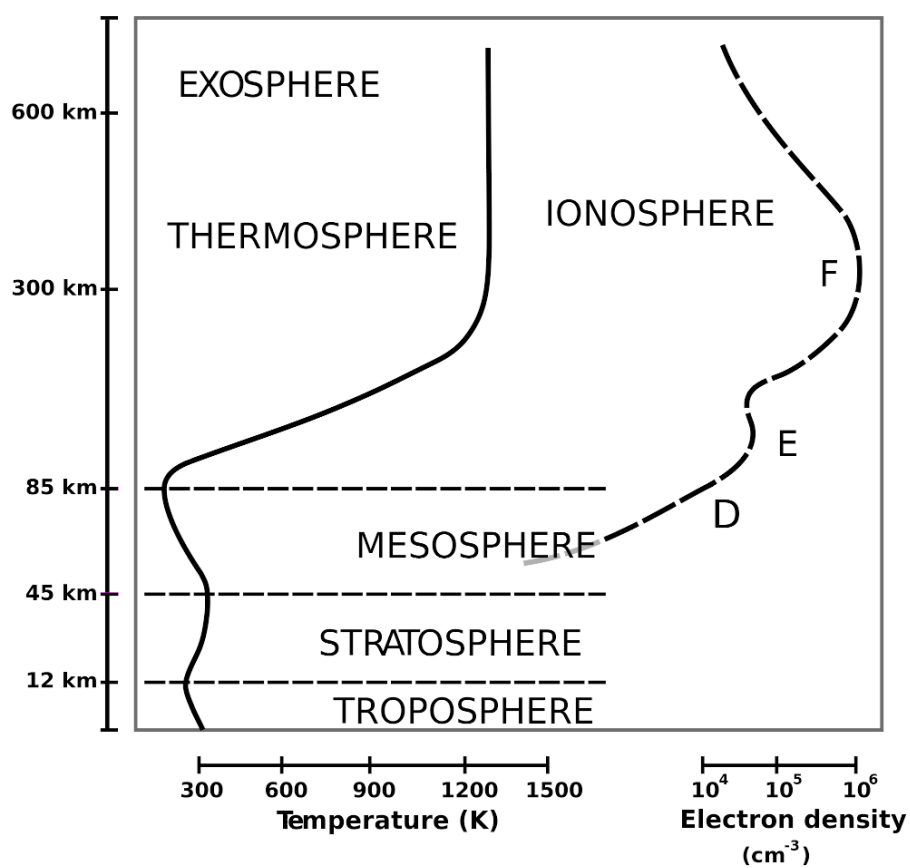
Figure 1.8: Regions of the atmosphere and ionosphere (public domain image)

1.4.2   The ionosphere

The regions of the ionosphere (figure 1.8) are determined primarily by the height-varying density and composition of the atmosphere, acted on by solar radiation. The D-region is the lowest, typically extending from around 70 km, to 90 km. During solar proton events, when protons emitted by the Sun are accelerated to high energies, levels of ionization can be significant at altitudes of 50 km and below (Hargreaves, 2005b). For the majority of time the primary source of ionization is that of nitric oxide by solar Lyman α radiation, but of a more variable nature is the ionization of the major neutral species (N_2, O_2) by high energy (>30 keV) electron precipitation, and hard X-rays emanating from solar flares. At night the high recombination rate severely reduces the number of free electrons in the D-region, especially at low altitudes. At higher altitudes, the E region (90 km to 120 km) responds to soft X-rays, extreme ultra-violet (EUV), and precipitating electrons above 5 keV. The F region is the upper most, extending from 120 km to 400 km.

1.4.3   Absorption of cosmic radio waves

The Relative Ionospheric Opacity Meter (riometer) is an instrument that is central to this thesis. As its name suggests, a riometer measures the opacity of the ionospheric plasma to radio waves of cosmic origin (Little and Leinbach, 1959).

To account for the absorption of an electro-magnetic wave passing through a plasma, the wave number, k, is given a complex value. The refractive index of the plasma is the ratio of wave's phase speed in the medium, to its speed in free space, c. It can be defined in terms of the complex wave number as

$$n = (\mu - i\chi) = \frac{kc}{\omega}, \tag{1.37}$$

where μ is the real part of the complex refractive index, χ is the imaginary part, and ω is the (angular) wave frequency.

The Appleton-Hartree equation gives the refractive index in terms of the properties of a plasma.

$$\begin{aligned} n^2 &= (\mu - i\chi)^2 \\ &= 1 - \frac{X}{1 - iZ - \frac{Y^2 \sin^2\theta}{2(1-X-iZ)} \pm \left[\frac{Y^4 \sin^4\theta}{4(1-X-iZ)^2} + Y^2\cos^2\theta\right]^{\frac{1}{2}}}, \end{aligned} \tag{1.38}$$

where,

$$\begin{aligned} X &= \frac{\omega_p^2}{\omega^2} = \frac{N_e e^2}{\epsilon_0 m_e \omega^2}, \\ Y &= \frac{\omega_H}{\omega} = \frac{eB}{m_e \omega}, \\ Z &= \frac{\nu_m}{\omega}. \end{aligned} \tag{1.39}$$

ω_H is the angular electron gyrofrequency, ω_p is the plasma angular frequency, N_e is the electron number density, e is the electron charge, B is the background magnetic flux density, ν_m is the electron momentum-transfer collision frequency, θ is the angle between the magnetic field and the wave k vector, and ϵ_0 is the permittivity of free space. For a derivation of the Appleton-Hartree equation see e.g. Davies (1966).

A wave propagating through the ionosphere may encounter two types of absorption. Deviative absorption is dominant in the F layer, a region in which the high electron density leads to a reduction in the real part of the refractive index, μ, effectively slowing the group velocity of the wave. If the refractive index reaches zero, the wave will be reflected. Equation 1.37 would seem to imply that such a refractive index contradicts the theory of relativity, however, information is carried at the group velocity, $v_g = d\omega/dk$, which certainly remains below c. The cosmic noise absorption measured by a riometer is almost entirely of the non-deviative type.

Non-deviative absorption

As an electro-magnetic wave propagates through plasma, electrons accelerated by the wave subsequently re-radiate the energy by their motion. However, collisions with other species cause changes in the phase of the oscillating electrons, and wave energy is lost to thermal energy in the plasma. To calculate the proportion of the wave power lost to this non-deviative absorption, simplification of equation 1.38 is necessary.

An assuming is made that the wave propagates close to the direction of the magnetic field, $\theta \to 0$. Under such circumstance, $\sin \theta \to 0$, $\cos \theta \to 1$, and equation 1.38 reduces to

$$(\mu - i\chi)^2 = 1 - \frac{\omega_p^2/\omega^2}{1 - i\nu_m/\omega \pm \omega_H \cos \theta/\omega}. \tag{1.40}$$

The imaginary part of the complex wave number, commonly given the symbol κ, represents an evanescing component of the wave.

By separating (1.40) in to its real and imaginary parts, the Appleton-Hartree equation for the absorption coefficient, κ, of mono-energetic electrons (i.e. electrons sharing the same collision frequency) is found

$$\kappa = \frac{e^2}{2m_e c\epsilon_0} . \frac{1}{\mu} . \frac{N_e \nu_m}{\nu_m^2 + (\omega \pm \omega_H \cos \theta)^2} \quad \text{Np/m}, \tag{1.41}$$

where ν_m is the energy-dependent electron-neutral momentum-transfer collision frequency. The $\pm$ applies to absorption of left-hand and right-hand circular wave polarizations respectively, which are conventionally (but erroneously) referred to as the O and X modes. The ionospheric absorption of
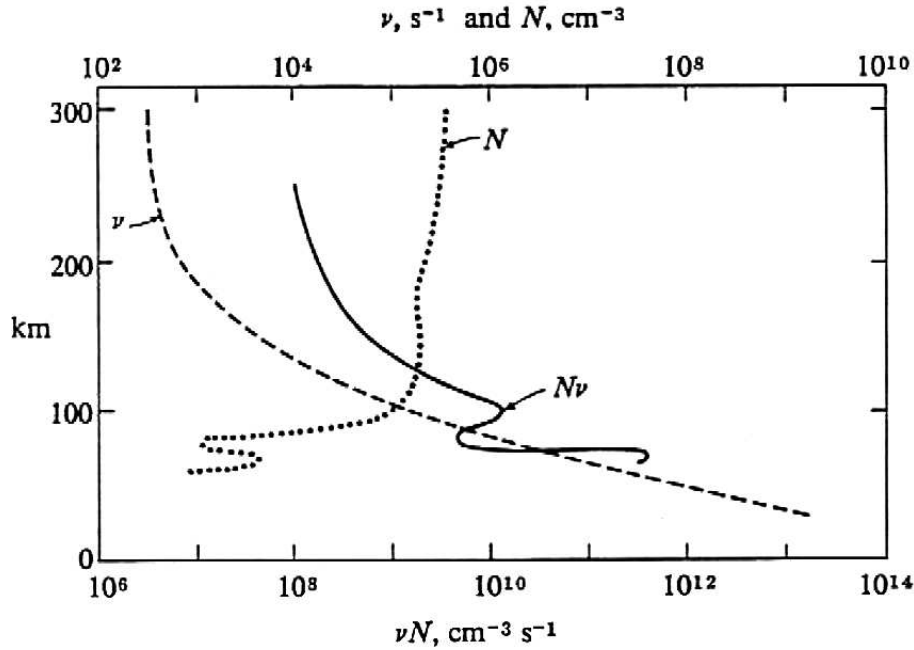
Figure 1.9: The altitude profile of $N_e\nu$, illustrating the variation of absorption with height (After Davies (1990))

cosmic radio waves is therefore a function of electron-neutral momentum-transfer collision frequency, and the electron density, integrated over the electron energy distribution, and the path length.

In the D and lower E region, where electron densities are relatively low, and absorption is non-deviative, $\mu \approx 1$ may be assumed. Additionally, for the receiving frequency of ARIES and IRIS (38.2 MHz, see chapter 2), ν_m^2 at altitudes above 60 km is small compared to ω^2, allowing integration over the electron distribution to be performed to the collision frequency alone – rather than the entire function – resulting in an *effective* collision frequency:

$$\nu_{\text{eff}} = \sum_{\text{neutral species}} \langle \nu_{e,\text{neutral species}} \rangle. \tag{1.42}$$

The angled brackets denote an average over the electron energy distribution, which is generally assumed to be Maxwellian. Converting from Nepers to decibels, and with an integration over the path length, (1.41) becomes:

$$\text{Absorption} = 4.6 \times 10^{-5} \int \frac{N_e \nu_{\text{eff}}}{\nu_{\text{eff}}^2 + (\omega \pm \omega_H \cos\theta)^2} \; dl \quad dB. \qquad (1.43)$$

Figure 1.9 shows the variation of non-deviative absorption with altitude. Electron density increases with altitude, whereas the collision frequency decreases, creating a peak absorption layer at around 90 km.

In chapter 3 the simplifications made in reaching this equation are put to the test using real world values, and its results are compared with alternative approaches.

1.4.4 Incoherent scatter radar

Incoherent Scatter Radar have become one of the most powerful ground based remote sensing techniques. By transmitting radio waves at VHF to UHF frequencies, and observing the much weaker backscatter from ionospheric electrons, many parameters can be measured. These include: electron number density, the ratio of electron to ion temperature, the ion temperature to mass ratio, the plasma velocity, and the relative motion of ions and electrons.

An electron that is able to move freely under the influence of an electromagnetic wave will scatter the radiation with a cross section:

$$\sigma_{free} = 4\pi r_e^2 \sin^2 \gamma, \tag{1.44}$$

where γ is the angle between the incident wave electric field, and the direction of the observer, and r_e is the classical electron radius. In the case of $\gamma = 90°$, i.e. direct backscatter, the cross section is of the order $10^{-28}\,\mathrm{m}^2$. This incredibly small cross section is the reason incoherent scatter radars must be designed to radiate megawatts, while receiving pico-watts in returned power. Large, highly directional antenna are therefore necessary, typically over $1000^2\,\mathrm{m}$ in area. The largest of these is Arecibo, in Puerto Rico (Castel, 2000) with a $73000^2\,\mathrm{m}$ collecting area, $265\,\mathrm{m}$ focal length, and a peak effective radiated power of $20\,\mathrm{TW}$ at $2380\,\mathrm{MHz}$.

Although the scattering is by the electrons, their motion is largely controlled by the much heavier ion population. A measure of the extent to which the ions influence the electron motion is the Debye length, λ_D. When the ion thermal motion is negligible,

$$\lambda_D = \sqrt{\left(\frac{\epsilon_0 k_B T_e}{N_e q_e^2} \right)}, \tag{1.45}$$

where ϵ_0 is the permittivity of free space, k_B is Boltzmann's constant, T_e is the electron temperature, q_e is the electron charge, and N_e is the electron number density. If the incident radiation has a wavelength much greater than the Debye length, scattering will be controlled by the ions, resulting in an *ion line*.

The process involved is one of Bragg-like scattering from ion acoustic waves with wavelengths half that of the incident radio waves (Rishbeth and Williams, 1985). Maximum scattering occurs when the fronts of the ion acoustic waves are perpendicular to the direction of the incident wave, i.e. directed toward and away from the transmitter. The result is two peaks in the received power: at the radio wave frequency plus and minus the Doppler shift relating to the velocity of the ion acoustic waves. The frequency shift associated with the ion line is typically several kHz. The electron lines, more commonly known as the *plasma lines*, are found at frequencies of several MHz above and below the incident radio wave frequency, corresponding to Doppler shifts from electron acoustic waves.
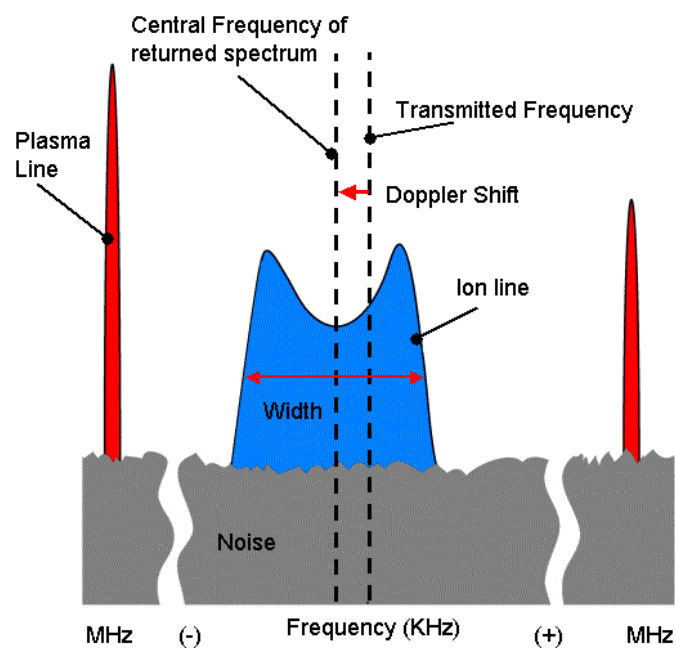
Figure 1.10: A typical spectrum of returned power for an incoherent scatter radar.

Ion acoustic waves travel at speeds within the velocity distribution of the ions, resulting in a broadening and merging of the ion lines due to Landau damping. In contrast, electron acoustic waves travel too fast for Landau damping of the electron population to occur, and the plasma lines remain sharp. An example of a received spectrum is given in figure 1.10. Generally, although both the ion line and plasma line are visible to incoherent scatter radars, the wealth of information available from the size, shape, and position of the ion line leads to this feature being at the forefront of their design.

Chapter 2

Instruments And Models

2.1 IRIS

Figure 2.1: Photograph of the IRIS riometer, Kilpisjärvi, Finland (courtesy S. Marple, Dept. Comm. Systems, Lancaster University).

Since the late 1950s, riometers have been an important tool in remote ionospheric sensing (Little and Leinbach, 1959). They maintain several advantages over radar systems: low cost, robust simplicity, continuous data coverage, and the ease of data interpretation.

The most basic riometers are essentially very sensitive radio receivers, each having a single directional antenna with a large beam width (typically 100 km at the 3 dB points). During the 1960s riometers with narrower beams were introduced as a natural progression (Hargreaves, 1969), and the first multi-beam riometers were developed (Butler and Lowe, 1961).
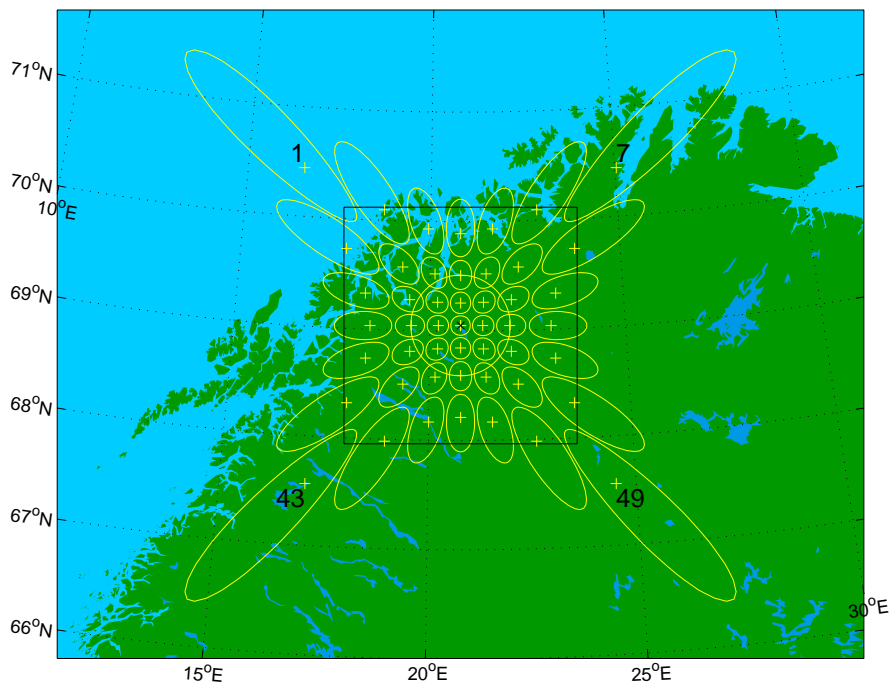
Figure 2.2: Map showing the distribution of IRIS riometer beams, projected at 90 km (courtesy S. Marple, Dept. Comm. Systems, Lancaster University).

As sensitive radio receivers, riometers are prone to interference. Steps must be taken during design and installation to avoid the reception of unwanted signals. To this end they operate on quiet sites, far from populated areas, and receive on protected frequency bands. Solar radio emissions are an unavoidable source of daytime interference, usually accompanying solar flares (Bastian et al., 1998; Dulk, 1985). If absorption measurements contain seemingly impossible negative value, it is usually due to additional power from solar radio emissions. Similarly, irregularities in the ionosphere can introduce spurious noise in the receiver power, this effect is know as scintillation (Chen et al., 1992).

The first Imaging Riometer for Ionospheric Studies (IRIS) system was deployed in Antarctica in 1988 (Detrick and Rosenberg, 1990). It comprised a 7x7 array of 49 riometer beams, achieving a maximum angular resolution of 13° at zenith. Subsequently, several other IRIS instruments were constructed. The IRIS utilized throughout this thesis is located approximately $83\,\mathrm{km}$ from the EISCAT VHF radar with beam 9 passing directly over EISCAT (Browne et al., 1995). It measures the ionospheric absorption of $38.2\,\mathrm{MHz}$ cosmic noise above Kilpisjärvi, Finland (69°03′ N, 20°47′ E) at $38.2\,\mathrm{MHz}$, sampling all beams once per second. A map showing the projection of IRIS beams is shown in figure 2.2.

Ionospheric absorption is measured as a reduction in the received cosmic noise power:

$$A(\mathrm{dB}) = 10\log_{10}\frac{\mathrm{P}}{\mathrm{P}'}, \qquad\qquad (2.1)$$

where P' is the measured noise power, and P is the expected power level in the absence of additional absorption (a quiet day value). For each beam, a quiet (sidereal) day curve is calculated by an empirical method (Marple and Honary, 2004) once per fortnight. The ideal quiet day curve would measure the noise power received on a perfectly quiet day, with no scintillation or interference. The two week period between quiet day curves will usually contain sufficient data to calculate quiet values for all times of the sidereal day. For non-vertical beams a correction is required to account for the longer path lengths at oblique angles. This is approximately $1/\cos\theta$, where θ is the zenith angle.

From equation 1.43 it is apparent that, neglecting Earth's magnetic field and assuming that the wave frequency is considerably larger than the collision frequency, the absorption measured by a riometer is inversely proportional to the square of its receiving frequency.

2.2 ARIES

The Advanced Rio-Imaging Experiment in Scandinavia (ARIES) (Grill et al., 2003) was the first of its kind; a riometer based around a Mills Cross antenna array. This configuration achieves a 4 fold increase in spacial resolution when compared to other imaging riometers with the same number of antenna. ARIES received at 38.2 MHz, with a low-noise 64-channel receiver, designed specifically for ARIES, and used a Field Programmable Gate Array (FPGA) to conduct beam forming entirely in the digital domain. The angular resolution reached a maximum of 4.75° at zenith.
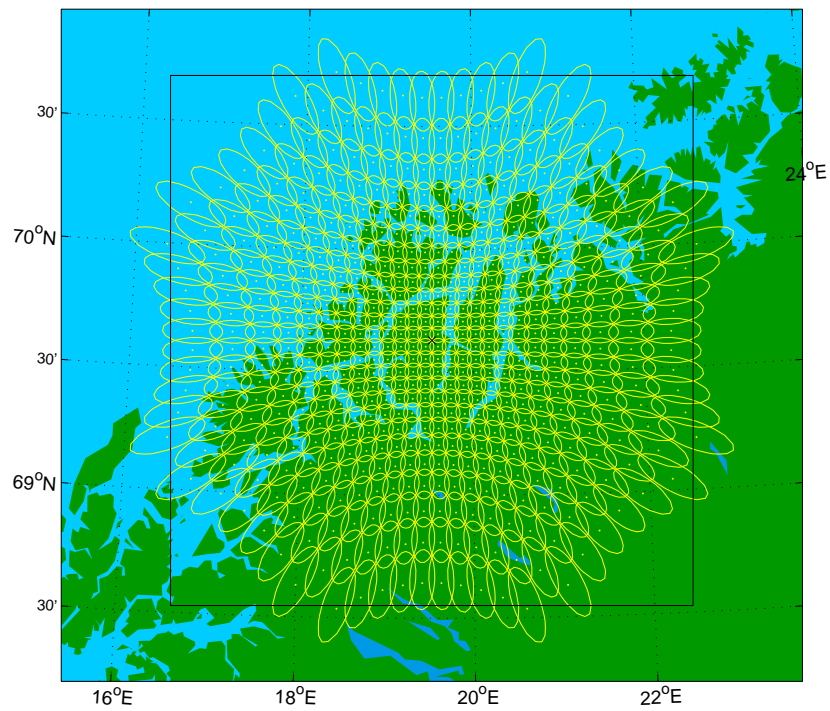
Figure 2.3: Map showing the distribution of ARIES riometer beams, projected at 90 km (courtesy S. Marple, Dept. Comm. Systems, Lancaster University).

The improvements in receiver and beam forming technology since the completion of IRIS have afforded ARIES a similar noise level at the same integration times, a remarkable feat given its far fewer antennae (Grill, 2007).

ARIES was located near Ramfjordmoen, Norway (69.63° N, 19.52° E). A location chosen for its proximity to several other experiments: STARE (Scandinavian Twin Auroral Radar Experiment), the EISCAT radars in Tromsø, and Andoya and Kiruna rocket ranges. Shown in figure 2.3 is a projection of ARIES beams.

At the time of writing, a temperature dependent error in ARIES receivers introduced an unpredictable slowly varying component in the received power, which made quiet day curve generation impossible. However, this has no impact on the research presented in this thesis, which only considers changes on much shorter time scales.

The Global Riometer Array, or GloRiA project, aspires to be the next step in the evolution of riometry. It aims to unite riometers from around the world to provide global coverage of solar-terrestrial processes.

2.3   EISCAT

The European Incoherent Scatter (EISCAT) VHF radar (Baron, 1986) has been measuring the basic parameters of the ionosphere from an altitude of 60 km to 1600 km since 1985. It is located near Tromsø (69°35′ N, 19°14′ E). A photograph of the 120 m by 40 m parabolic cylinder antenna of the VHF radar, is shown in figure 2.4. The antenna has a gain of 46 dBi, with circular polarization, and is fed by two klystroms, providing around 3 MW of power

Figure 2.4: Photograph of the EISCAT VHF radar, Tromsø, Finland (courtesy S. Marple, Dept. Comm. Systems, Lancaster University).

at 224 MHz. The antenna comprises two independent halves, which can be configured to be used as a single receiver, or split to give two concurrent beams. In 2001 the system received a major upgrade, with all new state-of-the-art signal processing hardware, with much of the processing now moved to the digital domain (van Eyken et al., 2001).

Between 9–13 November 2004, and on 28 October 2003, coinciding with the studies of chapters 3, and 4, respectively, the VHF radar was operating under the arc_dlayer-v program, which provided electron density measurements for the altitude range 60 − 140 km.

Currently, there are plans to replace the existing EISCAT radar systems in the coming years with an entirely new system called EISCAT-3D (Ulich et al., 2010).
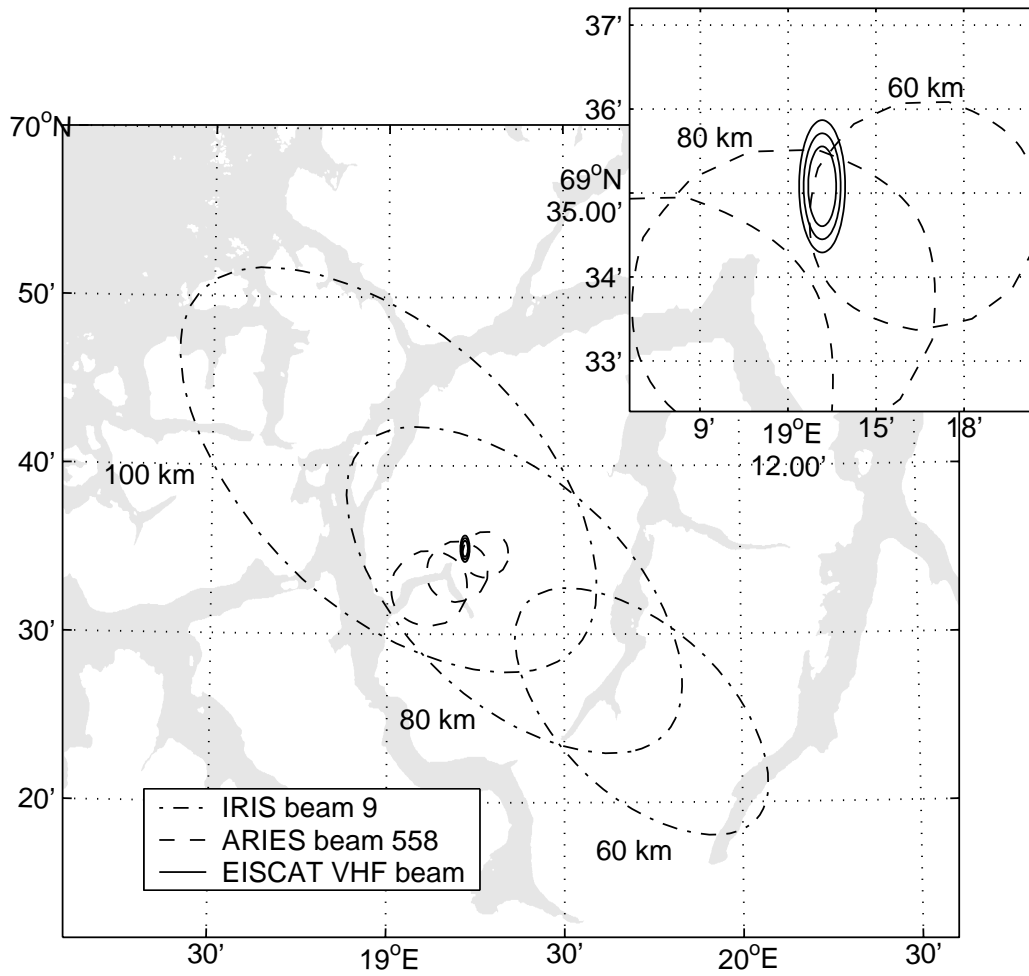
Figure 2.5: Map showing the location of beams 9 of IRIS and 558 of ARIES with the EISCAT VHF beam, at altitudes of 60, 80 and 100 km. Inset: close-up of the relatively narrow VHF radar beam.
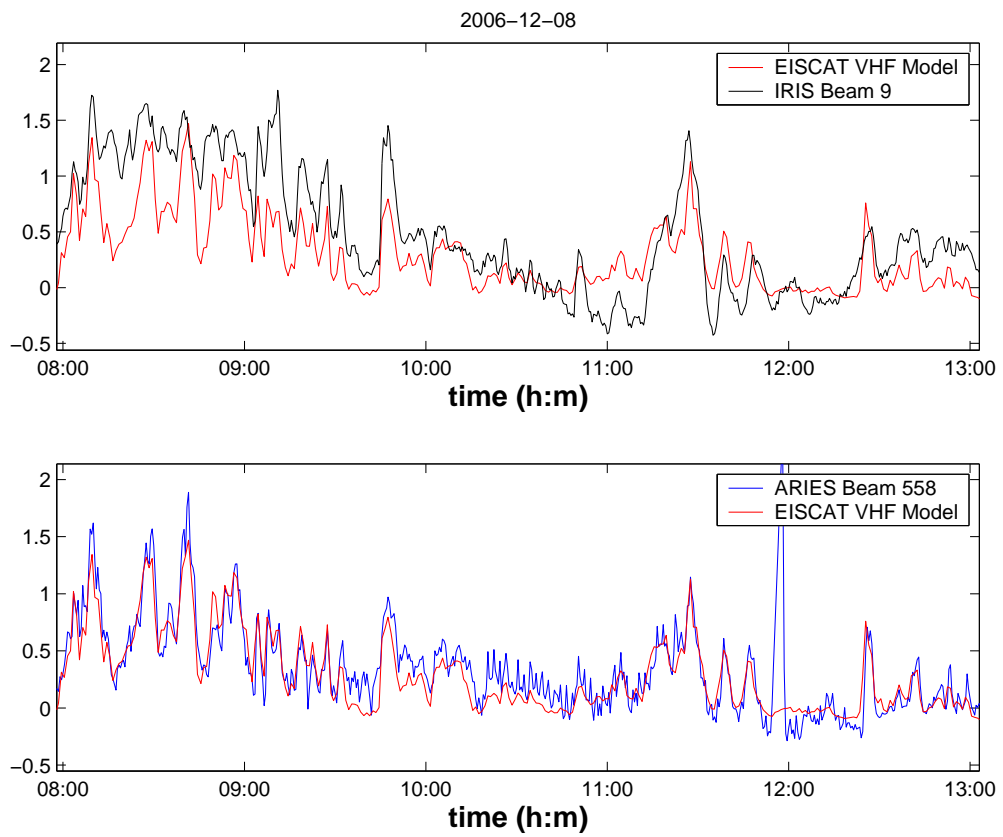
Figure 2.6: A comparison of ARIES (beam 558, blue), and IRIS (beam 9, black) measurements, with model results based on electron density measurements from the EISCAT VHF radar (red).

A map of beam projections, figure 2.5, shows that ARIES beam 558 (blue), IRIS beam 9 (black), and the EISCAT VHF radar beam (red) are each approximately centred on the same patch of sky, at an altitude of around $80 - 90$ km. Figure 2.6 illustrates the effect that the different beam sizes and viewpoints have on the absorption measured, or in the case of EISCAT, the absorption modelled. The ARIES and EISCAT beams are of similar width, compared to the much broader, and more oblique-pointing IRIS beam. The effect of this is especially clear between 08 UT and 09 UT, where the wider beam of IRIS acts to smooth over the peaks and valleys, which are therefore likely to have spacial scales smaller than the IRIS beam width.

2.4 GOES SEM

The Space Environment Monitors (SEM), aboard the Geostationary Operational Environmental Satellites (GOES), consist of instruments for the measurement of magnetic field, high energy particle fluxes (electrons, protons and alpha particles), and disk-integrated X-ray/EUV irradiance. Employing two ion chambers, the XRS system (Sylwester et al., 1995) provides two 15 bit X-ray channels, covering nominal wavelength ranges of $0.1 - 8$ nm, and $0.05 - 0.4$ nm (see Garcia (1994)). Data transmitted through the spacecraft telemetry allows real time observations of X-ray irradiance, in both spectral channels.

2.5 CAMMICE (POLAR)

The Charge And Mass Magnetospheric Ion Composition Experiment (CAM-MICE), aboard the Polar spacecraft (Acuña et al., 1995), provided energetic particle composition data from two instruments. The data set utilized in chapter 5 of this thesis is from the Double Coincidence Rate (DCR) channel of the Magnetospheric Ion Composition Sensor (MICS) (Wilken et al., 1992). The DCR channel responded mainly to the dominant proton species, with energy bins spaced logarithmically between $1\,\mathrm{keV}$ and $328\,\mathrm{keV}$, and a spin averaged temporal resolution of $192\,\mathrm{s}$. Prior to its end of life in 2008, Polar was in a $1.8 \times 9\,R_E$ polar orbit, with an $\approx 86°$ inclination to the equator. Its spin was stabilized perpendicular to the orbital plane, with a period of 6 seconds.

2.6 Space Weather Indices

A number of indices exist in solar-terrestrial physics to characterize activity levels. These include:

AE – Auroral electrojet index. A measure of current strengths in the auroral zone ionosphere.

ap – Global (planetary) index of geomagnetic activity.

Dst – Equatorial and mid-latitude index of geomagnetic activity, providing an estimate of ring current strength.

$\mathbf{F_{10.7}}$ – Solar radio flux at $10.7\,\mathrm{cm}$ wavelength.

SSNe – Effective sunspot number, based on ionospheric measurements.

The $F_{10.7}$, and *ap* indices are utilized in this thesis, and are described in detail below.

2.6.1 $F_{10.7}$ Index

$F_{10.7}$ is the solar radio flux at a wavelength of 10.7 cm (2.8 GHz), incident at Earth. The daily value of this index is measured at local noon by the Pentictin Radio Observatory in Canada, in solar flux units (10^{-22}Wm^{-2}Hz^{-1}). It has been recorded without break since 1947, and remains one of the primary indicators of solar activity. $F_{10.7}$ is frequently used as a proxy for other solar emissions, such as the extreme ultra violet (EUV) flux, an important source of ionospheric ionization that is impossible to directly measure at ground level due to atmospheric absorption. Recently an updated index, called $E_{10.7}$, has been proposed for this purpose. $E_{10.7}$ comprises a component of solar EUV irradiance, and is compatible with existing models expecting an $F_{10.7}$ input (Shin'ichi, 2002).

10 cm band solar noise, which varies slowly over hours, to months, or even years, is associated with active regions, correlating strongly with the total magnetic field within them. It is the subject of current study (see Svalgaard and Hudson (2010)) that this long held correlation appears to be breaking down, beginning during solar cycle 23.

2.6.2   *K*, *Kp*, and *ap* Indices

The *K* index is 3-hourly quantification of disturbances in the horizontal component of Earth's magnetic field. It has been recorded as an integer value between 0 and 9 since 1939, (Bartels et al., 1939). The *Kp* index is derived from *K* as the global (planetary) weighted average, calculated over a network of 13 magnetometer stations between 44 and 60 degrees latitude. *Kp* is recorded in thirds of an integer, a value between 0 and 9, which may be followed by a - or +. For example, 5- is equivalent to $4\frac{2}{3}$. Since *Kp* uses a logarithmic scale, it is often useful to convert them to a linear equivalent, the *ap* index. The conversion is as follows:

Kp	0o	0+	1-	1o	1+	2-	2o	2+	3-	3o	3+	4-	4o	4+
ap	0	2	3	4	5	6	7	9	12	15	18	22	27	32
Kp	5-	5o	5+	6-	6o	6+	7-	7o	7+	8-	8o	8+	9-	9o
ap	39	48	56	67	80	94	111	132	154	179	207	236	300	400

Since it is linear, the 3-hourly *ap* index may be averaged over the period of a day, giving the daily *Ap* index.

2.7 NRLMSISE-00 Model

NRL's Mass Spectrometer and Incoherent Scatter Radar model (NRL-MSIS, Hedin (1991)), is an empirical model of the atmosphere. The name is a relic of early versions of a model that has since included a wider range of instrument data. For the first time, the most recent version includes mass density values determined by satellite drag, and encompasses four decades of data (Picone et al., 2002). The E indicates that this version of the model extends from the ground to space; earlier versions did not cover below 90 km. The 00 is simply the year of the model revision. NRLMSISE-00 takes account of parameters such as the ap, and $F_{10.7}$ indices (proxies for the main drivers of the upper atmosphere: geomagnetic activity, and EUV flux, respectively), together with geographic location, altitude, and time. Model outputs are the densities of the major neutral species, and the neutral temperature. The model is used extensively in the study of upper atmosphere physics, necessitating careful consideration of the accuracy of its output. Chapter 3 comprises a test of NRLMSISE-00, before it is utilized in a simulation of the ionospheric effects of a solar flare (chapter 4).

2.8   SIC Model

The Sodankylä Ion-neutral Chemistry model (SIC), (Turunen, 1996), is a one dimensional model of the chemistry in the mesosphere and lower thermosphere, including the ionospheric D-region. It comprises over 400 reactions, involving a total of 36 positive ions, 27 negative ions, and 14 neutrals.

The model uses altitude profiles of temperature and major atmospheric species from the empirical MSIS model, (Hedin, 1991), and from Shimazaki (1984).

Photo-ionization of molecular and atomic oxygen as well as dissociation of the molecular major species are calculated based on solar spectral irradiances from the Solar2000 model, (Tobiska, 2000). The radiative transfer calculation follows Rees (1989), with numerical integration based on Press et al. (1992), disregarding refraction for all wavelengths.

The SIC model can be run in either time-independent or time-dependent mode, the former being more suitable for the modelling of, for example, constant forcing on the day-side, while the latter allows for the study of transient events, such as the effects of the solar flare encountered in chapter 4.

Chapter 3

A New Method to Deduce the Effective Collision Frequency Profile in the D-Region

A test of the NRLMSISE-00 neutral atmosphere model.

3.1 Introduction

The aim of this work is to apply linear regularization to a large (several
thousand) number of cosmic noise absorption (CNA) measurements, with
corresponding profiles of electron density, in order to infer a collision fre-
quency profile of the ionospheric D-region, which is responsible for the ma-
jority of CNA at high frequencies. This will reveal whether electron density
measurements at any given altitude and time are contributing more or less
than expected to the ground-measured absorption. Thus, it provides a test
for the combined neutral density and temperature output of an atmospheric
model, such as NRLMSISE-00.

Previously, Miyazaki (1975) obtained a collision frequency profile by com-
bining eight rocket-measured electron density profiles of the Antarctic D-
region, with corresponding ground-based cosmic noise absorption measure-
ments. By assuming a log-linear altitude dependence, the least squares
method was employed to give a collision frequency profile of the form $\nu =
\nu_0 \exp(-h/H)$, where h is the height above ground level and H is the scale
height. Serafimova and Serafimov (1991) proposed a method utilizing two
ground-absorption measurements, together with ionosonde measurements,
to arrive at an approximate exponential collision frequency profile of the
ionosphere.

Gokov et al. (1991) described a technique to simultaneously estimate
electron density and electron-neutral collision frequency profiles, based on
measurements of differential absorption and phase differences of the O and

X components of partial reflection (PR) signals. This was used at Khar'kov
State University to measure electron density and collision frequency profiles
to an accuracy of better than 30 %. Similarly, Vuthaluru et al. (2002)
calculated collision frequency profiles in the low latitude D-region by partial
reflection differential absorption and differential phase, using the large MF
radar at Buckland, Australia. Though relying on atmospheric models for the
extrapolation of results from lower altitudes, a good agreement with CIRA-86
calculated collision frequencies was reported below 80 km.

Such investigations are critical in assessing and improving models of the
upper atmosphere, in which systematic errors can be a significant problem,
often caused by the interpolation and extrapolation of empirical data that
does not cover a wide enough range of locations, times, or conditions. For
example, the coverage of incoherent-scatter radar employed in the MSISE-90
database is concentrated in North America, and the longitude variation
makes use of only the first spherical harmonic (Hedin, 1991). This gives
room to potentially significant improvements to the model from instruments
based in Europe, and the rest of the world. Drob and Picone (2000) report
that MSISE-90 (Hedin, 1991), a precursor to NRLMSISE-00, and CIRA-86
(Flemming et al., 1988), are both thought to underestimate and overestimate
mesopause region temperatures by around 15 K, respectively. They explore
the shortcomings of such atmospheric models in an area where performance
would be of great importance, that of the potential infrasonic monitoring of
a Comprehensive Nuclear-Test-Ban Treaty (CTBT).

In the intervening years, between MSISE-90 and NRLMSISE-00, a number of studies (e.g. Bush and Chakrabarti (1995); Pant and Sridharan (1998)) suggested that MSISE-90 output may be in error by up to a factor of 2. These studies led to revisions in the code, with improvements focusing mainly on the thermosphere. The most recent version, NRLMSISE-00, has given particular attention to making improvements in the molecular oxygen ($O2$) and temperature profiles, which are intended to increase the model's potential to become the standard for space object orbit determination and prediction by the United States Navy and Air Force (Picone et al., 2002).

As a function of neutral density and temperature, the electron-neutral effective momentum-transfer collision frequency can, to some extent, act as a proxy for these parameters in a test of the accuracy of an atmospheric model. However, in addition to offering improvements for the next generation of models, the contrasting of contemporary measurements with models based on databases covering several decades may reveal the effects of climate change. NRL attacked this issue by studying the orbital parameters of spacecraft that had remained in orbit over several decades (Emmert et al., 2004). They reported an apparent cooling and contracting of the upper altitudes of the atmosphere in response to increased greenhouse gases, and predicted a density reduction by a factor of 2 by 2100 CE at thermospheric heights, if current climate change trends are to continue.

The primary result of this study is in the form of time-averaged correction factors for the effective collision frequency profile calculated with the NRLMSISE-00 neutral atmosphere model, for active ($ap > 50$) and quiet ($ap < 50$) conditions over the period 2004–11–09 to 2004–11–13. The method would be equally effective if results were to be split between, for example, heater on and heater off periods of a co-located ionospheric heating facility.

3.2 Theory

Kinetic calculations for the general refractive index (Garrett, 1985) are employed to investigate the validity of the simplifications made in reaching the Appleton-Hartree equation for absorption, equation 1.43. An identical result to the method of Sen and Wyller (1960) can be found by taking the differential form of this equation, (equation 1.41), and applying their primary assumption, namely that the collision frequency is proportional to the electron energy ($\nu_m \propto v^2$), and the function κ is integrated over the electron energy distribution using the Chapman-Enskog method (Chapman and Cowling (1970) and Itikawa (1971)). The Appleton-Hartree method has the advantage that a collision frequency function with any chosen dependence on electron velocity may be used.

The maximum electron density encountered within this study is around $9 \times 10^{11} \, \mathrm{m}^{-3}$, resulting in μ falling to 0.975 (at $38.2 \, \mathrm{MHz}$) and the differential absorption given by the integrand of (1.43) being around $2.5 \, \%$ too low. However, plotting time series of the electron density radar data reveals that

error-spikes of the same magnitude are common. These often result in nonsensical negative data values, and are difficult to remove without skewing integrated values — for example, by excluding all negative valued data. In view of the considerable random errors in the radar data, it is necessary that the relationship between electron density and absorption is linear, thus the approximation $\mu \approx 1$ is kept.

The error introduced by using an effective collision frequency is greatest at low altitudes and falls very quickly with increasing height. With a receiver frequency of $38.2\,\text{MHz}$ for IRIS, the absorption is typically calculated to be less than $2\,\%$ too large at $60\,\text{km}$, and $0.1\,\%$ too large at $70\,\text{km}$. However, at lower frequencies there is a marked increase in these errors.

It is convenient to take the simple formulas calculated by Schunk and Nagy (1978) for the effective collision frequencies of the most populous atmospheric species. These are based on the cross sections given by Banks (1966), with the exception of atomic oxygen. The momentum-transfer cross section of atomic oxygen is difficult to determine experimentally; Schunk and Nagy (1978) took results from Henry and McElroy (1968), but slightly more recent values by Thomas and Nesbit (1975) are chosen. The latter are a little higher over the temperature range of interest and closer to the values of Banks (1966). The relative concentration of atomic oxygen increases with altitude; at $110\,\text{km}$ it is around $12\,\%$ of the total neutral density. Here the higher cross section values provided by Thomas and Nesbit (1975), and used in this study, translate to a rise of just $3\,\%$ in the differential absorption.

For molecular nitrogen momentum-transfer cross sections are taken from Morrison et al. (1997). Although these differ considerably from Banks (1966), especially at low energies, the variations largely cancel when integrated over the electron energy distribution and amount to less than $2.5\,\%$ in the temperature range 150 - 500 K.

The updated effective momentum-transfer collision frequencies for use between $150\,K$ and $500\,K$, and employed in this study are:

$$\langle \nu_{e,N_2} \rangle = N(N_2)(4.02 + 2.37(1 - 1.54 \times 10^{-4}T_e)T_e) \times 10^{-17}, \qquad (3.1)$$

$$\langle \nu_{e,O} \rangle = 1.37 \times 10^{-16} N(O)(1 + 3.32 \times 10^{-4}T_e)T_e^{\frac{1}{2}}, \qquad (3.2)$$

where $N(N_2)$ and $N(O)$ are the densities of N_2 and O respectively, in m^{-3}. T_e is the electron temperature in Kelvin.

Cross sections for the other neutral species are taken directly from Banks (1966), noting that those for the other important species, O_2, agree with more recent measurements by Sullivan et al. (1995), within the errors of their work.

3.3 Method

A linear problem in inverse theory generally takes the form:

$$c_i = \int r_i(x)u_0(x) \; dx + n_i, \qquad (3.3)$$

where each c_i is a measurement that contains information about a particular
aspect of an unknown process, $u_0(x)$, and n_i is the error of the ith measure-
ment. The measurements are related to the unknown process by the response
kernel, $r_i(x)$. Given the measurements, their errors, and the response kernel,
a statistical approximation, $\hat{u}_0(x)$, to the unknown process, $u_0(x)$, is sought.
In the present case c_i is the height integrated absorption measured by IRIS
and $r_i(x)$ are modelled absorption profiles, (given by (1.43)). These modelled
profiles are calculated with electron densities measured by the EISCAT VHF
radar together with the model neutral atmosphere, NRLMSISE-00. $u_0(x)$
is therefore a scaling factor for the modelled absorption, which, after a
small iterative correction, gives a scaling factor for the modelled effective
momentum-transfer collision frequency at each altitude. For this reason the
absorption scaling factor is denoted as $u_0(x)$, and the collision frequency
scaling factor as $u(x)$. The radar range gates are discrete and the integral in
(3.3) is accordingly replaced by a sum.

By choosing the solution to be a scaling factor for model values the regu-
larization is greatly simplified, and — by re-running the neutral atmosphere
model for each profile — diurnal variations of the neutral atmosphere are
included a-priori.

The Backus-Gilbert method of regularization is utilized and briefly described below. For a more in-depth explanation see Press et al. (1996).

A solution is sought to the inversion problem, expressed in (3.3), that is a compromise between an exact solution to the dataset and one that is reasonable. This is achieved by minimizing the expression:

$$A + \lambda B, \tag{3.4}$$

where A is a measure of the *spread* (the reciprocal of resolution) of the solution, i.e. how far the solution is away from an exact solution for the dataset. B is a measure of its instability, i.e. how unrealistic the solution is. λ allows tuning of the result between a stable solution and one that best fits the specific dataset. The *resolution function*, $\hat{\delta}(x, x')$, is implicitly defined by:

$$\hat{u}_0(x) = \int \hat{\delta}(x, x') u_0(x') \, dx', \tag{3.5}$$

where $\hat{u}_0(x)$ is the smooth, statistical solution and $u_0(x')$ is the exact (though highly unstable) solution for the particular dataset used. x represents the altitude for which the solution is sought, and x' the altitudes of the radar range gates. Minimizing A, to increase the resolution of the solution, is equivalent to bringing the resolution function closer to the identity matrix. Figure 3.1 shows the resolution function corresponding to the result, for several values of x. The value of λ is reduced with altitude in order to keep a reasonable resolution across the entire range of x.
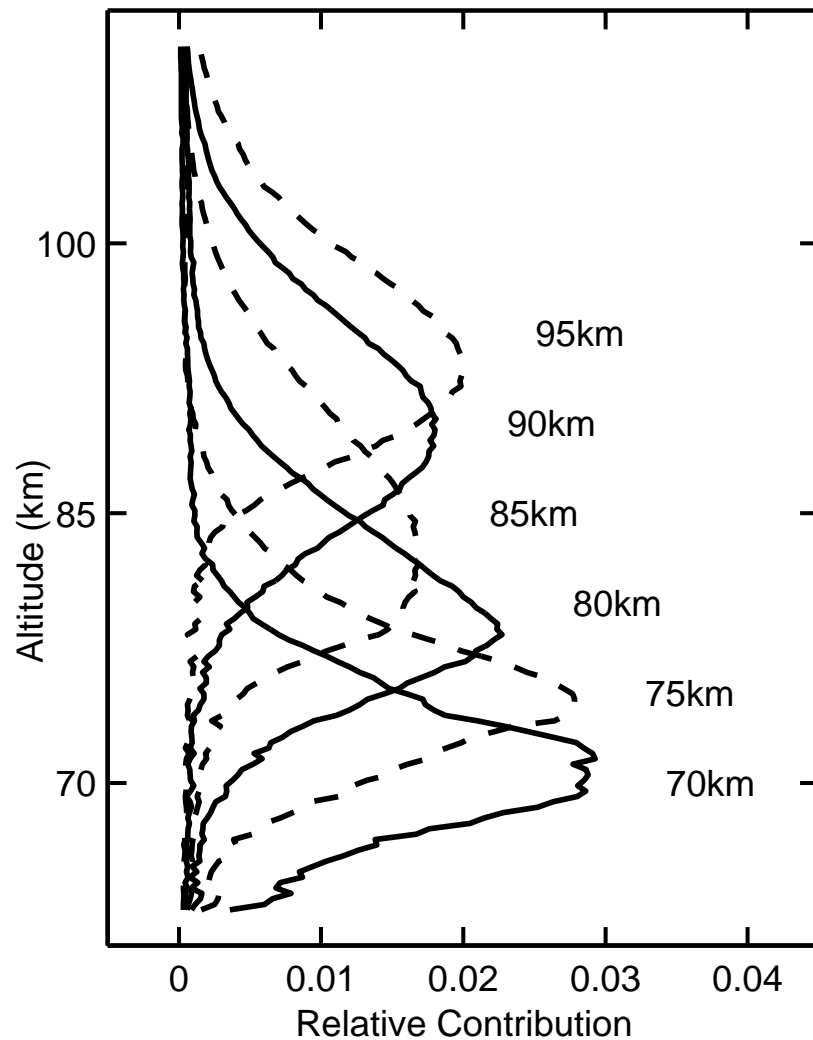
Figure 3.1: $\hat{\delta}$, the resolution function.

An error value, n_i, is assigned to each absorption measurement, c_i. These control the weight given to each sample, as well as defining the error bounds of the final result through the standard propagation of errors. The Backus-Gilbert method provides a solution for $\hat{u}_0(x)$, together with the corresponding errors.

It is useful to define the set of *inverse response kernels*, q_i:

$$\hat{u}_0(x) = \sum_i q_i(x) \cdot c_i, \tag{3.6}$$

and the integrated response kernel, R_i:

$$R_i = \int r_i(x) \, dx. \tag{3.7}$$

B, the measure of the stability of the solution, is given by:

$$B \equiv var\left[\hat{u}_0(x)\right] = \mathbf{q(x)}^{\mathbf{T}} \mathbf{S} \, \mathbf{q(x)}, \tag{3.8}$$

where S_{ij} is the covariance matrix. The errors, n_i, are herein assumed to be independent, therefore:

$$S_{ij} = \begin{cases} n_i^2 & i = j \\ 0 & i \neq j. \end{cases} \tag{3.9}$$

A, the measure of the width or spread of $\hat{\delta}(x, x')$, is defined as:

$$A = \mathbf{q(x)}^{\mathbf{T}} \mathbf{W(x)} \, \mathbf{q(x)}, \tag{3.10}$$

where $W_{ij}(x)$ is the *spread matrix*:

$$W_{ij}(x) \equiv \int (x' - x)^2 \, r_i(x')r_j(x') \, dx'. \tag{3.11}$$

This definition, used by Backus and Gilbert in their method, is one of many possible definitions. Equation 3.4 can now be written in terms of S_{ij} and $W_{ij}(x)$ as:

$$A + \lambda B = \mathbf{q(x)^T} \left[\mathbf{W(x)} + \lambda \mathbf{S} \right] \mathbf{q(x)}. \tag{3.12}$$

The solution to the set of inverse response kernels is:

$$\mathbf{q(x)} = \frac{\left[\mathbf{W(x)} + \lambda \mathbf{S} \right]^{-1} \mathbf{R}}{\mathbf{R^T} \left[\mathbf{W(x)} + \lambda \mathbf{S} \right]^{-1} \mathbf{R}}. \tag{3.13}$$

where $\mathbf{R}$ is the integrated response kernel.

The result of multiplying the inverse response kernels, $q_i(x)$, by the measurements, c_i, can be used to indicate whether a particular part of the dataset is responsible for contributing a greater or lesser amount than expected toward the measurement values. This is particularly useful in determining whether a specific feature in the dataset is real, or an instrumental effect. Finally, combining (3.6) and (3.8) gives:

$$\hat{u}_0(x) = \mathbf{c^T} \mathbf{q(x)} \pm \sqrt{\mathbf{q(x)^T} \mathbf{S} \mathbf{q(x)}}. \tag{3.14}$$

This solution is computationally demanding, requiring the inversion of an $N \times N$ matrix for each altitude value, x, where N is the number of measurements, c_i.

Once the differential absorption scaling factor, $\hat{u}_0(x)$, has been calculated, the collision frequency scaling factor can be found with an iterative formula based on the integrand of (1.43).

$$\hat{u}_{n+1}(x) = \hat{u}_0(x) \left(\frac{\hat{u}_n(x)^2 + \frac{(\omega \pm \omega_H \cos\theta)^2}{\nu_{\mathrm{mm}}(x)^2}}{1 + \frac{(\omega \pm \omega_H \cos\theta)^2}{\nu_{\mathrm{mm}}(x)^2}} \right), \tag{3.15}$$

$$\hat{u}(x) \equiv \hat{u}_{n\to\infty}(x) = \frac{\nu_{\mathrm{um}}(x)}{\nu_{\mathrm{mm}}(x)}, \tag{3.16}$$

where ν_{mm} is the modelled effective momentum transfer collision frequency, ν_{um} is the unknown effective momentum transfer collision frequency, and ω is the angular wave frequency. This step is necessary when studying absorption from a lower altitude or using a riometer with a lower receiving frequency, since $\omega^2 \gg \nu_m^2$ may no longer hold. In such cases one would also have to take care when calculating the modelled absorption, as discussed in section 3.2.

Notes within the Fortran code of the NRLMSISE-00 neutral atmosphere model (Picone et al., 2002), state that *"$F_{10.7}$, $F_{10.7}a$ (an 81-day running mean of $F_{10.7}$) , and ap effects are neither large nor well established below 80 km and these parameters should be set to 150, 150, and 4 respectively."* For the NRLMSISE-00 model input these suggested values are used at all altitudes ($\approx 60 - 110\,\mathrm{km}$), and throughout the event. This simplifies interpretation of the results when splitting the data between periods of active and quiet conditions, and avoids a discontinuity at 80 km.
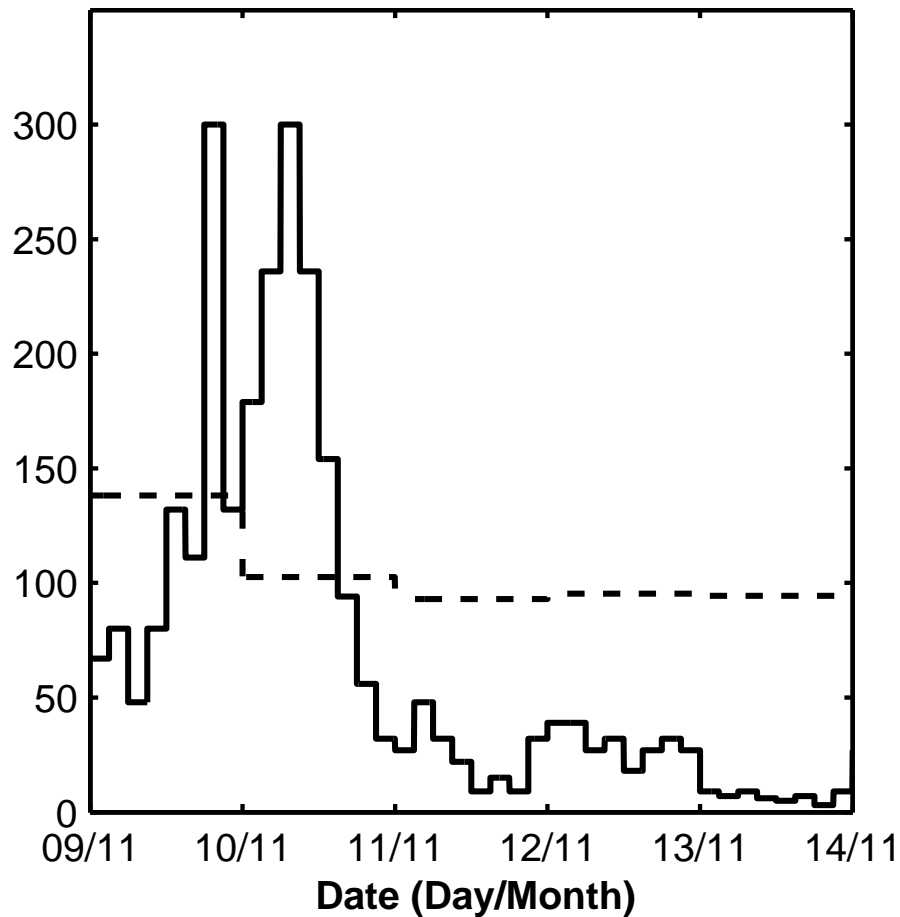
Figure 3.2: 3-hour values of ap index (solid line) with daily $F_{10.7}$ index (dashed line).

3.4 Data

Between 2004–11–09 to 2004–11–13 a unique set of data was recorded by EISCAT and IRIS. Over the 5 day period geomagnetic conditions changed from very active to quiet, there was little in the way of solar radio emissions to contaminate IRIS measurements, and polar cap absorption (PCA) (Reid, 1974) provided "illumination" of the lower D-region.
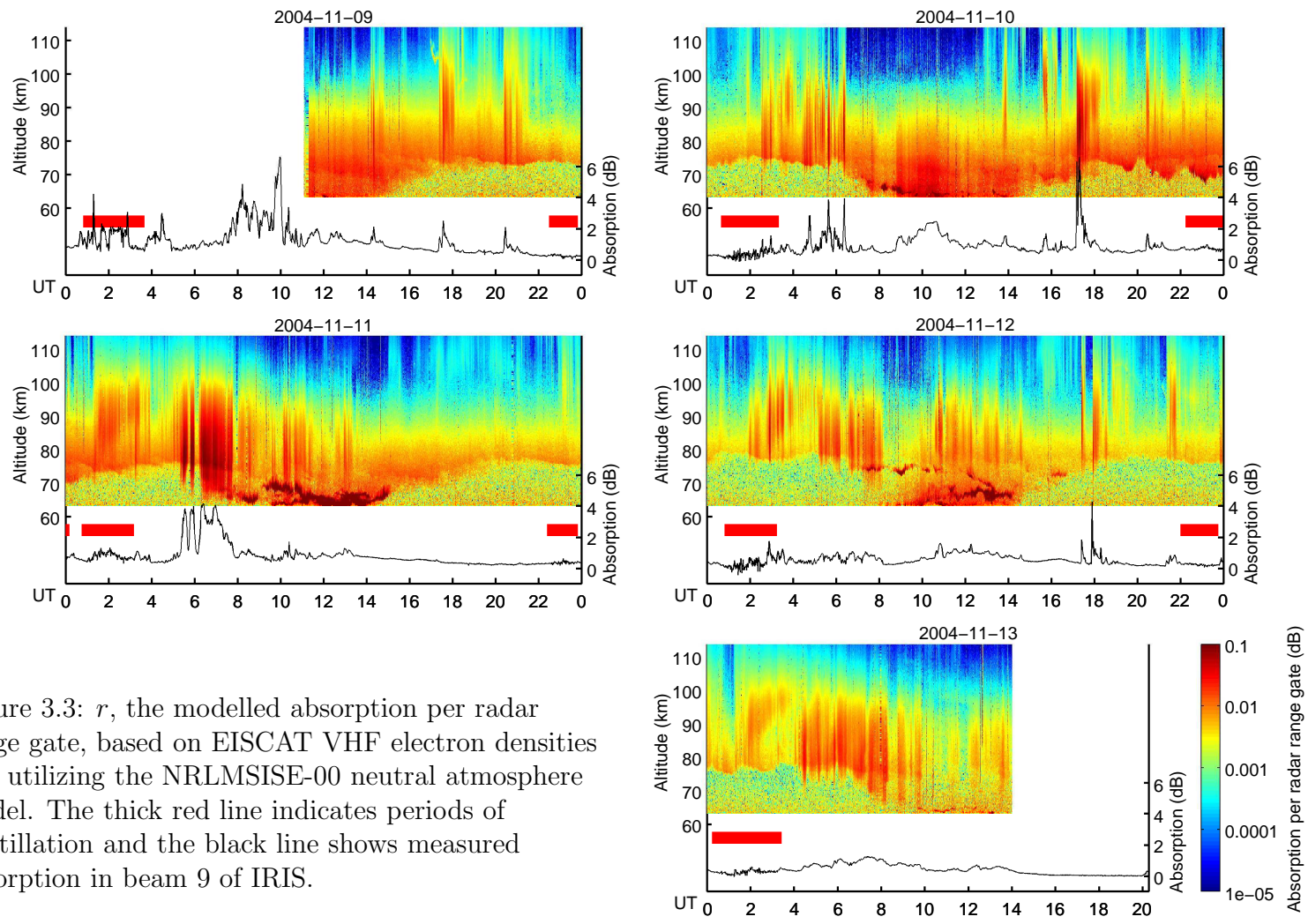
Figure 3.3: r, the modelled absorption per radar range gate, based on EISCAT VHF electron densities and utilizing the NRLMSISE-00 neutral atmosphere model. The thick red line indicates periods of scintillation and the black line shows measured absorption in beam 9 of IRIS.

Figure 3.2 shows that active conditions ($ap > 50$) lasted until 2004–11–10 21:00 UT and were followed by a quiet period, during which the value of ap remained below 50 for the rest of the dataset.

In Fig. 3.3 the height-integrated absorption measured by beam 9 of IRIS is shown, together with a colour plot of the modelled absorption based on radar data, which makes up the response kernel. The EISCAT VHF radar's power profile data with 1 minute integration and 300 m range gates is used. As expected, a clear correlation can be seen between patches of strong modelled absorption and high levels of measured absorption. Exceptions can be seen around midday, especially on 2004-11-11.

3.4.1   Excluded data

Figure 3.4 shows four subsets of data, each containing periods of poor correlation between the absorption modelled using EISCAT data and that measured by IRIS. These are excluded from the calculation.

In Fig. 3.4(a) the correlation is excellent until around 2004–11–10 05:15 UT, when the larger beam of IRIS has a smoothing effect on the now spatially non-uniform (as confirmed by IRIS images) ionosphere. Both peaks and troughs become less pronounced in the IRIS measurements.

Polar mesospheric winter echoes (PMWE) (Ecklund and Balsley, 1981) contaminate the radar data and, subsequently, the modelled absorption in Fig. 3.4(b). This occurs around midday on most of the days in the dataset, and is usually accompanied by a significant contribution to absorption in IRIS from PCA at altitudes below the range of the radar, rendering data from

these periods useless. Hargreaves (2005a) reports that altitudes between 45 and 65 km typically account for 80 % of the total daytime absorption during PCA events. For 2–3 hours toward the beginning and end of these periods, Fig. 3.3 shows that the absorption tapers off within the altitude range of the radar.

Beginning 2004–11–12 14:40 UT and lasting a few hours, a small localized patch of absorption overlaps with the eastern extent of beam 9, and is seen more strongly in the neighbouring beam to the east. It appears stationary within the IRIS images and is not seen in the radar (Fig. 3.4(c)). The modelled absorption matches well with the neighbouring IRIS beam to the west. Toward the end of this period large, shifting patches of absorption are seen advancing northward in the IRIS images. They enter IRIS beam 9 around a minute earlier than the radar (Fig. 3.4(d)). Additionally, the period 2004–11–10 18:10 UT to 2004–11–11 01:00 UT is also excluded. This covers three strong patches of enhanced electron density that seem to have little to no effect on the absorption measured by IRIS. When included, this period affects the result significantly; it is thought that the patches are very localized (i.e. smaller than the riometer beam).

With the exception of Fig. 3.4(b) these problems should be eliminated by using a riometer and radar with comparable fields of view.
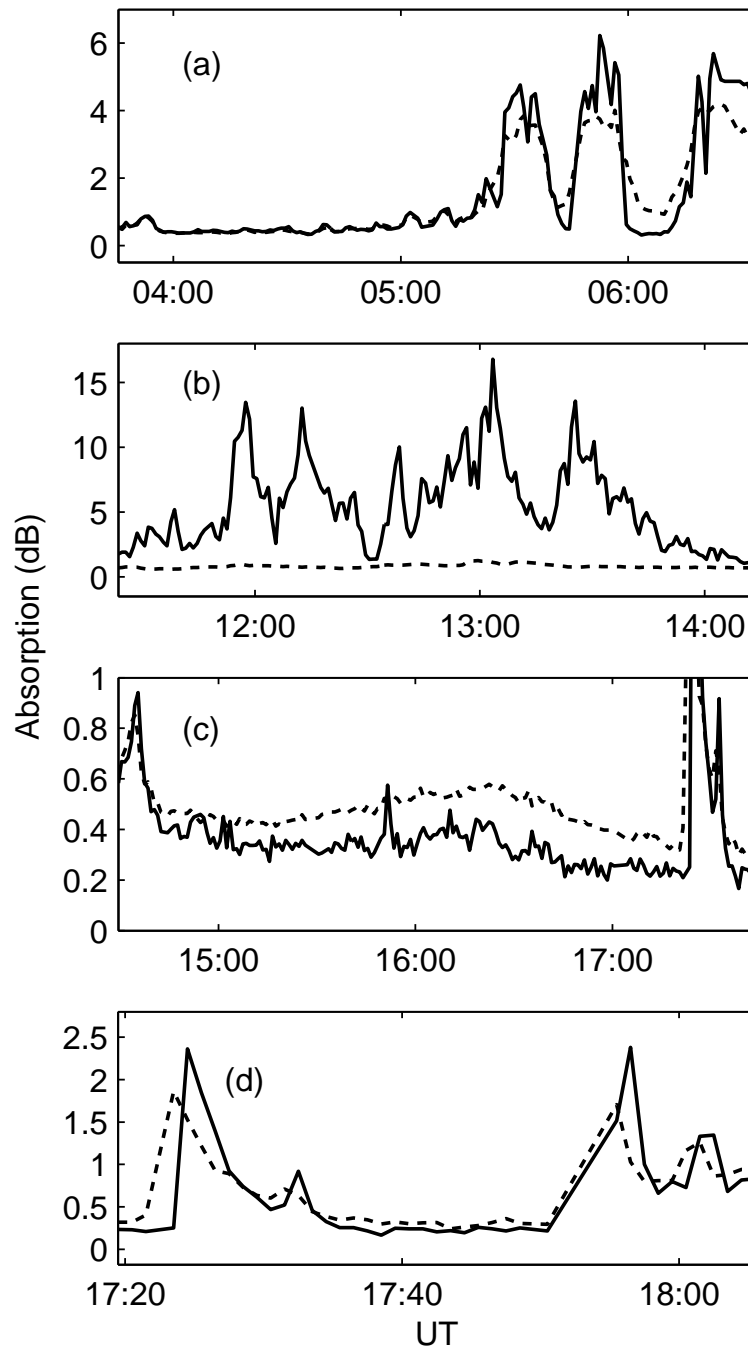
Figure 3.4: Subsets of data that show periods of poor correlation between absorption calculated using EISCAT and NRLMSISE-00 (solid line) and measured by beam 9 of IRIS (dashed line). (a), (b) are 2004–11–11; (c), (d) are 2004–11–12. For further explanation see text.

3.4.2 Sources of error

As well as the expected instrument errors encountered in the measurements, prominent sources of error include: calibration of the radar data, errors in the riometer quiet day curve and the different fields of view of the riometer and radar beams (see Fig. 2.5).

The field of view of the 9th beam of IRIS is closest to that of the vertically pointing radar, intersecting it at $\approx 80\,\mathrm{km}$ (Fig. 2.5). Although it is possible to interpolate between the riometer beams for the location of the radar beam at each altitude, the correlation between the instruments is hampered by the contribution to the other riometer beams from absorption further away from EISCAT. Fortunately, the absorption profiles are centred at approximately $80\,\mathrm{km}$, making the pointing direction of beam 9 ideal.

There are difficulties in calibrating the EISCAT VHF data directly with the dynasonde. Instead it is calibrated against electron density measurements from the EISCAT UHF radar, which is itself calibrated against the dynasonde. Comparing many samples of the UHF and VHF data from an overlapping altitude range on 2004–11–13, the median electron density ratio is found to be 1.84, the mean 1.90 and the total error in the mean 0.144 ($\approx 8\,\%$). The median value being the better choice as the values are not symmetrically distributed about the mean.

There are no error values given with the EISCAT power-profile data but an estimate of the random error can be taken from the data by comparing consecutive samples. The estimated error of the integrated modelled absorption, R_i, carried through from the radar data is:

$$\sigma_{R_i} \approx \sqrt{\sum_n \frac{(r_{i,n} - r_{i,n+1})^2}{2}} \approx 0.025 \text{ dB.} \tag{3.17}$$

Let m_i be defined as the measured absorption, c_i, minus the modelled absorption, R_i:

$$m_i = c_i - R_i. \tag{3.18}$$

σ_{R_i} is close to the noise-limit of IRIS and is small compared to the width of the distribution of m_i for this dataset, which is symmetrical but has a longer-than-Gaussian tail. This larger variability between the modelled (radar) and measured (riometer) values is almost certainly due to the separation of the instruments. Although it is impossible to know how the co-location error is distributed in altitude, assuming that it is constant allows for the use of combined error values, n_i. It is logical to assume, and can be clearly seen in the data, that this co-location error increases with increasing absorption.

Plotting the standard deviation of m_i for several subsets of data, binned according to c_i, gives an idea of the relationship between absorption, c_i, and combined (co-location and instrument) error. A good approximation, which forms the basis of the error values used, is found to be:

$$n_i = \pm \sqrt{([0.5 \, \mathrm{dB}]^2 + [0.5 \times \mathrm{c_i}]^2)}. \tag{3.19}$$

Several hours of scintillation occurred each night between approximately 22:00 UT and 03:30 UT (red lines, Fig. 3.3). The error estimate for these periods is increased accordingly. It should be noted that multiplying every value of n_i by a constant has no effect on the final result, but the errors of the result scale proportionally with the constant.

3.5 Results

Figure 3.5 shows that the effective momentum-transfer collision frequency profiles calculated using the NRLMSISE-00 model are very accurate in the 68 - 95 km range, with correction factors that are close to unity during both the active and quiet periods. Above 95 km the larger error indicates that the stability of the result is poor, this is due to the small contribution to the total absorption and a uniformity of absorption with respect to height at these altitudes.
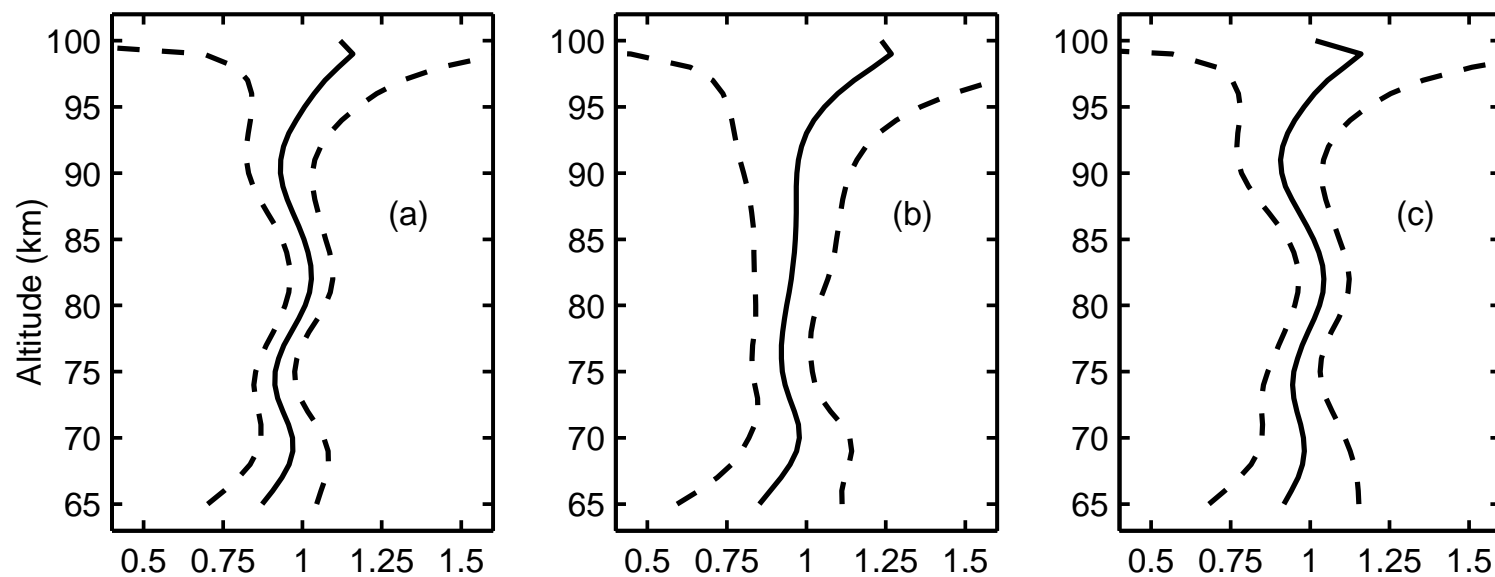
Figure 3.5: Correction factor, $\hat{u}$, for the effective momentum-transfer collision frequency given by NRLMSISE-00 (solid lines), with error bounds (dashed lines). (a) All of the data; (b) Active conditions ($ap > 50$); (c) Quiet conditions ($ap < 50$)

The apparent rise in the correction factor above 95 km, in both the active and quiet periods, is therefore thought to be a coincidence rather than a real trend. Generally, an absorption profile with an unvarying shape will present a badly posed inversion problem, supplying little information of the real-life contribution to integrated absorption (and thus collision frequency) from each altitude.

Below 68 km the result is smaller than unity, and less certain than might be expected. Clutter in the arc_dlayer-v program on the EISCAT VHF system was significantly reduced in June 2004 but may still remain a factor, (I. Häggström, private communication, 2007). This could be responsible for systematic overestimating in the power profile data from the lower range gates, leading to a reduced correction factor. The added uncertainty is caused by larger errors inherent in measuring very small electron densities, together with the rarity of patches of significant absorption at low altitudes.

The result for the entire dataset, Fig. 3.5(a), is closer to that of the quiet period, Fig. 3.5(c), simply because the majority of the data falls within the quiet period. The mean values of each correction factor profile between 70 km and 93 km, where the result is reasonably stable, are 0.965, 0.956 and 0.974, for all of the data, the active period and the quiet period respectively. Each of these factors differ from unity within the error of the calibration of the radar data ($\approx 8\%$). Therefore, the effect of the *ap* index on the effective collision frequency in the D-region is minimal, and less than the errors of the result. This confirms the assumption that *"ap effects are neither large nor well established below 80 km"*, suggested in the NRLMSISE-00 source code.

Without any regularization the inversion would be very badly posed, and the resultant profiles would oscillate wildly. In making the result smooth, the regularization has an effect similar to that of a low pass filter. Some residual oscillation is present in each of the profiles, but it is important that real features are not lost by overly constraining the result.
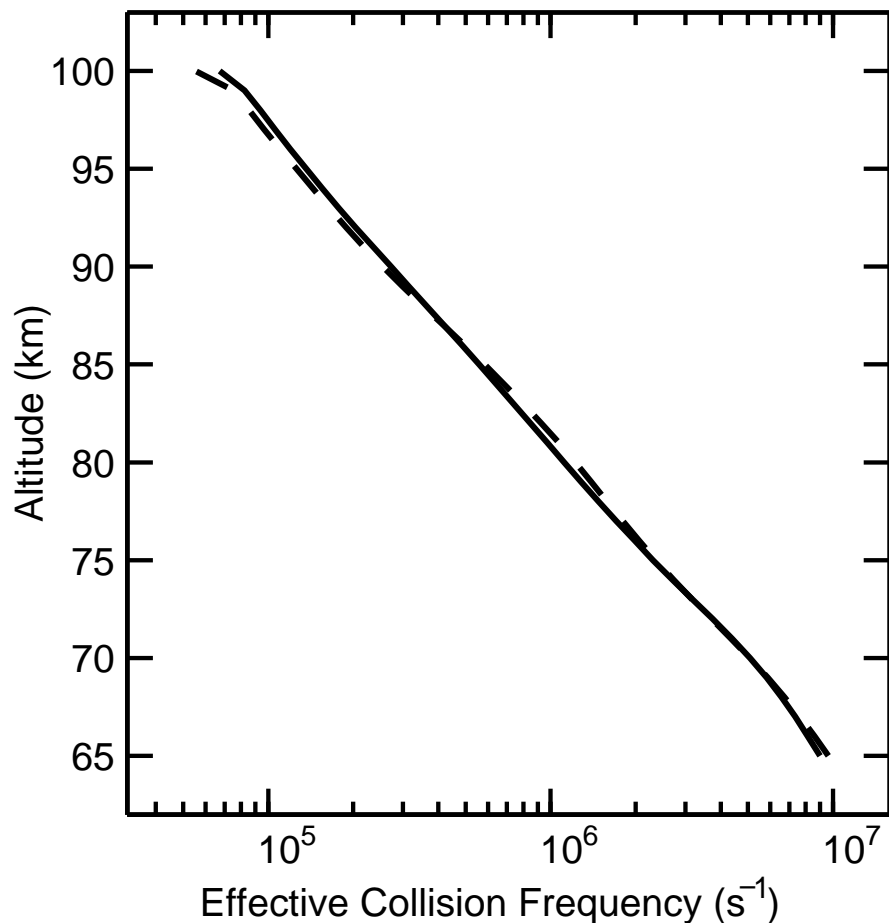
Figure 3.6: Corrected effective collision frequency profiles during active conditions at 2004–11–10 00:00 UT (solid line) and quiet conditions at 2004–11–12 00:00 UT (dashed line)

Multiplying the effective collision frequency profiles, calculated with values from the neutral atmosphere model NRLMSISE-00, by the correction profiles (Fig. 3.5), gives *corrected* effective collision frequency profiles. The corrected profiles for 2004–11–10 00:00 UT (active conditions) and 2004–11–12 00:00 UT (quiet conditions), are shown in Fig. 3.6.

In order to check that the regularization is not confining the result — beyond a reasonable amount — to the a-priori information, the program is re-run with various changes to the response kernel, r. Each profile of r (the model absorption per radar range gate) is multiplied by the functions depicted on the left hand side of Fig. 3.7 and the resulting variation in the solution, $\hat{u}_0$, is shown in the right hand side. For example, the top plot shows the effect of increasing the NRLMSISE-00 calculated absorption by 20 % at all altitudes. Ideally, the solution would then be compensated by a reduction of $100 \times (1 - 1/1.2) = 16.67$ % at all altitudes.

The changes in the result match very well with the ideal response for slowly varying functions of altitude, such as the first two examples, but narrow layers are less resolved. This is a reflection of the sensitivity of the result to similar variations in the actual neutral atmosphere.

Inspection of the set of inverse response kernels reveals that, when included in the dataset, PMWE contributes far less to the measured absorption than would be expected from such an increase in electron density. The same is true for the apparent enhancement in the EISCAT data (Fig. 3.3) at an altitude of 100 - 105 km on 2004–11–09 17:00 UT. Neither are thought to be real enhancements of electron density.
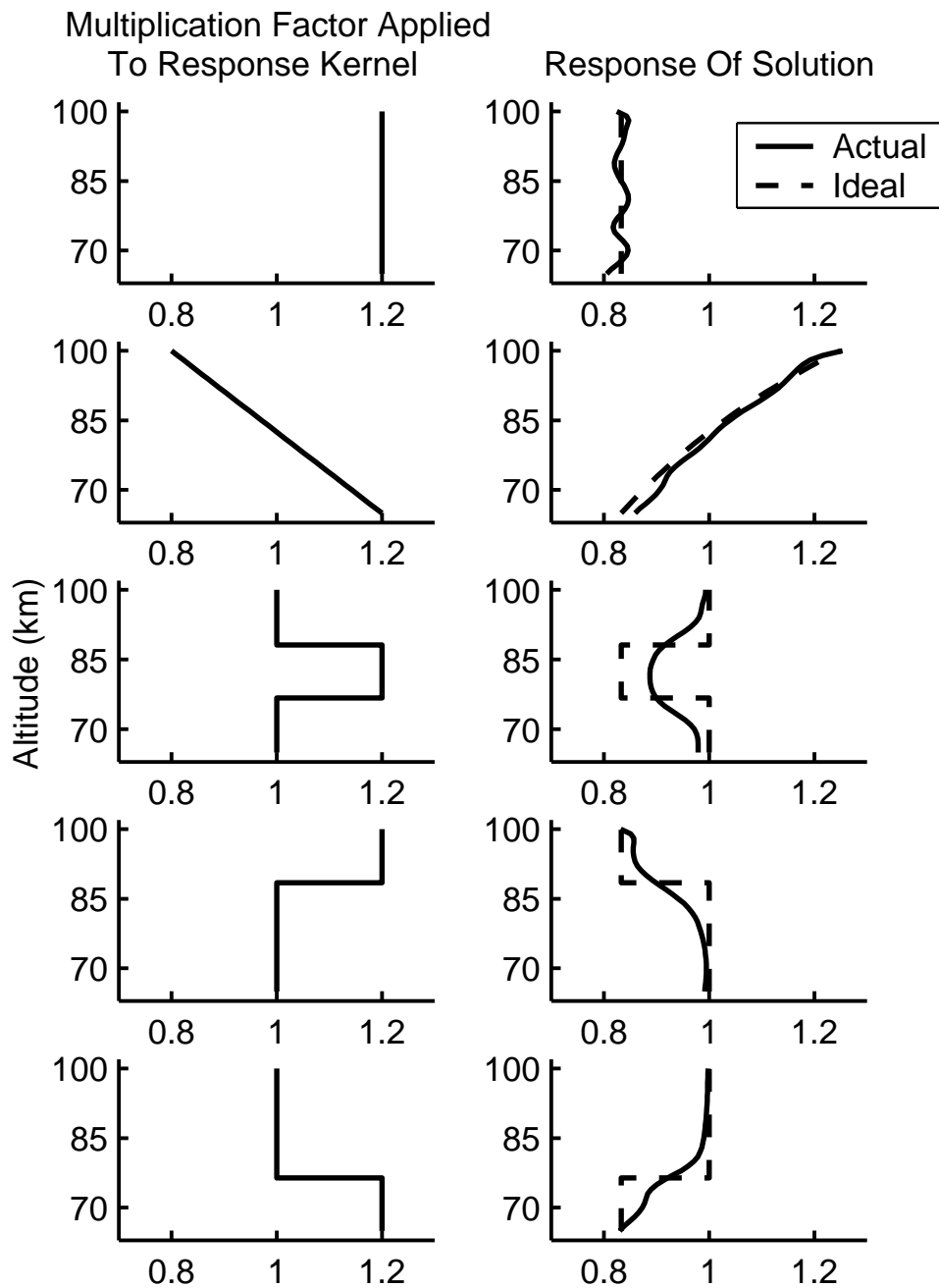
Figure 3.7: Response of the solution $\hat{u}_0(x)$ (right), to the multiplication factor
profiles (left) imposed on the response kernel, $r_i(x)$.

3.6 Conclusion

Within this chapter, a new technique has been demonstrated for measuring the effective electron-neutral momentum-transfer collision frequency profile in the D-region. The results match well with values derived from the NRLMSISE-00 neutral atmosphere model and show no detectable variation between the active and quiet periods. The method would be improved by using a riometer located at the radar site, with a comparable field of view. This would allow for higher altitude resolution, while reducing the errors (residual oscillations) in the result. Figure 2.5 suggests that ARIES should provide a significant improvement in this respect.

Direct comparison of the results with previous works is complicated by multiple definitions of the electron-neutral collision frequency. In the case of ν_M defined by Sen and Wyller's magneto-ionic theory, an added inconsistency arises from the invalid assumptions of temperature independent collisional cross-sections.

The corrected collision frequency profiles (Fig. 3.6) are in close agreement with the results of Miyazaki (1975) from a geographic latitude of $69°00'$ S. This is close to the southern hemisphere latitude corresponding to Tromsø ($69°35'$ N), and confirms that the log-linear altitude dependence assumed by Miyazaki (1975) is a reasonable approximation in the high-latitude D-region.

3.7 Extending the Backus-Gilbert Method to Three Dimensions

Inversion problems are commonplace in many branches of science, not least in geophysics and solar-terrestrial physics. One dimensional methods, as encountered so far in this chapter, are not applicable in all cases. For example, a medical Computerized Tomography (CT) scanner is required to produce three dimensional models from series of two dimensional images, while seismic surveys produce three dimensional models of Earth's interior based on the propagation of elastic waves through the Earth.

In a scheme that is similar to depth perception by pairs of eyes, the data from multiple nearby imaging riometers with overlapping fields of view can be inverted to produce a three dimensional model of ionospheric absorption. This process is known as imaging riometer tomography, and is presented here as a possible application of the Backus-Gilbert inversion method (see section 3.3), extended from one to three dimensions.

A three dimensional grid of voxels mapped to the ionosphere are labelled in a linear fashion, each as a single integer, v, from 1 to the total number of voxels. The contribution to the absorption measured by riometer beam i, from a unity value of differential absorption in voxel v, is r_{iv}. This forms the response kernel.

If the total absorption measured by beam i is c_i, with an error of n_i, then

$$c_i = \sum_v r_{iv} u_v + n_i, \tag{3.20}$$

where u_v is the underlying, or unknown, value of differential absorption in voxel v. (An assumption of this linear relation is that the variation in absorption across, but not necessarily along, the field of view of each beam is small.)

With a knowledge of the mapping from the Cartesian coordinates of the voxel locations, to corresponding integers v, the set of inverse response kernels can be defined as

$$\hat{u}(x, y, z) = \sum_i q_i(x, y, z) \cdot c_i. \tag{3.21}$$

The integrated response kernel, R_i, is unchanged from the one dimensional case

$$R_i = \sum_v r_{iv}. \tag{3.22}$$

As before, the variable λ enables tuning of the result between a stable solution and one that best fits the specific dataset. It is necessary to use separate values of λ for each of the directions x, y, z when uncertainties vary between the directions. In the present case, the uncertainty in altitude is larger than that of longitude or latitude. To accommodate these distinct λ, the variable is incorporated into the *spread-matrix*, W'_{ij}, with the apostrophe indicating this change in definition. The measure of spread, the reciprocal of resolution, is thus

$$\frac{A}{\lambda} = \mathbf{q(x, y, z)^T \, W'(x, y, z) \, q(x, y, z)}, \tag{3.23}$$

where,

$$W'_{ij}(x, y, z) \equiv \sum_v r_{iv} r_{jv} \left[\left(\frac{X_v - x}{\lambda_x} \right)^2 + \left(\frac{Y_v - y}{\lambda_y} \right)^2 + \left(\frac{Z_v - z}{\lambda_z} \right)^2 \right]. \tag{3.24}$$

Previously a solution was sought that minimized $A + \lambda B$, where B is the measure of stability (equation 3.8), but an identical result is found in minimizing $A/\lambda + B$.

$$\frac{A}{\lambda} + B = \mathbf{q(x, y, z)^T} \left[\mathbf{W'(x, y, z) + S} \right] \mathbf{q(x, y, z)}. \tag{3.25}$$

where S_{ij} is the covariance matrix (equation 3.9), based on the measurement errors, n_i.

The three dimensional solution, (previously equation 3.13), requires only

minor modification:

$$\mathbf{q(x,y,z)} = \frac{[\mathbf{W'(x,y,z)+S}]^{-1}\ \mathbf{R}}{\mathbf{R^T}\ [\mathbf{W'(x,y,z)+S}]^{-1}\ \mathbf{R}}. \qquad (3.26)$$

Once the response kernel, r_{iv}, has been calculated, based on the spatial gain of the riometer beams, the forward model (equation 3.20) can be used to simulate imaging riometer measurements for any 3D distribution of ionospheric absorption.

In figures 3.8 to 3.11, the forward model is used to simulate riometer data from a block of absorption (20 km in length and width, 10 km height), using beam patterns of the ARIES and IRIS imaging riometers. In each of the figures, the absorption block is placed in a different location and the inversion is performed to reveal the location and size of this absorption, albeit with a loss of resolution due to the limitations inherent with the instrument resolution.

An advantage of this method of tomography is speed, the matrix inversion of equation 3.26 needs only be calculated once. After which, each additional solution requires only simple matrix multiplication. The inclusion of incoherent scatter radar data could be achieved by treating each radar range gate as an individual beam, i, with an absorption value, c_i, calculated with knowledge of the neutral atmosphere (e.g. NRLMSISE-00), and using an appropriate error value n_i. Theoretically, this method could find the altitude of a layer of absorption that is completely uniform in the longitude and latitude directions. However, it is highly sensitive, and errors in riometer absorption measurements would disallow such an achievement.
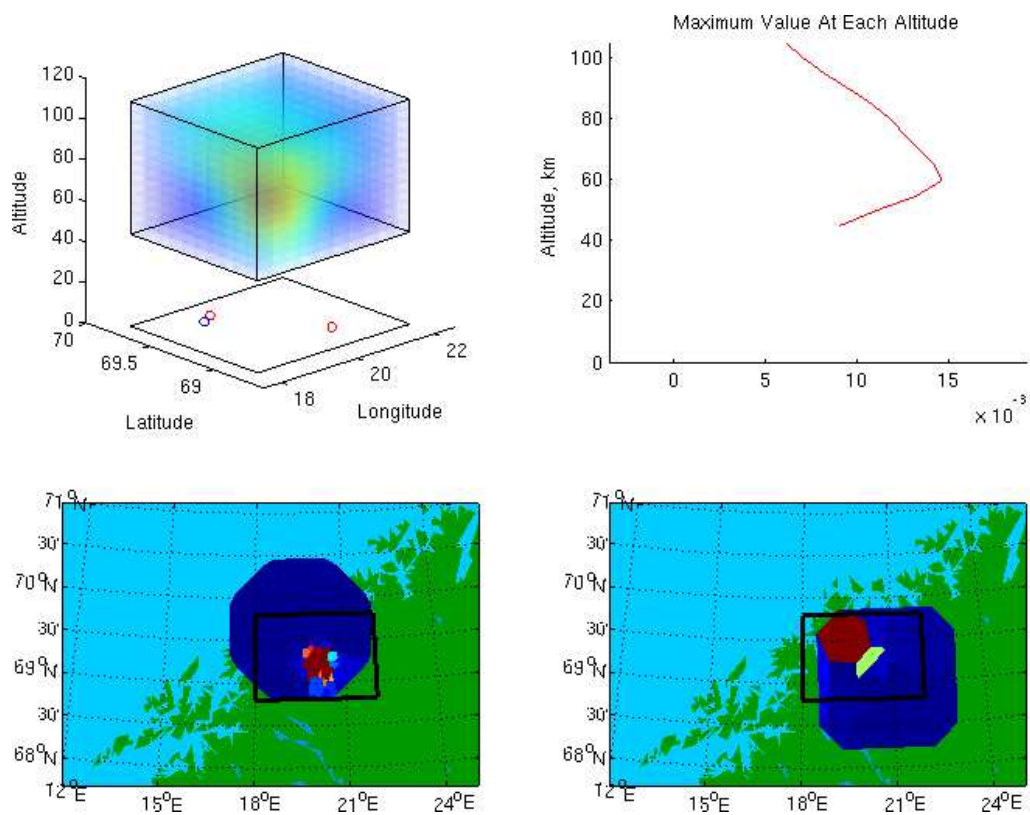
Figure 3.8: **Top:** Solution of the tomographic inversion, for the simulated absorption block (20 km in length and width, 10 km height), centred on 60 km altitude. **Bottom Left:** Simulation of ARIES absorption data. **Bottom right:** Simulation of IRIS absorption data.
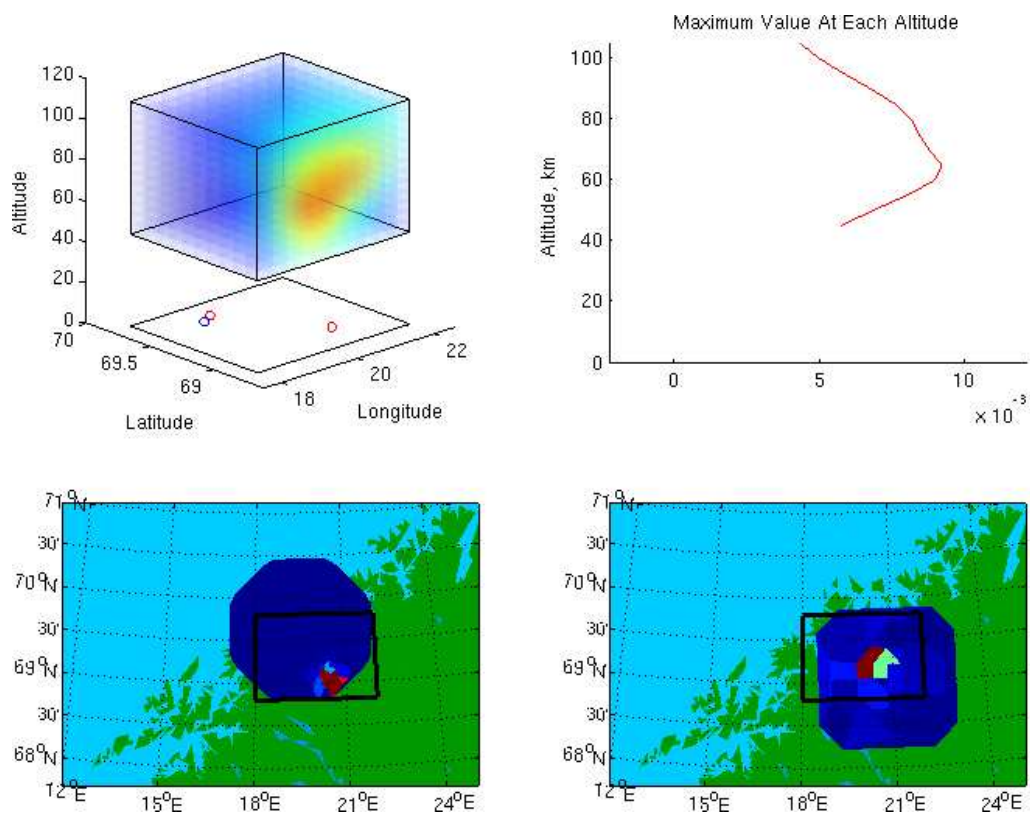
Figure 3.9: As Fig. 3.8, except with the absorption block toward the south.
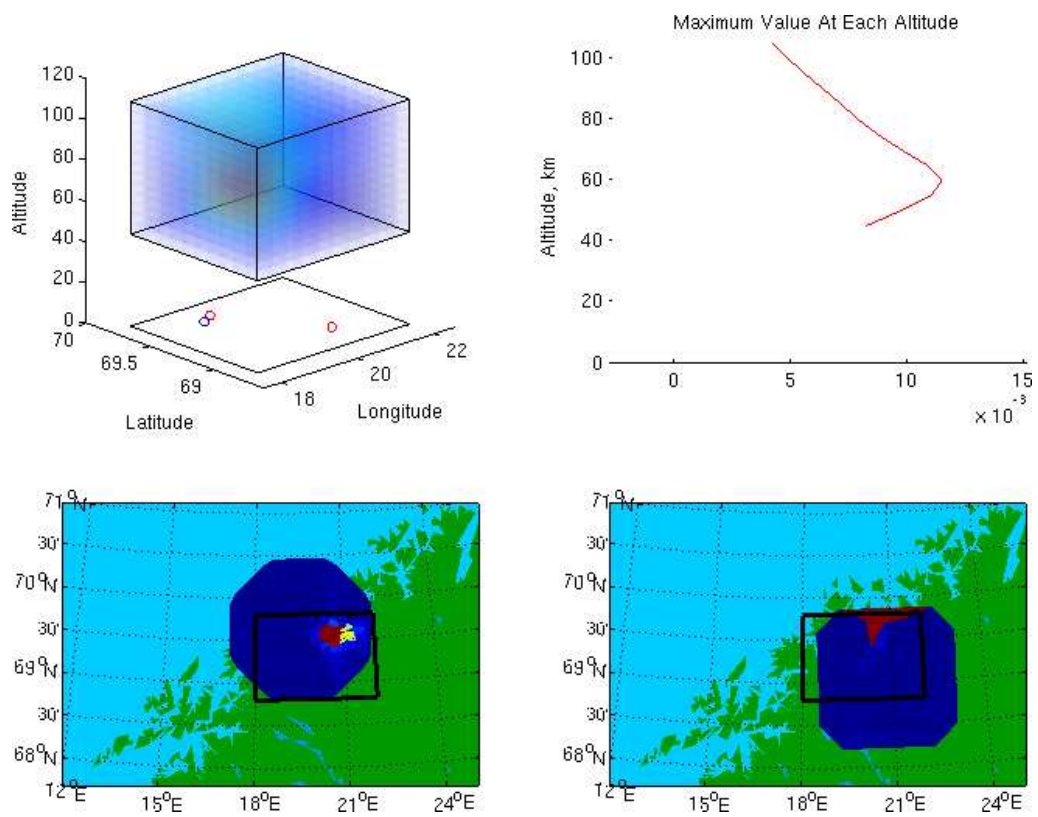
Figure 3.10: As Fig. 3.8, except with the absorption block toward the north.
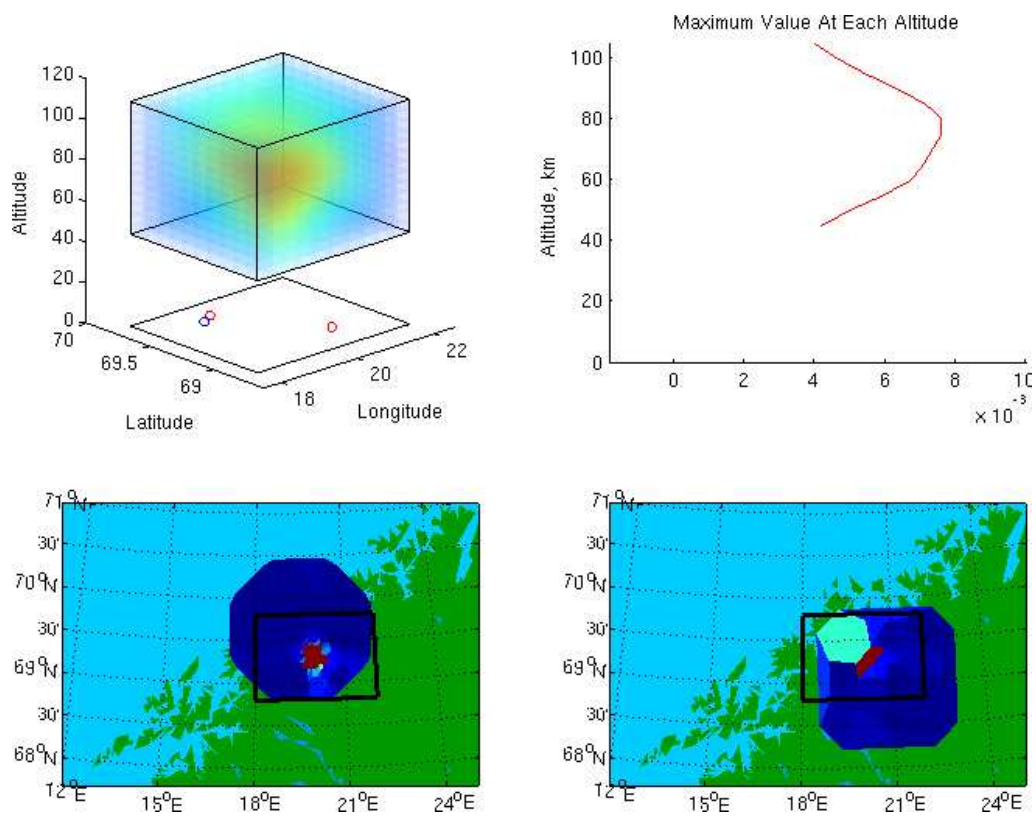
Figure 3.11: As Fig. 3.8, except with the absorption block at 80 km altitude.

Chapter 4

The Ionospheric Effect of a Solar Flare

The work presented in this chapter was conducted in collaboration with the Finnish Meteorological Institute, Helsinki, Finland, and the Sodankylä Geophysical Observatory, Oulu, Finland. It has been published as part of Enell et al. (2008), from which section 4.6 is taken. All other sections are the work of the author.

4.1   Introduction

Ionization by X-rays emitted from the hot solar corona and, to a greater extent, secondary ionization by the associated photoelectrons, occurs in the upper mesosphere and lower thermosphere. The flux of such short-wavelength radiation is highly variable. During flare events X-ray emissions from the solar corona can increase by several orders of magnitude (see e.g. figure 4.8).

Modelling of the ionospheric effects of large X-ray solar flares has previously been attempted by Tereshchenko et al. (2007) and Zinn et al. (1990), while other studies have observed the effects using satellites, such as TIMED (Woods et al., 2002), and the Student Nitric Oxide Explorer (SNOE) (Bailey et al., 2000). The electron density in the upper and middle atmosphere is enhanced during a flare, affecting the propagation of radio waves. On the 28 October 2003, an X 17.2 flare, which is central to this study, caused an enhancement in the cosmic noise absorption measured by IRIS that peaked at 1.3 dB.

In this chapter, photo-electron and secondary electron production rates in the high latitude ionosphere are modelled, together with high energy electron distribution functions. The former are used to extend the Sodankylä Ion-neutral Chemistry (SIC) model, in order to produce electron density profiles, which are found to be in agreement with observations, after an adjustment of the initial nitric oxide NO concentration.

Solar flares typically occur during active periods, when the preceding auroral activity, including proton events, may enhance NO by one to a few orders of magnitude (see e.g. Siskind et al. (1989)).

Nitric oxide is an important minority constituent of Earth's thermosphere, playing an significant role in determining the composition of the atmosphere above 100 km (Roble et al., 1987).

Mapping of the latitudinal variations of NO by Rusch and Barth (1975) revealed concentrations that were greater at high latitudes than at low latitudes. There are two major thermospheric sources of NO, auroral particle precipitation is thought to dominate at high latitudes, whereas solar X-rays dominate at low latitudes. This has recently been confirmed with correlations reported between solar soft X-ray measurements, and nitric oxide measured by SNOE as a function of latitude (Barth et al., 2003). While each mechanism is found to be dominant in a different latitude region, solar X-rays contribute to the density over the whole illuminated hemisphere. Similarly, auroral precipitation dominates between $67° - 70°$, but transportation by meridional winds extend its influence to mid and low latitudes (Barth and Bailey, 2004). Joule heating may also contribute to increased NO production during geomagnetic storms, due to the temperature dependent nature of the reaction between ground state atomic nitrogen and molecular oxygen (Dobbin et al., 2006).

A consequence of an abundance of nitric oxide is a greater thermospheric cooling rate, caused by the $5.3\,\mu$m radiative emissions by excited NO (Maeda et al., 1992). This has been observed following periods of enhanced geomagnetic and solar activity by the SABER instrument on the Thermosphere-Ionosphere Mesosphere Energetics and Dynamics (TIMED) satellite (Mlynczak et al., 2003)

Additionally, NO may be transported to lower altitudes (Seppälä et al., 2007), where enhanced densities contribute to the destruction of ozone (Ravishankara, 2009) via the reactions:

$$
\begin{aligned}
NO + O_3 &\rightarrow NO_2 + O_2 \\
O + NO_2 &\rightarrow NO + O_2 \\
net : O + O_3 &\rightarrow 2O_2
\end{aligned}
$$
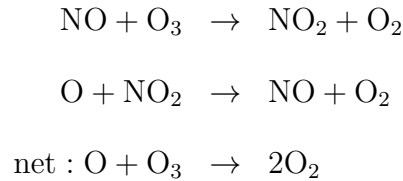
Following restrictions on the use of CFCs, nitrogen oxides have become the dominant ozone depleting substance of this century (Ravishankara, 2009). The role of NO in this process gives clear weight to the importance its study.

Comparisons made between SIC model results and EISCAT electron density measurements in section 4.6 will attempt to quantify the effect, if any, a large X-class solar flare has on the thermospheric concentration of nitric oxide, and provide a means of estimating the underlying levels.

4.2   The Extreme Flare of 28 October 2003

Halloween of 2003 coincided with an intense period of solar activity. On 4 November 2003 occurred the largest flare since records began in 1976. Based on VLF and riometer measurements, Thomson et al. (2004), and Brodrick et al. (2005) independently determined that the flare, which saturated the GOES detectors, had a magnitude in the range X40–X45 ($4.0 - 4.5 \times 10^{-3} \mathrm{Wm^{-2}}$ in the wavelength band 1–8 Å at 1 AU).
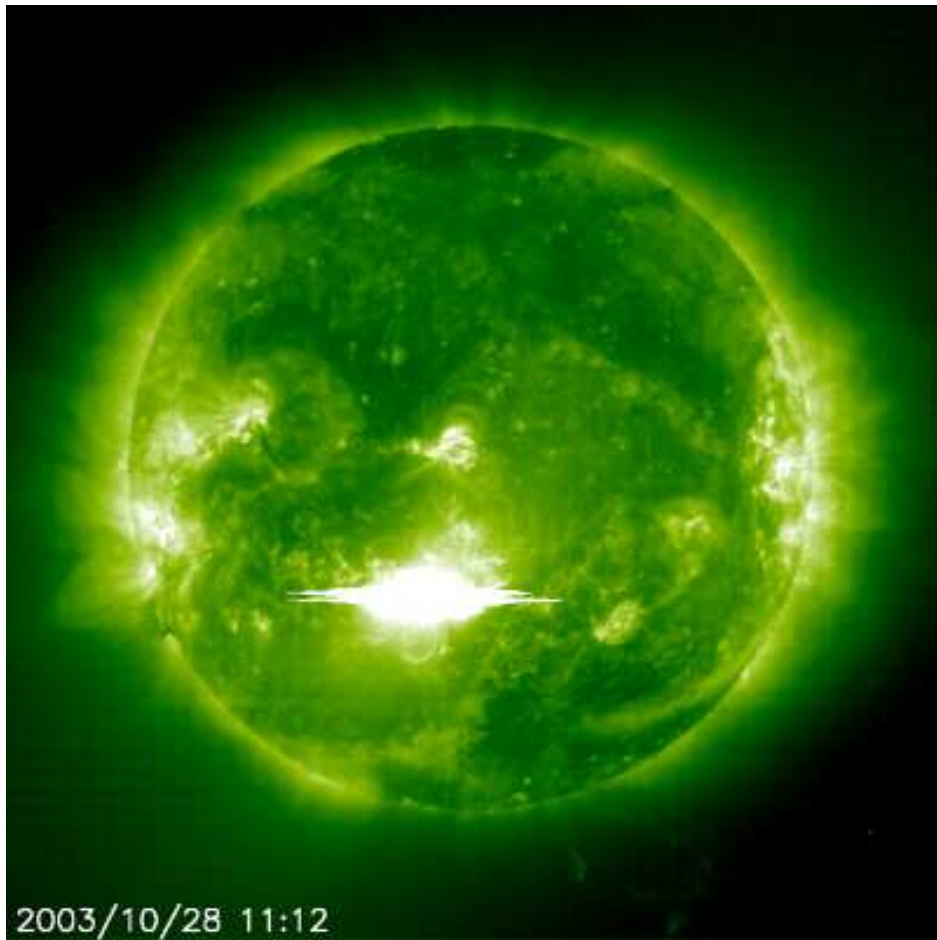
Figure 4.1: The October 28, X17.2 Solar Flare in extreme ultra-violet light (195 Å) by the SOHO/EIT (Extreme-ultraviolet Imaging Telescope).

On 28 October 2003, the same active region (NOAA 10486) was responsible for the 4th largest solar flare, measured at X 17.2/4B. Unlike the 4 November flare, this one occurred while Europe was in daylight, and the EISCAT VHF radar was running the arc_dlayer experiment, providing measurements of the ionospheric D-region. The GOES 10 and 12 satellites detected a rise in solar X-Ray radiation as early as 09:41 UT, however, the flare began proper at 11:01 UT, and peaked at 11:10 UT. At this time the active region was near the centre of the solar disk (20° west of the central meridian). The coronal mass ejection was therefore directed toward Earth, appearing as a halo. The fast moving CME hit Earth early on 29 October. In all 8 X-class solar flares were born of the active region NOAA 10486.

4.3 GOES X-ray Data

The two spectral channels of the GOES XRS system, $(0.1 - 0.8\,\text{nm}$ and $0.05 - 0.4\,\text{nm})$, can be fitted to a function approximating solar flare X-ray emissions. Figure 4.8 (Left) shows the 5-min integrated GOES-10 X-ray measurements during the event. The flare maximum, occurring at 11:10 UT, causes clipping in the higher energy channel, which is corrected by hand before fitting to the semi-empirical spectrum of Culhane and Acton (1970):

$$N(E) = C \cdot T^{-0.2} E^{-1.3} \exp\left(-\frac{E}{k_B T}\right) \left[1 - \left(\frac{E}{88.0}\right)^{0.33 k_B T}\right]^{-1}, \qquad (4.1)$$

where k_B is Boltzmann's constant, and E is the emitted photon energy in keV. Equation 4.1 contains two free parameters, a solar coronal plasma

temperature T, and a factor C representing a line-of-sight integral of coronal electron density. Thus it can be adjusted to reproduce values in the two spectral channels of GOES XRS, when integrated over the specified ranges.

The spectral model, equation 4.1, is appropriate for coronal temperatures less than 20×10^6 K. For the high coronal temperatures encountered at the peak of the flare, the spectrum for $T = 20 \times 10^6$ K is taken and shifted toward smaller wavelengths until the ratio of the GOES channels match corresponding values from the spectrum, and then C is scaled to reproduce the values of the data. The resulting spectra are shown in figure 4.2, with the corresponding coronal temperature parameter, T. For smaller, and subsequently cooler flares equation 4.1 is found to be appropriate without any modification.

The described fitting procedure may appear somewhat arbitrary, and it is known that an accurate X-ray flare spectra will contain many discrete coronal emissions, however, the computed ionization production rates between 60–90 km should be fairly insensitive to the exact shape of the X-ray spectrum (Zinn et al., 1990). During a large solar flare the majority of ion production in the D-region is by X-rays, and the associated energetic secondary electrons. At 90 km less than a third of the production rate is expected to be from solar radiation of wavelengths greater than 8 Å, a proportion that falls rapidly at lower altitudes (Tereshchenko et al., 2007; Zinn et al., 1990). Furthermore, this method has proven to yield results (electron density profiles) in agreement with observations.
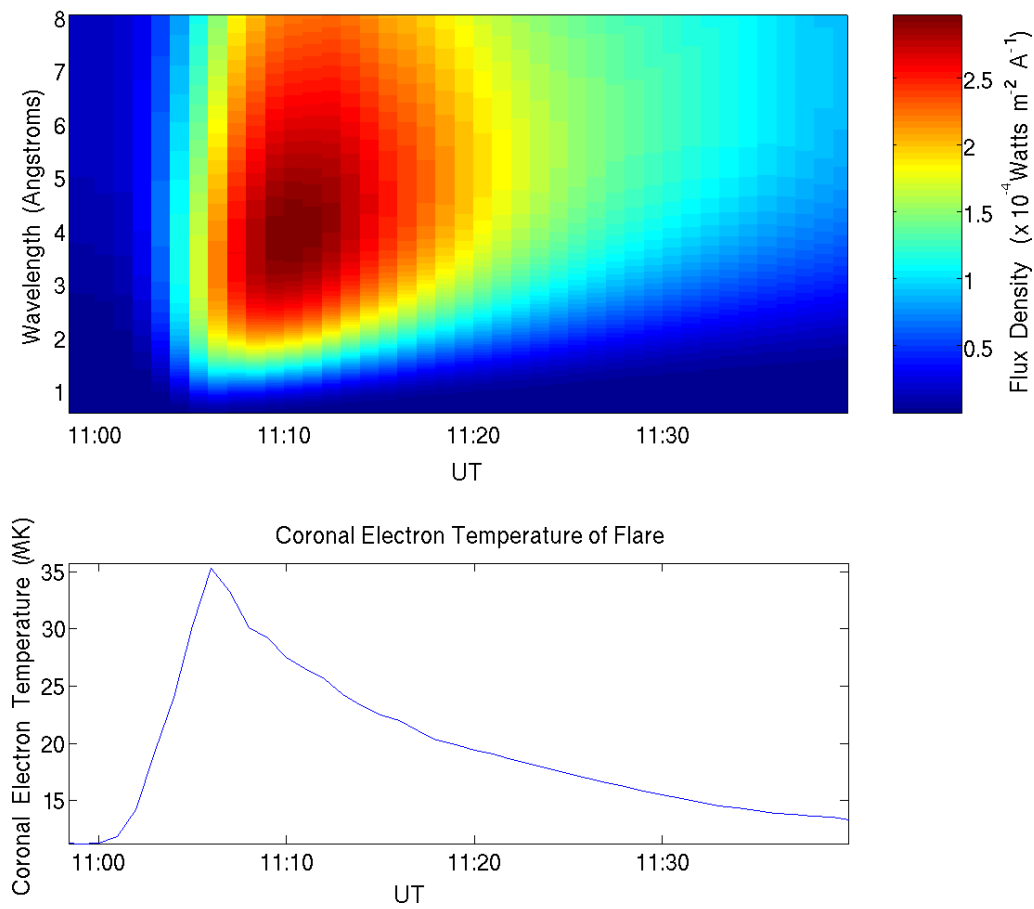
Figure 4.2: The Culhane and Acton (1970) spectra fitted to the GOES X-ray channels over the duration of the flare. **Top:** Photon flux density as function of wavelength and time. **Bottom:** The corresponding coronal temperature parameter, T.

4.4   Ionization Rates

The rates of X-ray flux conversion, to the production of photoelectrons, are numerically calculated for each wavelength (spectral bin) of the fitted X-ray spectra, by tracing through a model upper atmosphere (NRLMSISE-00). Photo-ionization cross sections for the seven most common neutral constituents are provided by the NIST XCOM database (Berger et al., 1998), four of these are shown in figure 4.3. An altitude of $500\,km$ is taken to be the effective top of the ionosphere, where the rate of X-ray deposition is insignificant.

In order to make comparisons with data from the EISCAT radars, the neutral atmosphere model is initiated for the location of Tromsø, with suitable geomagnetic and solar indices for the time of the event. The obliquity of the X-rays is important at the high latitude, and calculations for a spherical Earth are used. In late October the solar elevation in Tromsøis low, even at noon – throughout the event the solar zenith angle remains around $83°$.
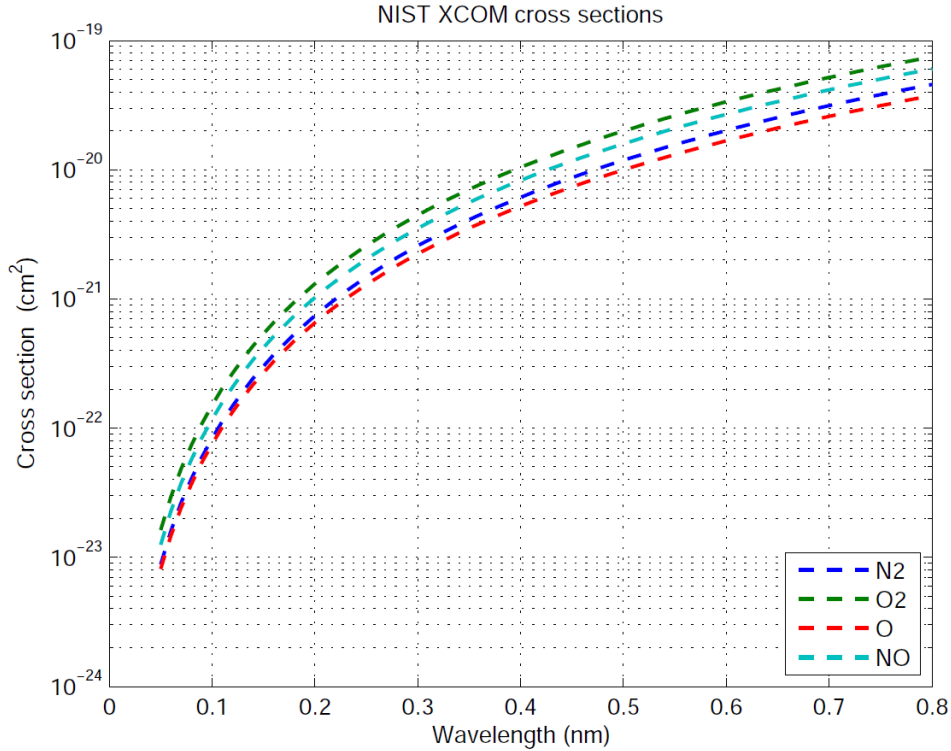
Figure 4.3: The X-ray cross sections of the major atmospheric species, as taken from the NIST XCOM database, (Berger et al., 1998).

4.5 The High Energy Electron Distribution

In this section the method of Jasperse (1976) is followed, in order to simulate the high energy electron distribution function, and the production rates of secondary electrons resulting from photo-electron collisions. Some assumptions of the nature of the ionospheric D-region are necessary: the high collision frequencies at these altitudes must allow for a steady state approximation, with negligible transport; attachment and recombination are neglected at high energies; and collision frequencies and the electron velocity distribution are isotropic.

By treating the energy loss to secondary electron production as an excitation process, the continuous slowing down approximation is employed, based on the Boltzmann-Fokker-Planck method:

$$F_0 \cdot \left(-\frac{\partial E}{\partial t} \right) = \int_E^\infty dE' \left(\frac{\delta F_0}{\delta t} \right)_{pi}, \tag{4.2}$$

where,

$$-\frac{\partial E}{\partial t} = E \cdot \left\{ \sum_j \sum_k \left[1 - \exp\left(-\frac{E_{jk}}{T_{ex}} \right) \right] \delta_{jk} \nu_{jk0} + \sum_j \sum_k \delta_{ijk} \nu_{ijk0} \right.$$
$$\left. + \sum_j \left(\delta_{nj} \nu_{mnj} + \delta_{ij} \nu_{eij} \right) + \frac{\nu_{ee}}{2} \right\}. \tag{4.3}$$

A subscript 0 indicates that this is the spherically symmetric part of the complete theory. Each ν represents a specific electron collision frequency, and the corresponding δ are the energy losses associated with each collision.

The right hand side of equation 4.2 represents the previously calculated photo-electron production rates, which contribute to the electron distribution function, F_0.

The electron-electron momentum-transfer collision frequency,

$$\nu_{ee} = 16\pi \left(\frac{e^2}{m_e} \right)^2 \ln \Lambda \frac{N_e}{v_e^3}, \tag{4.4}$$

(where $\ln \Lambda \approx 15$ is the Coulomb logarithm), is comparatively small, and can be neglected. Similarly for momentum-transfer collisions, ν_{eij}, between electrons and each ion state j.

In the case of high energy photoelectrons, and owing to the overwhelming proportion of neutrals in the D-region, the dominant terms in equation 4.3 are those of the elastic electron-neutral collisions, $\delta_{nj}\nu_{mnj}$, and the electron-neutral ionization collisions, $\delta_{ijk}\nu_{ijk0}$. The electron velocity, v_e, is much greater than the velocity of any neutral, so the elastic momentum-transfer collision frequency between an electron and neutral j depends only on the electron velocity,

$$\nu_{mnj} = N_j v_e \sigma_{mnj}. \tag{4.5}$$
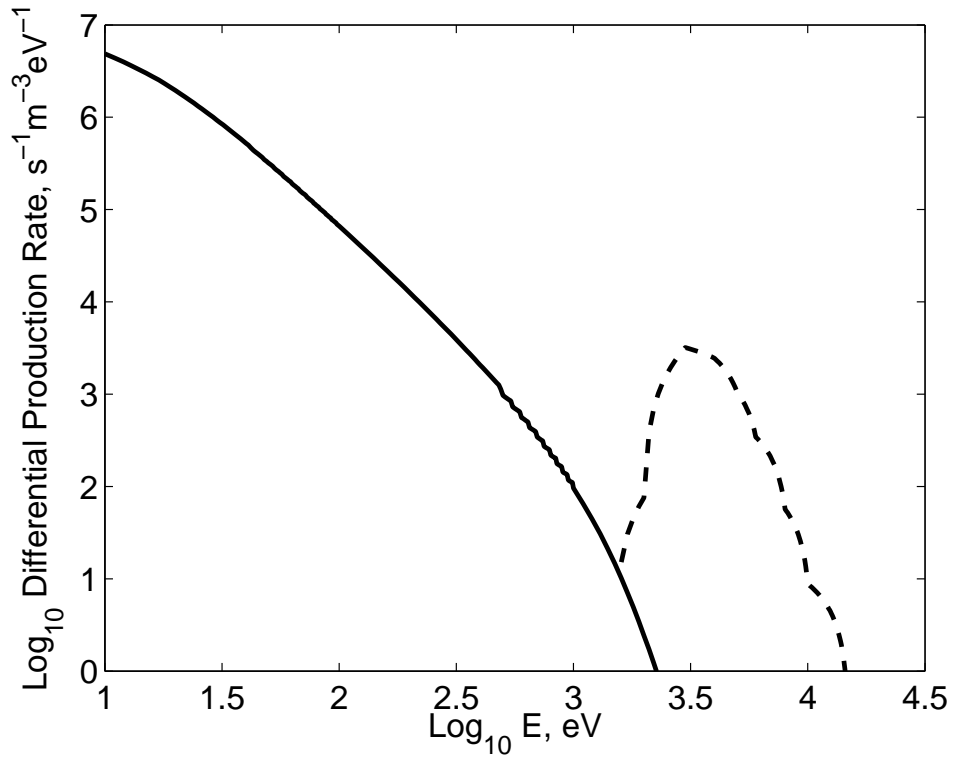
Figure 4.4: The differential electron production rates at 90km altitude. Dashed: photoelectrons. Solid: secondary electrons.

The corresponding energy loss per collision is

$$\delta_{nj} = 2\frac{m_e}{m_j}. \qquad (4.6)$$

For ionizing collisions,

$$\nu_{ijk0} = N_j v_e \sigma_{ijk0}, \qquad (4.7)$$

with a corresponding energy loss given by

$$\delta_{ijk} = \frac{E_{ijk} + \overline{E_{SE}}}{E}, \qquad (4.8)$$

where E_{ijk} is the threshold ionization energy in converting neutral j to ion k (see e.g. Hargreaves (1992), pp.223). $\overline{E_{SE}}$ is the average energy of an ejected secondary electron, found by integrating the differential ionization cross section,

$$\overline{E_{SE}} = \int \left(\frac{d\sigma_{ijk}}{dE_{SE}} \cdot E_{SE} \right) dE_{SE}. \qquad (4.9)$$

At this point the continuous slowing down differential equations, (4.2 and 4.3) can be solved, utilizing the ionization rates from section 4.4, with electron impact ionization cross sections taken from the NIST Electron Impact Cross-Section Database (Kim et al., 2010). For each altitude of the input photoelectron production rates, solutions to the partial differential equation are achieved numerically, beginning at the highest energies and progressing to the lowest, since each process can only affect the electron distribution at lower energies. The solutions provide the high energy electron distribution

function, F_0, and the differential secondary electron production rates.

The differential production rates of photoelectrons and secondary electrons, calculated for an altitude of 90 km, are shown as dashed and solid lines, respectively, in figure 4.4. The ratio of secondary-electron to photoelectron production rates (figure 4.5) fits the expected pattern – that of higher energy X-rays photo-ionizing at lower altitudes. The low altitude photoelectrons are ejected with more energy, subsequently producing a higher number of secondary electrons. An effect of the large solar zenith angle can clearly be seen, as the X-rays penetrate more atmosphere to reach the same altitude.
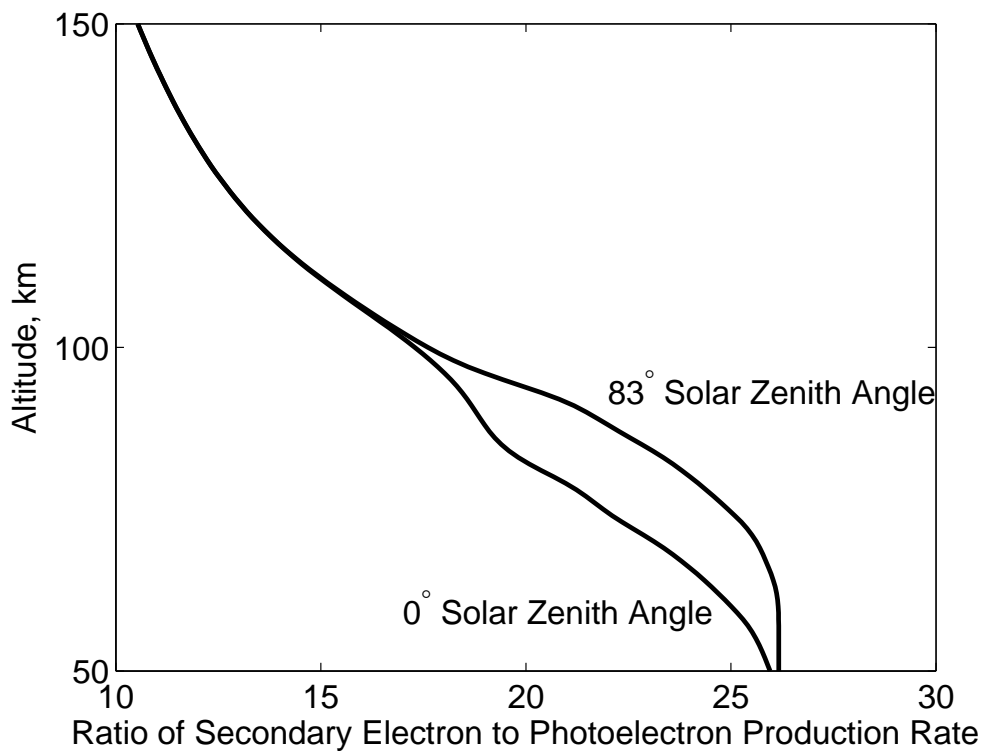
Figure 4.5: The calculated ratio of secondary electron to photo-electron production rates.

Presented in figure 4.6 is the high energy electron distribution function at 90 km, simulated by the continuous slowing down approximation. It is limited to energies above 50 eV in accordance with the assumptions made at the beginning of this section. The thermal electron distribution, assumed to be in a Maxwellian state, with a temperature taken from the NRLMSISE-00 model, is included.
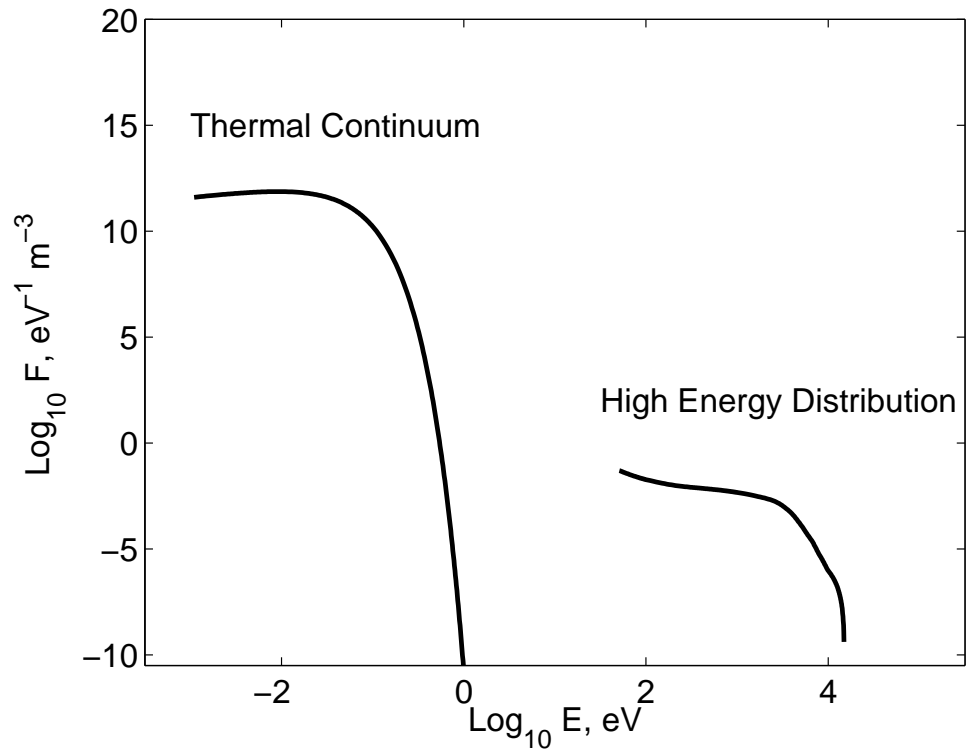
Figure 4.6: The calculated electron distribution function at 90 km, 28 October 2003 11:11 UT.

The effect of the high energy electrons on cosmic radio wave absorption at 38.2 MHz is calculated, using generalized kinetic dispersion formula (Garrett, 1985), and is found to be negligible compared to that of the thermal distribution. Thus, the enhanced absorption in IRIS (1.3 dB) has no significant contribution from the high energy photoelectrons, simply because they are too quickly thermalized by the high collision frequency of the D-region.

By incorporating the additional production rates arising from the X-ray flare, (figure 4.4), the Sodankylä Ion-neutral Chemistry model is extended into the hard X-ray region, and is used to investigate the effect of the extreme solar flare of 28 October 2003 on the D-region chemistry.

4.6 Effect of Solar X-ray Flare on D-Region Chemistry

SIC X-ray extension

For solar hard X-ray spectra, many empirical models are nowadays becoming available, such as the Solar Irradiance Platform that is to replace the current Solar2000 (Tobiska, 2000) model. For the present purpose, a simple analytical approximation is used. However, the possible choices of spectral models will affect the results and interpretation with respect to the adaptation of [NO] profiles, so a proper representation of the solar spectrum is an important issue for further studies.

From the SIC model results, altitude profiles of electron density are calculated as

$$N_e(h) = \sum_{i=1}^{36} [P_i(h)] - \sum_{j=1}^{27} [N_j(h)], \qquad (4.10)$$

where the sums represent the total concentrations of the positive and negative ions, respectively.

When setting up a new run, the SIC model is initialized by repeating a diurnal cycle with photochemical forcing only until a quasi-steady cycle is obtained. This method provides control (background) profiles for comparison of the results as well as initial concentration profiles of all modelled species for the event runs.
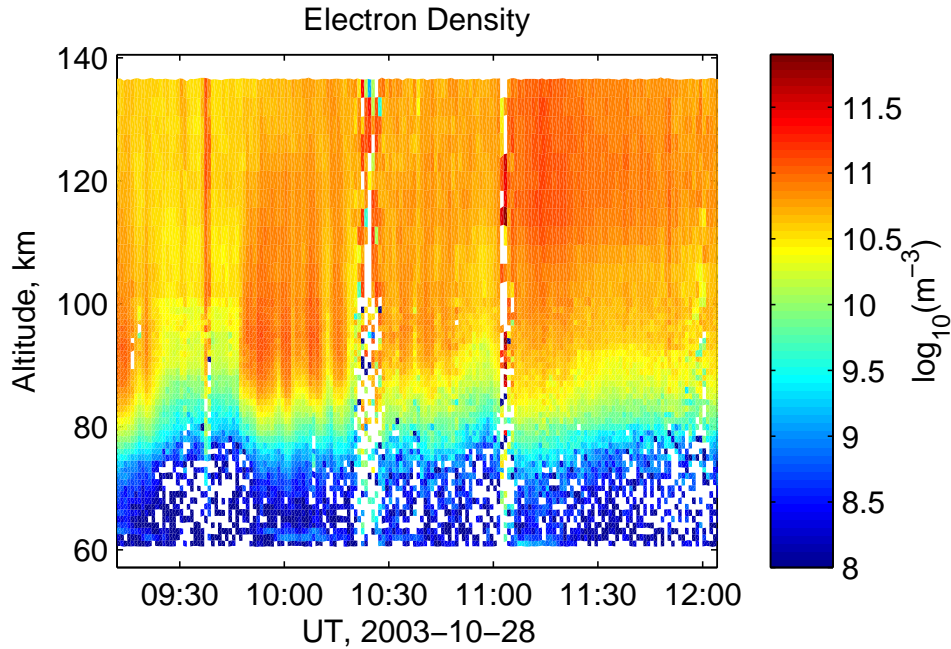
Figure 4.7: The 2003-10-28 X17 flare event. EISCAT electron density measurements prior to, and over the course of, the flare. The effect of the flare is seen beginning at 11:00 UT, peaking at 11:10 UT, and decaying over the course of an hour.

Data analysis

During the event the EISCAT VHF radar was running the high-resolution arc_dlayer experiment which is a pulse-to-pulse long-lag experiment with high time resolution for the ranges 60–140 km. The measured electron density profiles running up to, and during, the flare are shown in figure 4.7. The break in the data at 11:02 UT is likely due to radio interference from the broad-band noise emitted by the flare in its initial impulsive stage.

For analysing the experiment data, the Fukuyama and Kofman (1980) (henceforth FK) theory was fitted to the EISCAT autocorrelation function (ACF) profiles using the Metropolis-Hastings Markov Chain Monte Carlo (MCMC)

method (Hastings, 1970). MCMC is a random sampling procedure which automatically yields the posteriori distributions of the free parameters. The FK fit parameters are electron density N_e, electron temperature, ion velocity, ratio $\lambda = N_-/N_e$ of negative ion to electron density, and collision frequency ν_{in}. Since the MCMC method can, by definition, yield only results within the given a priori distributions of the parameters to fit, wide step-function type prior distributions were used. The calibration factor of the ACF profiles was estimated by fitting the first lags of the ACFs to the so-called raw N_e (N_e^*) profiles given by the standard EISCAT analysis software GUISDAP in the E region. Since ISRs do not measure the true raw backscattered power (zero lags of the ACF), GUISDAP calculates the N_e^* values from the 32μs pseudo-zero lags of the arc_dlayer experiment, automatically calibrating against the *foE* of the co-located EISCAT dynasonde (I. Häggström and M. Rietveld, personal communication).

Modelling

For modelling the 2003-10-28 case, the SIC model was initialized for the location of EISCAT at Ramfjordmoen near Tromsø, Norway (69.59°N, 19.23°E). The MSIS background atmosphere was calculated with the following parameters: $F_{10.7} = 217.8$ (solar 10.7 cm flux of the preceding day), $F_{10.7A} = 164.56$ (3-month average of $F_{10.7}$) and daily average $A_p = 22$. Calculations of ionization and dissociation of nitrogen and oxygen were included as in the standard SIC 6.8.1 model and in addition rates due to the fitted hard X-ray spectra, of which the right plot of figure 4.8 shows two examples, were included. The radiative transfer calculations were updated with 5-min time
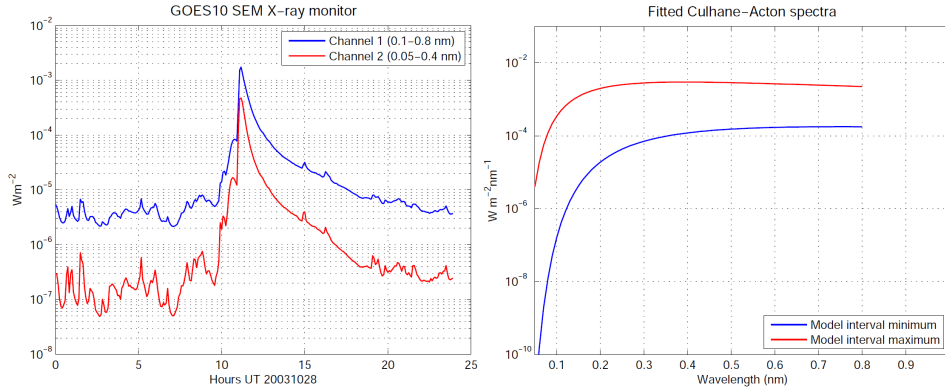
Figure 4.8: Left plot: The GOES X-ray channels for the 2003-10-28 event. It should be noted that the wider channel saturated during the maximum. Right plot: Fitted spectra for the maximum (around 11:10 UT) and minimum (X-rays switched on at 10:50 UT) fluxes during the model run. Similar spectra fitted to 5-minute average GOES data were used throughout the flare runs. The solar zenith angle was around 83° throughout the event, since it occurred close to local noon.

resolution together with estimates of vertical transport, etc., as described in Verronen (2006).

Scaling of nitric oxide

Nitric oxide (NO) is the main varying ionizable species in the altitude range of this study. During quiet times, solar Lyman α ionization of NO is the main source of the lower ionosphere. Hard X-rays, as well as auroral electrons and solar protons, efficiently ionize also the main constituents of the atmosphere, but here it is assumed that their concentrations are constant, given by the MSISE-90 background.

The odd nitrogen family ($NO_x = N + NO + NO_2$) is long-lived, the lifetime being from about one day in the solar-illuminated upper atmosphere up

to months in the polar night. Under such conditions transport of NO_x to lower altitudes and latitudes is important (Siskind et al. (1997), Callis and Lambeth (1998), Vitt et al. (2000), Seppälä et al. (2007)). The balance between the species is governed by photochemistry, so that most NO_x is converted into NO during daytime. The concentration of NO thus depends on transport and preceding production by auroral activity and proton events. [NO] has a maximum at altitudes between 100 and 120 km, where both soft X-ray radiation (1–7 nm) and auroral electron precipitation (assuming typical
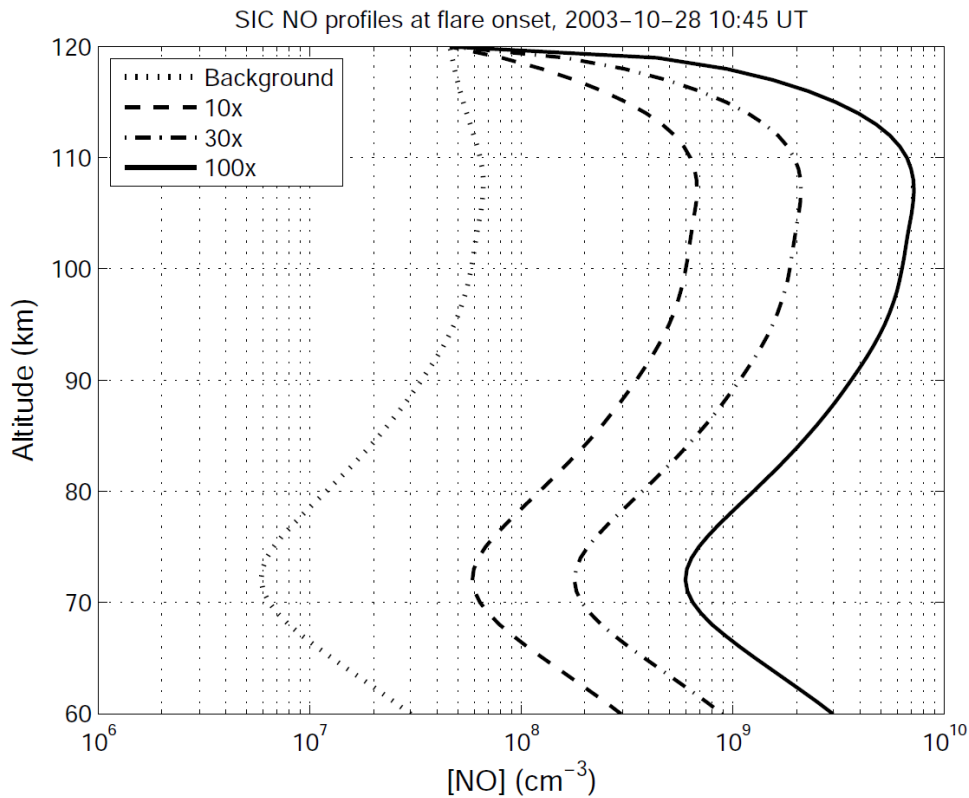
Figure 4.9: SIC model NO concentration profiles at the onset of the X17 flare of 2003-10-28, 10:45 UT. The initial profile was scaled by constant factors of 10, 30 and 100 at start of run (08:00 UT); thereafter the profiles change slowly by chemical reactions.

characteristic energies of 1–10 keV) dissipate most of their energy. As shown by SNOE the concentration of NO around the 110 km peak varies between 10^7 and 10^9 cm^{-3} at high latitudes. See the studies by Barth (1992, 1996), Siskind et al. (1998), Saetre (2004, 2007) for further discussions of these measurements and modelling of NO. A concentration on the order of 10^9 cm^{-3} in active periods can therefore be expected.

To account for this variability of [NO], the modelled and measured N_e profiles were brought into agreement by scaling the SIC initial concentrations of nitric oxide at the start of the model run (8:00 UT), multiplying by 10, 30 and 100. The model runs were continued without X-ray ionization until 10:45 UT, allowing the numerical solutions to settle to NO concentrations acceptably close to the observed range at the maximum. The resulting NO concentration profiles at 10:45 UT are shown in figure 4.9. X-ray ionization was switched on at 10:50 UT.

The left plot of figure 4.10 shows SIC modelled and arc_dlayer fitted electron densities for 09:45 UT, which was the time of a minimum in the electron density before the flare peak. The FK MCMC fit was done on data averaged over 9:25–9:45 UT. For the GUISDAP results the medians of the 1-minute profiles in the same time interval is used, bad profiles removed by manual inspection. Likewise, the left plot of figure 4.11 shows modelled and measured profiles for the peak, 11:10 UT. The EISCAT results were here averaged over 11:05–11:20 UT. The right plots show the relative difference between the FK MCMC fitted and the SIC model electron density profiles, $N_e(\text{FK}) - N_e(\text{SIC})/N_e(\text{FK})$, at the 1 km resolution of the SIC model runs. The agreement between SIC modelled and EISCAT arc_dlayer fitted electron

density clearly falls into three regions.

Region 1. 75–100 km:

The profiles agree well when starting with 30–100 times the SIC quiet background [NO]. This is not unreasonable since proton events occurred and auroral activity was very high during the days preceding the event and the following extreme "Halloween storm". We have previously modelled the effects of solar protons alone during this period, (Verronen et al., 2005). On October 28, 2003, SIC modelled [NO] in this altitude range was $10^7 - 10^8\,\mathrm{cm}^{-3}$, increasing even more after the following Halloween events. Taking also auroral electrons into account, a concentration of close to $10^9\,\mathrm{cm}^{-3}$ as in these cases (figure 4.9) is therefore not unrealistic. The exact shape of the modelled electron density profiles will depend not only on [NO] and the applied hard X-ray spectra but also on EUV, soft X-rays and particle precipitation. However, at the time of onset of this event it appears that simultaneous particle precipitation can be neglected.

Region 2. Above 100 km:

Before the flare onset (figure 4.10) the electron density is highly overestimated for the [NO] scaling required for best agreement at 75–100 km. As seen in figure 4.9 the model concentration of NO at the maximum near 110 km is close to $10^9\,\mathrm{cm}^{-3}$ or higher for all three scaling factors, so this scaling is possibly unrealistic. In that case, interpolation between the profiles can in principle be applied to obtain an estimate of the actual NO concentrations. However, part of the discrepancy, especially before the flare onset, can also be caused by the simple radiative transfer calculation overestimating soft X-rays and EUV at these altitudes for the high solar zenith angle of the
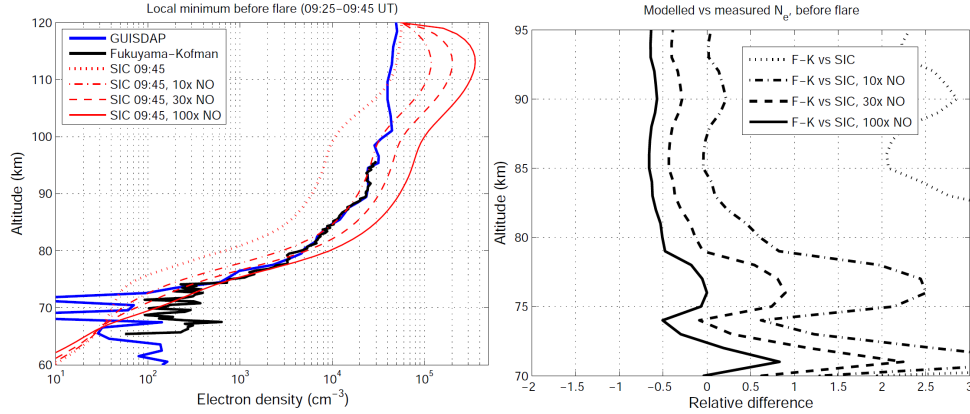
Figure 4.10: The 2003-10-28 X17 flare event. Left plot: SIC and EISCAT results before the flare onset. GUISDAP profiles are averaged over the minimum in electron density preceding the flare, 09:25–09:45 UT, bad profiles removed. The FK MCMC fit was applied to data averaged over the same interval. SIC was run without hard-X-ray ionization, the initial [NO] profile multiplied by 10, 30 and 100 at 8:00 UT. The SIC results are shown for 09:45. Right plot (N.B: altitudes restricted to 70–95 km): Relative differences between FK MCMC and SIC electron densities, $N_e(\mathrm{FK}) - N_e(\mathrm{SIC})/N_e(\mathrm{FK})$.
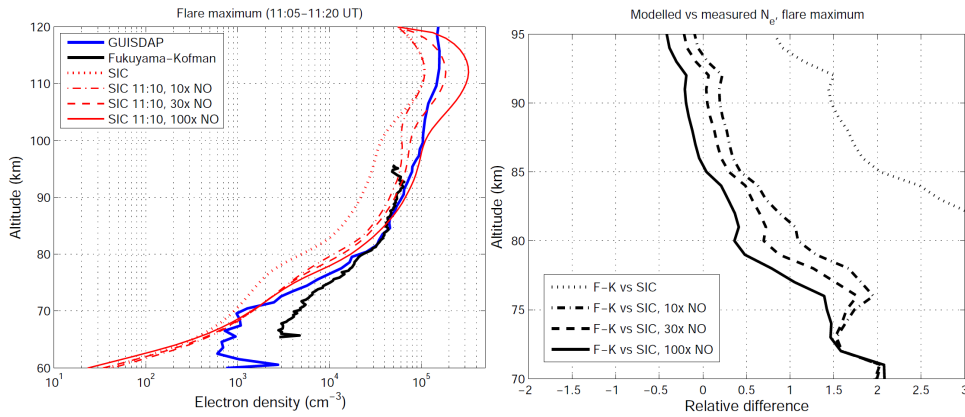
Figure 4.11: The 2003-10-28 X17 flare event. Left plot: SIC and EISCAT results at the peak of the flare. GUISDAP profiles are averaged over the period 11:05–11:20 UT. The FK MCMC fit was applied to data averaged over the same interval. In the model runs the hard X-rays based on the spectra fitted to GOES data were switched on at 10:50 UT. Results shown are for 11:10. Right plot (N.B: altitudes restricted to 70–95 km): Relative differences between FK MCMC and SIC electron densities, $N_e(\mathrm{FK}) - N_e(\mathrm{SIC})/N_e(\mathrm{FK})$.

event. This source of uncertainty should be eliminated by a proper radiative transfer calculation, but this is beyond the scope of the present study. More likely ionization by EUV and soft X-rays are underestimated at the flare maximum. Soft X-rays ($> 1\,\text{nm}$) and EUV are included as a daily average from the SOLAR2000 model, (Tobiska, 2000). Thus ionization by soft X-rays and EUV in the model run does not follow the flare development. In this case the lower concentrations of figure 4.9 are still correct.

Region 3. Below 75 km:

The scattering is affected by the high collision frequency, by the presence of negative ions, and possibly also by radar self-clutter (F-region backscatter from preceding pulses aliased into the lowest ranges). The latter is significant only below 65 km (I. Häggström, personal communication). The upper panel of figure 4.12 confirms that negative ions are significant below 70 km. The middle plot shows modelled and FK fitted values of the negative ion to electron density ratio λ for the flare maximum.

The GUISDAP and FK electron density profiles agree fairly well in the pre-flare case, but at the flare maximum the difference is large. The discrepancy between FK and raw N_e (the latter not shown in the figures) is small, however, and attributable to the negative ions. Turunen (1993) has shown that the Fukuyama and Kofman (1980) theory represents the effect of negative ions well. As figure 4.13 shows, the difference is likely caused by the fact that GUISDAP uses a fixed collision frequency profile whereas it is a fitted parameter in the FK MCMC retrieval. It can be seen that the FK fit reproduces the mesopause as a change in the gradient. The GUISDAP profile, calculated from the NRLMSISE-00 model (Picone et al., 2002) temperature
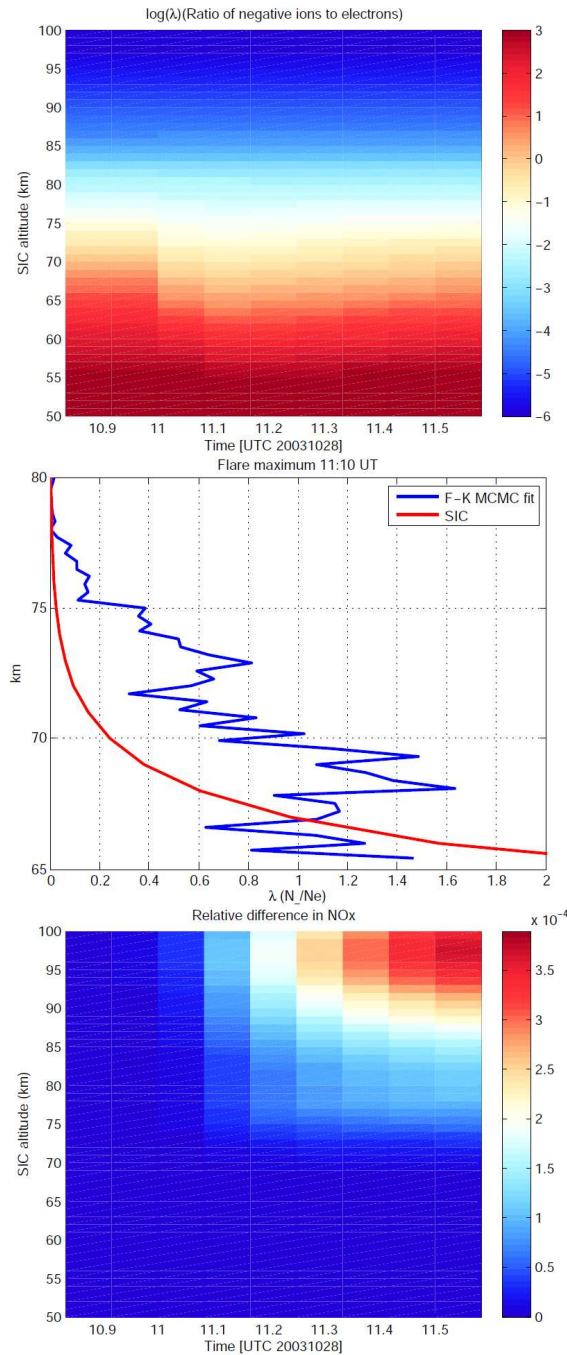
Figure 4.12: Upper panel: SIC modelled ratio, λ, of negative ion to electron density. Middle plot: SIC modelled and FK MCMC fitted λ for the flare maximum (11:10 UT). Lower panel: Relative $NO_x(N + NO + NO_2)$ enhancement due to the flare (event run vs control run for $100\times$ background [NO] at 8:00 UT). There is clearly no significant change here.

and densities of N_2, O_2 and O only, clearly lacks this feature. Thus, the actual electron density at the flare peak is not well reproduced by the model – the difference is at least a factor of two. Proton precipitation probably began around this time (see Verronen et al. (2005)), and the short wavelength region of the Culhane and Acton (1970) spectrum (equation 4.10) may not be a good representation of the actual solar spectrum, especially since one of the GOES detectors was saturated and the spectrum was adapted manually. The discrepancy may also be an indication that it would be necessary to introduce hard X-ray ionization earlier in the model run.

A narrow polar mesospheric winter echo (PMWE) is also visible at around 60 km. The strength of the PMWE appears to follow the X-ray ionization, which is expected since both ionization and some perturbations, likely turbulence causing a density modulation fulfilling the Bragg condition at the radar wavelength, are necessary for producing a strong echo.

The lower panel of figure 4.12 shows that the *change* in nitric oxide concentration due to the flare is completely negligible. The modelled relative change is less than 1/1000, whereas the SIC model initialisation is considered convergent for changes of less than a few percent per cycle. This does not mean that flares are not a possible significant source of atmospheric NO. Solar flare events affect the entire sunlit atmosphere and may last for several days. At lower latitudes, where the background concentration is orders of magnitude smaller due to transport and the absence of particle precipitation, flares are likely to enhance [NO] significantly. Refer to the SNOE observations, such as Barth (1992, 1996); Barth and Bailey (2004); Siskind et al. (1998).

Discussion

Preceding auroral activity and proton precipitation have evidently enhanced the [NO] background in the upper mesosphere up to $10^8 - 10^9 \, \mathrm{cm^{-3}}$. As seen in figures 4.10 and 4.11 the pre-flare result above $110 \, \mathrm{km}$ fits measurements without any scaling of the initial [NO] profile, whereas at the flare maximum the resulting electron density is too low. This is possibly due to underestimated soft X-ray fluxes. As mentioned, the issues of proper radiative transfer at high solar zenith angles also needs further investigation, since overestimates of the ionization rates may instead follow and therefore the higher [NO] values may still be correct.

Neutral chemistry changes are insignificant in these short-lived high-latitude events, but further model studies will address the importance at low latitudes. Finally it should be noted that effects of heating on atmospheric dynamics

during flares is also very likely of major importance, rendering the MSISE-90 model values unreliable, but this is beyond the scope of this paper. These questions are planned to be addressed by applying a version of the CMAT2 three-dimensional model (Harris, 2001) where the radiative code has been extended into the hard X-ray range (A. Dobbin and A. Aylward, personal communication).
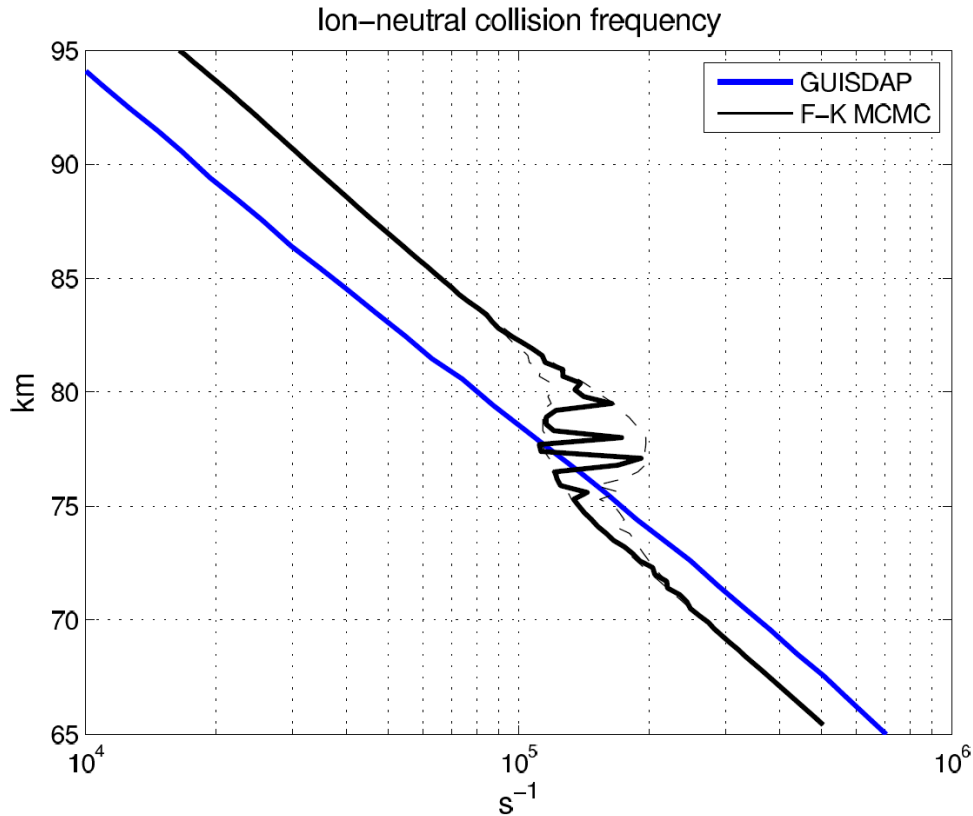
Figure 4.13: Comparison of the fixed ion-neutral collision frequency profile of GUISDAP, calculated from MSIS N_2, O_2, and O, and the Fukuyama-Kofman MCMC fit. The FK fit reproduces the mesopause well whereas the exponential GUISDAP profile, likely differing from the real one, may cause misinterpretation of the electron densities.

4.7   Conclusion

The D-region electron-ion production rates associated with a large solar flare are calculated, and a simulation of the high energy electron distribution function, using the continuous slowing down approximation, reveals that the population of hot electrons are too few to contribute to the measured cosmic noise absorption.

The work has led to the extension of the SIC model, to include the effects of solar X-rays. When combined with electron density profiles from the EISCAT radar, the model can be used to estimate the highly variable [NO] profile. However, this scheme is reliant on accurate electron density data – sometimes difficult to obtain during times of strong ionization, when the calibration by ionosonde measurements may be compromised. A knowledge of the underlying particle precipitation is also important, and in-situ measurements of [NO] during flare events would be ideal in order to verify the results. The effect of high X-ray flux on D-region ion chemistry is significant, but the neutral composition is little affected in the short time scale of a solar flare.

Chapter 5

On the Origin of High m Number Magnetospheric Waves

5.1   Introduction

Waves in the magnetosphere typically cover the ULF (ultra-low-frequency)
range, from $1\,\text{mHz}$ to $1\,\text{Hz}$, corresponding to the lowest frequency possi-
ble within the available space, to the gyrofrequency of charged particles.
Currents induced by these waves are often large enough to be detected by
ground-based magnetometers, and for this reason they were first observed
around 150 years ago (Hughes, 1994), prior to any knowledge of the existence
of the magnetosphere or ionosphere.

The introduction of photographic recording techniques revolutionized ge-
omagnetic research, and over the next century the widespread distribution of
magnetometers, with magnetic recording, enabled the classification of many
different types of event. An understanding of the mechanisms behind the
micropulsations began to follow. Dungey (1954) proposed that they might
be the signatures of standing Alfvén waves, known as field line resonances
(FLR). Within 10 years the theory was confirmed when pulsations were
observed to occur at each end of the same field lines (in the northern and
southern hemispheres) with the phase differences between each end indicating
an odd mode standing wave (Nagata et al., 1963).

The all-sky integrating nature of magnetometers does not allow for the
detection of small scale waves, as peaks and troughs will cancel each other
over the whole field of view. However, pulsations in the precipitation of
energetic electrons ($> 30\,\text{keV}$) have long been observed in cosmic noise

absorption (CNA). These pulsations often appear in riometer observations, and have previously been linked with micropulsations. Spanswick et al. (2005) matched precipitation pulsations with field line resonances, while Senior and Honary (2003) identified a westward propagating wave in the IRIS riometer, which they attributed to modulation via a drift or drift-bounce resonant wave, i.e. a ULF wave in resonance with a magnetospheric charged particle population.

The variations in D region electron densities caused by precipitating electron pulsations have also been observed with ionospheric radar. Yeoman and Wright (2000) conducted a detailed case study of an event on 18 October 1999, with the CUTLASS HF radars. Three distinct waves were identified. The first had a large scale nature, suggesting a driving source external to the magnetosphere, whereas the second and third had smaller azimuthal scale lengths, suggestive of an internal driving mechanism.

Occurring mostly during the morning and early afternoon, eastward propagating waves with high azimuthal wave numbers (m numbers) are an interesting, yet common, subset of CNA pulsation. Kikuchi (1988) employed a scanning beam riometer to measure the period and velocity of 19 such waves. He reported that this newly discovered type of pulsation occurred between 5 and 10 MLT, and had a short azimuthal wavelength, corresponding to an m number of $20 - 180$. The eastward direction led him to conclude that "the primary source must be located in the night-side magnetosphere", an assumption this work shall dispute.

There is some uncertainty as to when the first riometer observation of a high m number wave took place. Many publications report moving patches of absorption, often repeating with regularity (see e.g. Makarevitch et al. (2004); Kainuma et al. (2001); Nielsen (1980); Hargreaves (1970)). Differentiating between waves and moving patches of absorption is not straight forward. While most would argue that a wave is observed in-situ, whereas a moving patch of absorption is simply a fossil that has been transported from its generation region, Kikuchi (1988) reported frequencies and wave numbers of events that were believed to have travelled far from their formation in the night-side. On the other hand, Makarevitch et al. (2004) presented moving absorption patches that bear great resemblance to the waves analysed in this chapter. An example keogram therein shows several equally spaced repeating arcs of absorption that, when analysed as a wave, have a frequency of $1.1\,\mathrm{mHz}$, and an m number of $\sim +60$. These values are in line with the events studied in this chapter. An m number of $+60$ is not particularly large, but this is to be expected since Makarevitch et al. (2004) were using IRIS, a 49 beam imaging riometer with relatively low spatial resolution.

The Advanced Rio-Imaging Experiment in Scandinavia (ARIES), is a new type of imaging riometer with a spatial resolution of less than 10 kilometres at zenith, and over five hundred individual beams. It has provided the greatest imaging resolution of any riometer to date, and facilitated the identification of a large number of high m number waves (up to $m = 380$,) within a single 6 month period. This latest advance in instrumentation means that, for the first time, evidence is available for the complete generating mechanism of

these waves, beginning with a source external to the magnetosphere, and
ultimately resulting in the observed structured cosmic noise absorption.

Many studies have considered unstable magnetospheric particle popula-
tions as a source of high m ULF waves (e.g. Baddeley et al. (2004, 2002);
Yeoman and Wright (2000)). Although the origin of these unstable particles
remained uncertain, Baddeley et al. (2004) set out to test the relationship
between high m number waves and particle populations, finding excellent
agreement between the energy in magnetospheric ion distribution functions,
and the corresponding energy dissipated by high m waves in the ionosphere.

The distribution of solar wind energy within the magnetosphere has long
been a hot topic. Recent work (Turner et al., 2009), set out to quantify
the partitioning of solar wind energy. The Epsilon parameter of Akasofu
(1981) was used determine the energy input, and several magnetospheric and
ionospheric sinks were considered, allowing for a calculation of the efficiency
of the system. In the proposed generation mechanism, the path of energy
is traced from its sink in the ionosphere, back to it's source in the solar
wind. The magnitude of energy transferred to the secondary high m number
waves is small compared to the total transferred in the system. However, it
is unclear how much is lost along the way, in what could be a substantially
inefficient process.

It is accepted that cavity modes excite toroidal Alfvén waves, with par-
ticularly strong coupling where the compressional wave frequency matches

the natural resonance of the field line. This is an important process in the energization of charged particles. In section 5.3.5 a simple box model of the day-side magnetosphere is employed to help qualitatively describe the coupling. Toroidal Alfvén modes are capable of energy exchange with the magnetospheric charged particle population, through Landau *and* inverse Landau damping of particles close to drift-bounce resonance. The former has previously been overlooked, but is a key process in the generation of high m number waves

5.1.1 Generation mechanism overview

The generation mechanism of high m number waves can be broken down into the 5 steps shown in figure 5.1.

Solar wind pressure pulses on the day-side magnetopause excite quantized standing waves in the magnetospheric cavity. These compressional modes couple to toroidal Alfvén field line oscillations, which share the low azimuthal wave numbers of the cavity modes.

Drift-bouncing magnetospheric protons are accelerated by the toroidal waves though Landau damping, causing a bump to appear on the tail of the proton energy distribution. Following a reduction of the initial driving wave, this free energy becomes unstable to inverse Landau damping, and a secondary toroidal wave is generated.

The energy of a proton in resonance with a wave is determined by both the frequency and the azimuthal wave-number of the wave. As a consequence, secondary waves take a range of frequencies and azimuthal wave-numbers, while obeying a dispersion relation determined by the proton energy. Distinctive, high azimuthal wave-numbers are often observed.

By modulating the growth of whistler mode waves, and subsequently, the pitch-angle scattering of electrons into the loss cone (Coroniti and Kennel, 1970), images of these ULF waves appear in the cosmic noise absorption measured by riometers.

```
┌────────────────────────────┐
│   The solar wind drives dayside   │
│        cavity mode waves          │
└────────────────────────────┘
               ▼
┌────────────────────────────┐
│     Mode conversion takes         │
│  place from poloidal to toroidal  │
└────────────────────────────┘
               ▼
┌────────────────────────────┐
│   Energization of drift-bouncing  │
│    protons via Landau damping     │
└────────────────────────────┘
               ▼
┌────────────────────────────┐
│  Inverse Landau damping drives    │
│    a high m secondary wave        │
└────────────────────────────┘
               ▼
┌────────────────────────────┐
│     Secondary wave modulates      │
│      electron precipitation       │
└────────────────────────────┘
```
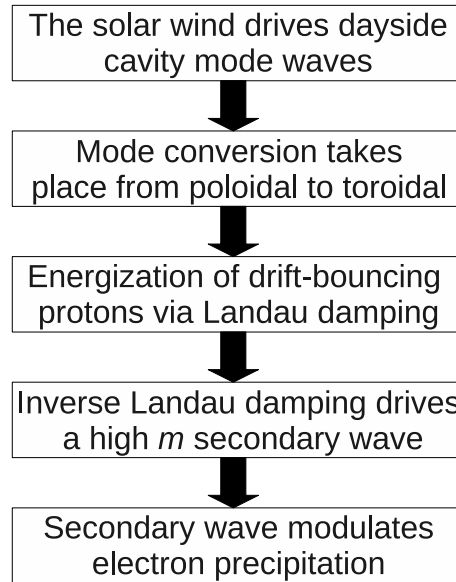
Figure 5.1: An overview of the proposed generation mechanism.

5.2 ARIES Results

The times of all of the detected high m number wave events are displayed in figure 5.8. There is clearly a relationship between solar wind activity and observations of high m number waves. Since they require a source of protons for drift-bounce resonance, and electrons for precipitation, it is not unexpected that pulsations tend to occur following substorm activity, when charged particles are drifting toward the day-side magnetosphere. If high m waves are not observed, it could be due to a lack of particles, rather than an indication that magnetic pulsations are absent.

In analysing data from ARIES, *cross-power*, the Fourier transform of the
cross-correlation function, and *cross-phase*, the frequency dependent phase
difference, are calculated for pairs of equi-latitudinal beams. 42 beam pairs
located close to the zenith are employed. Cross-power is also defined as
the product of the two Fourier transforms, where one of them has been
complex conjugated. Within this chapter, plots labelled cross-power are the
magnitude of this complex term, while the cross-phase is the phase angle.

Azimuthal wave numbers (m numbers) are determined from the cross-
phase, and the known ARIES beam spacing, with an assumption that peak
absorption is at an altitude of 90 km. Results from beam-pairs are averaged to
reduce error, and searched for wave-like structures with frequencies between
0.3 and 17 mHz. Neighbouring beams are paired when analysing large m
number events, whereas to improve accuracy neighbour-but-one beam pairs
are chosen for m numbers below 250. ARIES is aligned geographically;
although it is not feasible to pair beams of the same geomagnetic latitude
without severe aliasing due to a wide beam separation, the effect of this
rotation is expected to be, at most, a few percent in the calculated m
numbers.

Phase maps of two frequencies present during a typical event on 17
January 2007 are shown in figure 5.2. These illustrate the relative phase
of each beam, in radians, filtered at a specific frequency. The 0 point is
arbitrary. Cross-power and cross-phase spectrograms for the morning of 17

January are shown in figure 5.3, in which other waves can also be seem: a low m number wave at 01:00 UT, and a westward wave at 11:00 UT. For the 05:30 UT high m event, unfiltered data from 5 neighbouring ARIES beams, and the X (north) components of two nearby magnetometers are given in figure 5.4. Clear phase differences are visible across the ARIES beams. The magnetometers at Tromsø (69.66°N, 18.94°E), and Andenes (69.30°N, 16.03°E) are not capable of detecting waves with small spatial scales, as they effectively integrate over a wide area of sky, instead they respond to a concurrent $7 - 8$ mHz large scale wave, which is observed between 05:15 UT and 06:00 UT, and thought to be the driver of the event. A similar integration effect is seen in the western most riometer beam, where the dip in received power at 05:24 UT is smoothed due to the larger beam size.
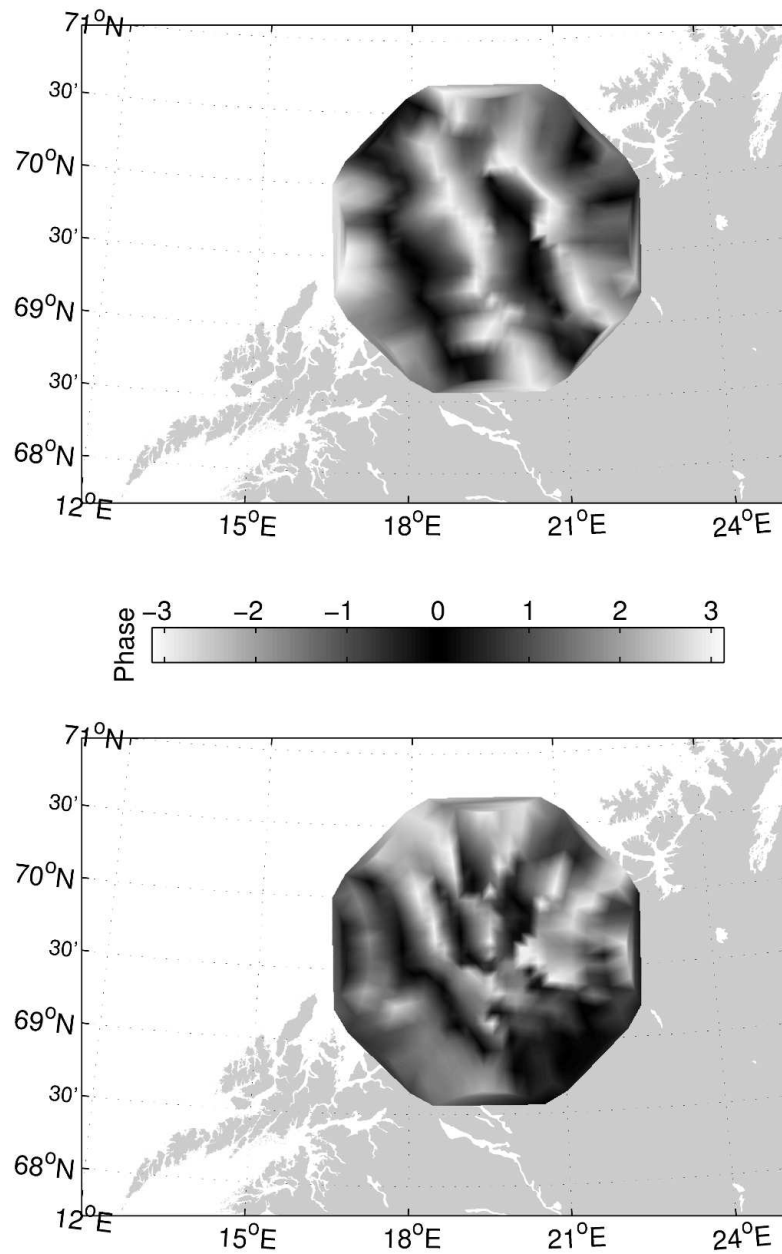
Figure 5.2: Phase maps of 17 January 2007 05:30 UT.
Top: 3.2 mHz, $m = 120$. **Bottom:** 5.7 mHz, $m = 320$.
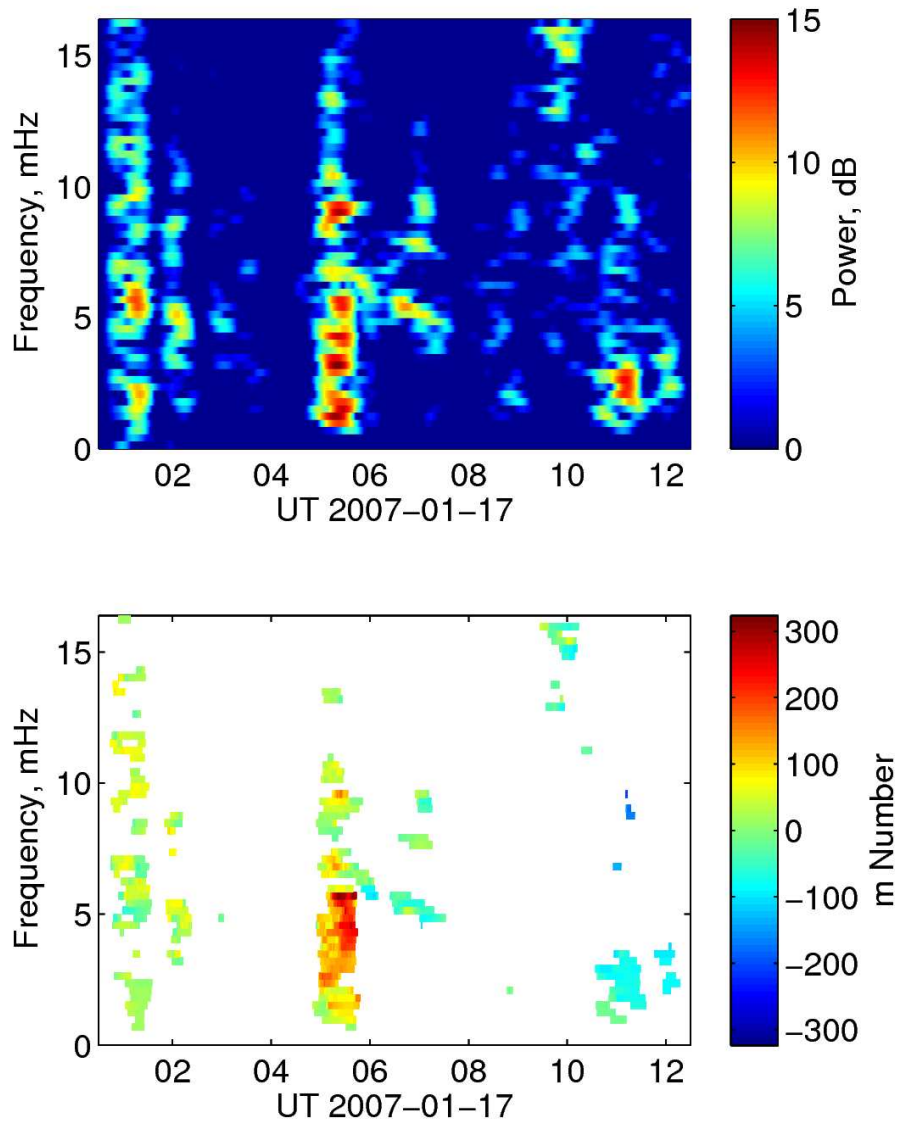
Figure 5.3: Spectrograms of the morning of 17 January 2007, showing the
high m event at 05:30 UT. **Top:** Cross-power. The 0 dB value is defined at
an arbitrary cut-off level. **Bottom:** Cross-phase.
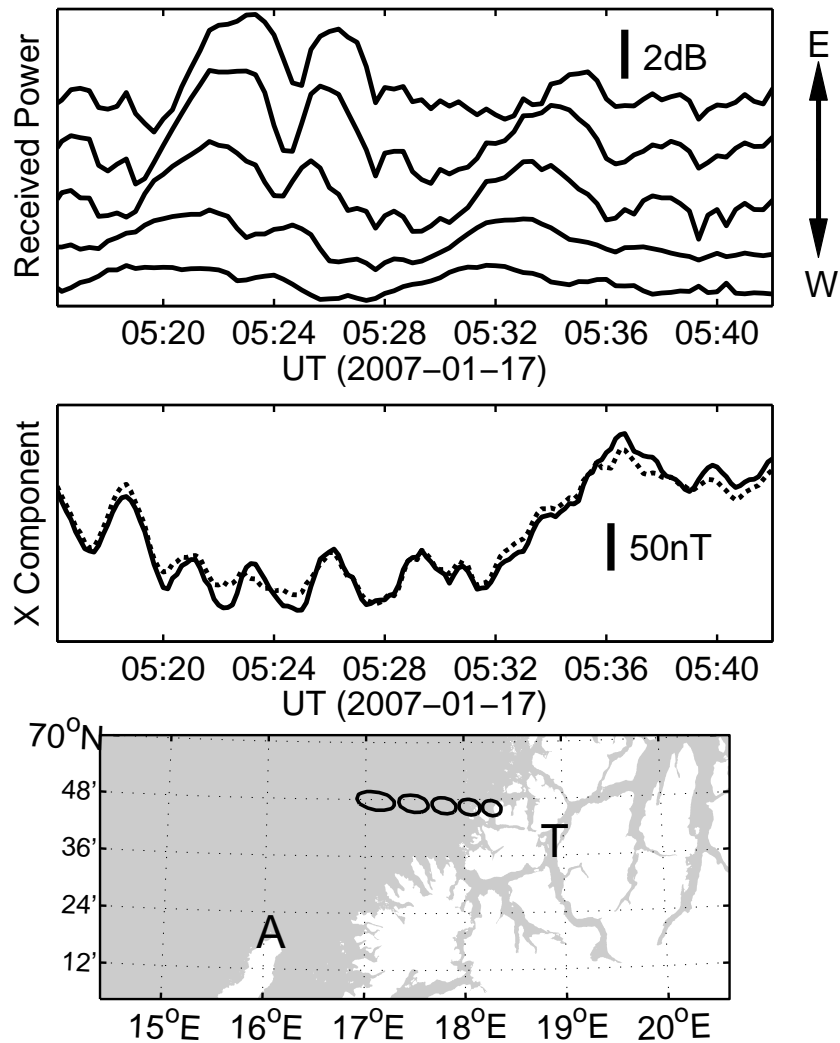
Figure 5.4: Unfiltered data from the event of 17 January 2007, 05:30 UT.
Top: ARIES received power from 5 individual neighbouring beams. **Center:**
Tromsø (solid), and Andenes (dotted) X component magnetometer data.
Bottom: Map showing the locations of the 5 ARIES beams (projected to
90 km altitude), and the **T**romsø and **A**ndenes magnetometers.

5.3   Theory of the generation mechanism

5.3.1   Particle-wave resonance

A charged particle drift-bouncing in the magnetosphere is able to resonate
with a toroidal MHD wave when the *resonance condition* is met:

$$\omega - m\omega_d = N\omega_b, \tag{5.1}$$

(Southwood et al., 1969), where m is the azimuthal wave-number, and ω is
the angular frequency of the wave; ω_d and ω_b are the drift and bounce angular
frequencies of the particle. N is the *resonance order*, an integer that may
be positive, negative, or zero. A graphical representation of the resonance
condition is given in figure 5.5. 5.5a, 5.5b, and 5.5c, show the trajectories of
an ion in resonance with the $N = 0$, 1, and 2 modes, respectively, in the rest
frame of the wave.

In a process known as Landau damping, drift-bouncing charged particles
with slightly less energy than required for resonance will take energy from the
wave, regardless of the direction of their motion around Earth. Conversely,
in inverse Landau damping, particles with slightly more energy than required
for resonance will transfer energy to the wave.

It is worth noting that in order for such resonances to occur, which
is a widely accepted phenomena, there must be energy exchange between
particles and waves close to resonance. The exact mechanism of energy
is transfer between the particles and wave is not universally agreed upon.
Southwood et al. (1969) suggested that the azimuthal electric field component

of the wave could accelerate charged particles. This has been disputed on
the grounds that, in the absence of strong collisions, an electric field in the
presence of a perpendicular magnetic field would only produce drift motion.

Another possible mechanism in the $N \neq 0$ case is second order Fermi ac-
celeration (Fermi, 1949). This process involves a magnetic field that increases
in strength each time a particle is bounces, effectively giving the particle a
'kick'. Alternatively, it can be thought of as a magnetic mirror that moves
toward/away from a bouncing charged particle, causing the particle's energy
to be increased/decreased. The magnetic field perturbation due to the ULF
waves under consideration would present such a moving mirror point, and
could exchange energy with near-resonant charged particles.
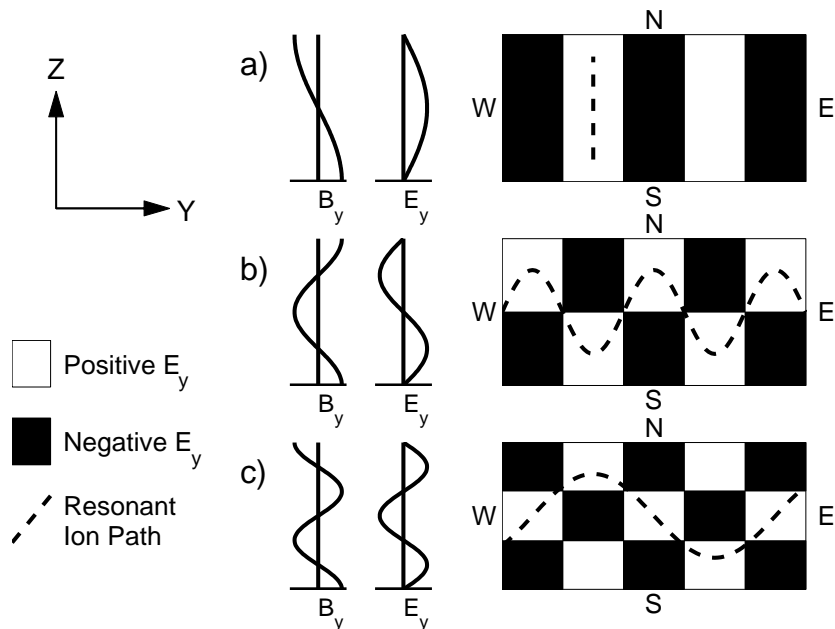
Figure 5.5: Illustration of the resonance condition (after Southwood and
Kivelson (1982)). **a)** N=0, **b)** N=1, **c)** N=2. The dashed lines represent the
ion motion in the rest frame of the wave.

The proton drift (Chisham , 1996) and bounce (Glassmeier et al., 1999) angular frequencies, in the Earth's rotating reference frame, are:

$$\omega_d = \frac{EL^2}{B_s R_E} - \frac{6WL(0.35 + 0.15\,\sin(\alpha))}{B_s R_E^2}, \tag{5.2}$$

$$\omega_b = \frac{\pi\sqrt{W}}{\sqrt{2m_p}LR_E(1.3 - 0.56\,\sin(\alpha))}, \tag{5.3}$$

where L is the L-shell of the proton and W is its energy in eV, B_S is the equatorial magnetic field strength at the surface of Earth, α is the equatorial pitch angle of the proton, E is the magnetospheric electric field, and m_p is the proton mass.

Resonance at the L value of the ARIES riometer, near geosynchronous orbit, is relevant. Here, following Baddeley et al. (2002), equations (5.2) and (5.3) reduce to:

$$\omega_d \approx C_1 + C_2 W, \tag{5.4}$$

$$\omega_b \approx \sqrt{C_3 W}. \tag{5.5}$$

where $C_1 = 7.7 \times 10^{-6}$, $C_2 = -1.44 \times 10^{-8}$, and $C_3 = 2.89 \times 10^{-7}$.

5.3.2 Combining Landau and inverse-Landau damping

Protons accelerated by Landau damping will form a bump on the tail of their energy distribution functions. When the driving wave ceases, the bump-on-tail energy becomes unstable to inverse Landau damping, and the generation of a secondary MHD wave can occur. Combining equations (5.1), (5.2), and (5.3), it is found that a secondary wave has one of two degrees of freedom determined by the energy of the bump-on-tail particles, i.e. the wave frequency and m number of a secondary wave are not fixed, but are dependent. For any particular frequency and m number of a driving wave, there will be a linear relationship between frequency and m number of all possible secondary waves.

Considering equation (5.1), for both a driving and secondary wave in resonance with a common ion energy, the general linear relation is obtained:

$$\omega_S = m_S\,\omega_d + \frac{N_S}{N_D}(\omega_D - m_D\,\omega_d), \qquad (5.6)$$

where the D and S subscripts refer to the driving and secondary waves respectively.

If the properties of the driving wave are known, the proton angular drift
frequency, ω_d, may be determined using equations (5.1), (5.2), and (5.3),
and substituted into equation (5.6) to reveal the possible parameters of a
secondary wave. Thus, at geosynchronous orbit:

$$
\begin{aligned}
\omega_S = {} & \left[\frac{N_D C_3}{2 m_D C_2} - \sqrt{\left(\frac{N_D C_3}{2 m_D C_2} \right)^2 - \frac{C_3}{C_2} \left(C_1 - \frac{\omega_D}{m_D} \right)} \, \right] \\
& \times \left(\frac{m_S}{m_D} N_D - N_S \right) + \frac{m_S}{m_D} \omega_D.
\end{aligned} \tag{5.7}
$$

Based on the current hypothesis, that many of the observed high m
number waves are a product of resonances, driven by cavity-like wave modes,
the case of a large scale, i.e. small m number, driving wave is considered. As
$m_D \to 0$, equation (5.7) becomes:

$$
\omega_S(m_D \to 0) = m_S \left[C_1 + \frac{C_2}{C_3} \left(\frac{\omega_D}{N_D} \right)^2 \right] + N_S \frac{\omega_D}{N_D}. \tag{5.8}
$$

5.3.3 Resonance orders

The resonance orders N_D and N_S are integers, including negative values
and zero. Since ω and ω_b are by definition positive, some values of N are not
always possible, depending on the azimuthal direction of the wave (positive or
negative m) and the azimuthal drift direction of the charged particle (positive
or negative ω_d). Generally, smaller values of N produce more strongly
coupled resonances, with $N = 0$ being the Cerenkov resonance. N must
be non-zero and positive for eastward propagating MHD waves in resonance

with protons. This is also the case with cavity mode-like waves, where
the low azimuthal wave numbers would require unrealistically high particle
energies for $N = 0$. However, westward travelling waves may resonate with
$N_S = .., -2, -1, 0, 1, 2, ..$, and would therefore present a more complicated
picture.

It can be seen from figure 5.5 that the shear Alfvén harmonic, n, is related
to the resonance order by $n = N + 1$. Since $N = 1$ is expected to be the
strongest resonance for cavity mode waves, $n = 2$ will be used in a model
solution (section 5.3.5).

5.3.4 Modulation of precipitation

The capability of magnetospheric ULF waves to modulate electron precip-
itation has been well established via observation (e.g. Spanswick et al.
(2005)). Coroniti and Kennel (1970) (see also Haugstad (1975)) suggested
that the magnetic pulsation modulates the growth-rate of whistler-mode wave
turbulence. Since these waves drive pitch-angle diffusion via Doppler-shifter
cyclotron resonance the electron precipitation is modulated. Nosé et al.
(1998) offered an alternative mechanism whereby electrons are accelerated
due to the parallel electric field of a kinetic Alfvén wave. For this study
the actual mechanism that operates is unimportant, it is enough that the
modulation of electron precipitation is occurring.

5.3.5 Magnetospheric cavity modes

Later it will be apparent that the cavity-mode waves are quantized, with
only a small set of particular frequencies being observed. This is a useful
feature, which helps to identify them as a source of high m waves. While it
might be obvious that these frequencies relate to resonances within the mag-
netospheric cavity, this section aims to examine in more detail the structure
and characteristics of the cavity resonances, and their role in the generation
of high m waves.

To describe the magnetospheric cavity modes, and coupled field line
resonances, the method of Cheng et al. (1998) is followed, by solving the
linearised ideal MHD wave equation in simple Cartesian coordinates. X
represents radial distance, and Y azimuthal distance, with positive Y toward
dusk. The Z direction follows the magnetic field, from the South to the
North pole.

$$\frac{d^2\mathbf{E_1}}{dt^2} = \frac{1}{\mu_0 \rho_0} \left[(\nabla \times \nabla \times \mathbf{E_1}) \times \mathbf{B_0} \times \mathbf{B_0} + \right.$$
$$\left. (\nabla \times \mathbf{B_0}) \times (\nabla \times \mathbf{E_1}) \times \mathbf{B_0} \right], \qquad (5.9)$$

where $\mathbf{B_0}$ is the ambient magnetic field, ρ_0 the ambient plasma density, and
$\mathbf{E_1}$ the electric field perturbation.

In ideal MHD there is no electric field component along the magnetic field. $\mathbf{E_1}$ may therefore be described by:

$$\mathbf{E_1} = (E_{1X}(X), E_{1Y}(X), 0) \cdot \exp\left[i\left(k_Y Y + k_Z Z - \omega t\right)\right], \qquad (5.10)$$

where k_Y and k_Z are the wave numbers in the Y and Z directions, respectively.

In order to explore standing wave modes, equation (5.9) is decomposed into two steady state differential equations. The first to be solved for E_{1y}, the second giving E_{1x}:

$$\frac{d^2 E_{1Y}}{dX^2} + \left\{ \frac{2k_Y^2 \omega^2 \left(\frac{dv_A}{dX}\right)}{\left(\frac{\omega^2}{v_A^2} - k_Z^2\right)\left(\frac{\omega^2}{v_A^2} - k_Z^2 - k_Y^2\right) v_A^3} + \frac{1}{B_0}\frac{dB_0}{dX} \right\} \frac{dE_{1Y}}{dX}$$
$$+ \left(\frac{\omega^2}{v_A^2} - k_Z^2 - k_Y^2\right) E_{1Y} = 0, \qquad (5.11)$$

$$E_{1X} = \frac{ik_Y \frac{dE_{1Y}}{dX}}{\left(\frac{\omega^2}{v_A^2} - k_Z^2 - k_Y^2\right)}, \qquad (5.12)$$

where $v_A = B_0 / \left(R_E \sqrt{\mu_0 \rho_0}\right)$ is the Alfvén speed in Earth radii per second. In Cartesian coordinates, k_Y is equivalent to the azimuthal m number. All distances are in Earth radii (R_E), wave-numbers are in radians R_E^{-1}, and speeds are $R_E \text{s}^{-1}$.

In order to avoid a problematic singularity in (5.11) and (5.12) at $\omega^2/v_A^2 - k_Z^2 - k_Y^2 = 0$, the angular wave frequency, ω, is given an imaginary component. The negative damping factor $\gamma = \Im(\omega)/\Re(\omega)$ represents an irreversible loss of energy to the coupled field line resonances. The effect of this damping is to broaden a field line resonance without altering its location. The value of k_Z is taken to be $n \cdot \pi/5$, where $n = 1, 2, 3, \cdots$ and 5 is the normalized length of the field lines, following Cheng et al. (1998).

After solving equations (5.11), and (5.12), the magnetic field perturbation is found using the Maxwell-Faraday equation:

$$\nabla \times \mathbf{E_1} = -\frac{\partial \mathbf{B_1}}{\partial t}. \qquad (5.13)$$

Thus, the magnetic field perturbation in the X direction is proportional to the electric field perturbation in the Y direction, and vice versa.

A numerical solution is presented in figure 5.6, for magnetic field corresponding to the equatorial plane of a dipole $(B_0 \propto 1/X^3)$, with the adjustable Alfvén speed profile utilized by Cheng et al. (1998), shown in figure 5.7. The parameter values used in this solution are $P = 4.7$, $Q = 4.7$, $R = 7.37$, $v_{A0} = 0.0387$, with $\omega = 16 \times 10^{-3} \cdot 2\pi$, $\gamma = -0.0022$, $k_Z = 2 \cdot \pi/5$, and $k_Y = 0.5$. The Alfvén speed at the plasmapause, v_{A0}, and the parameter R, have been chosen such that an $8\,\text{mHz}$ field line resonance will occur at $6.18 R_E$, in accordance with observations of phase reversal in magnetometer data, (Menk et al., 2001).
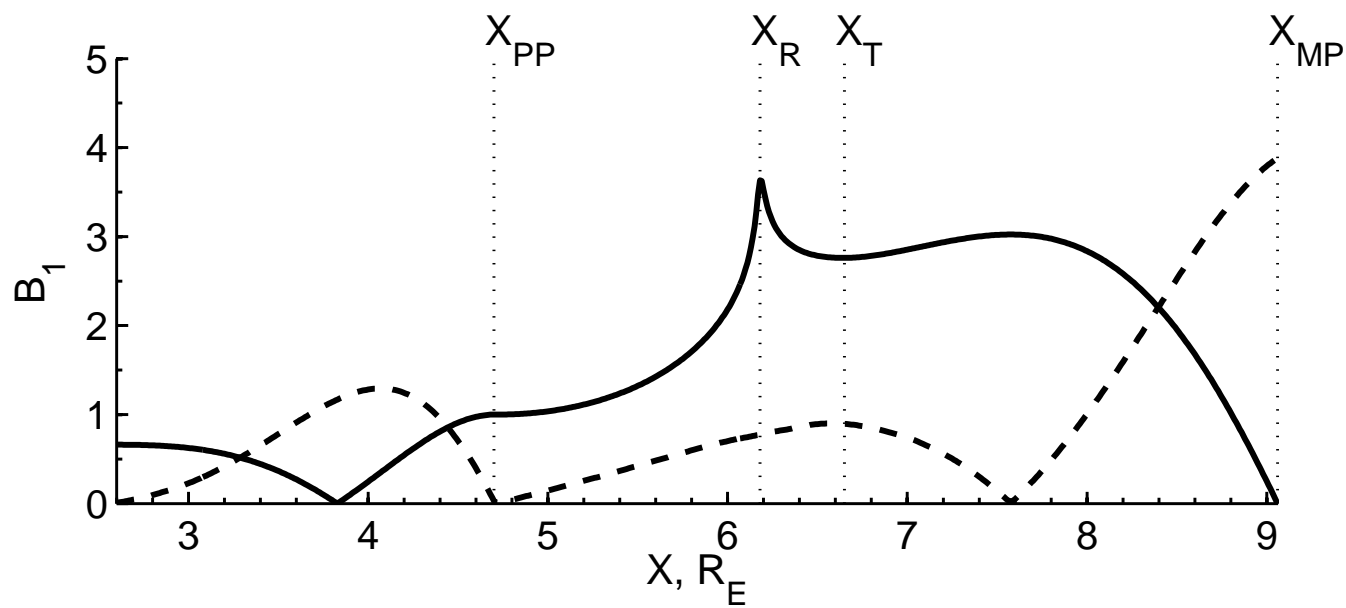
Figure 5.6: A time independent solution of the ideal MHD wave equation, for a frequency of $16\,\mathrm{mHz}$, with $n = 2$. Magnetic field perturbations are shown in the X (solid), and Z (dashed) directions.

Without azimuthal boundaries the choice of k_Y seems arbitrary, and in reality would be determined by the propagation of a solar wind pressure front along the magnetopause. Here a value of 0.5 radians R_E^{-1} is chosen, equivalent to an m number of 3.5 at $X = 7R_E$, which is not unreasonable. At the magnetopause the boundary conditions require that the electric field, and therefore the magnetic field perturbations in the X and Y directions, are zero. However, B_{1Z}, representing equatorially symmetric compressions and rarefactions of the magnetic field, is not zero. This is the means of energy transfer from solar wind pressure variations to the cavity mode waves.

In the WKB approximation, $(\omega^2/v_A^2 - k_Z^2 - k_Y^2)$ can be thought of as the variable wave-number $k_X(X)$. A turning point, X_T, is found in B_{1X}, where $k_X(X) = 0$. In the present solution $X_T = 6.65$. Earthward of this point the cavity mode decays, before resonance with field line oscillations occur at X_R. Across the field line resonance, which is centred on $k_Z = \omega/v_A$, there is a phase reversal in the toroidal component, B_{1Y}.

Beyond X_R the cavity mode continues to decay, until a second turning point is met. For an Alfvén speed profile proportional to $1/X$, the second turning point is located at $X_T/\sqrt{2}$, where $k_X(X) = i\omega/v_A$. In the absence of a plasmapause all three components have local minimum at the second turning point, where B_{1Y} and B_{1Z} are zero, but B_{1X} is non-zero and finite. Here, the magnetospheric cavity mode can efficiently couple to that of the plasmaspheric cavity, at the plasmapause, X_{PP}.

The solution within the plasmaspheric cavity has an anti-node in B_{1X}, and nodes in B_{1Y} and B_{1Z}, at the plasmapause, where, neglecting damping, $k_X(X)$ is once again real due to the lower Alfvén speed.

The distance from, for example, the turning point X_T, to the closest possible position of the magnetopause, X_{MP}, may be estimated using the phase integral equation:

$$\phi_n = \int_{X_T}^{X_{MP}} k_X(X)\, dX - (l - 1/4)\pi = 0 \qquad (5.14)$$

where l is an integer.

When the azimuthal wave-number is not exactly zero, time independent solutions are available only for a plasmapause of zero thickness, indicating that a thin plasmapause is important for standing wave longevity in the combined plasmaspheric and magnetospheric cavity. Satellite observations (e.g. Chappell et al. (1970)) have shown that, during high ap index, the plasmapause is characterized by a fall in ion density of ~ 3 orders of magnitude in as little as $0.2R_E$. At low ap index the same ion density change typically occurs over a radial distance exceeding $1R_E$. Thus, it may be expected that events are more likely at times of high ap index.

The plasma density, and the azimuthal wave-number, k_Y, combine to determine a location of the second turning point in the magnetosphere that matches the location of the plasmapause.

The magnetospheric plasma density, azimuthal wave-number, and plasma-pause location have unique relationships with activity and local time. It is therefore expected that there will be a geomagnetic/solar activity dependence on the MLT of high m number observations. However, in order to establish relationships between such variables it would be necessary to abandon the Cartesian model, and fixed wave-numbers, in favour of a more realistic geometry, which is beyond the scope of this thesis.
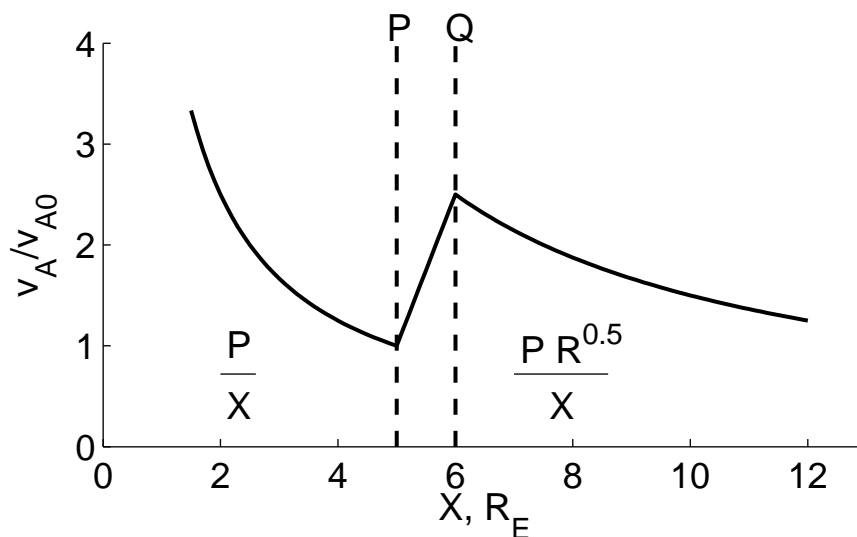
Figure 5.7: The adjustable Alfvén speed profile. Shown with $R = 9$, $P = 5$, and $Q = 6$. P and Q define the plasmapause, while v_{A0} is the Alfvén speed at P.

In summary, the simple box model provides estimates of the L-shell of phase-reversal for each cavity mode harmonic (utilized in section 5.4.2), predicts enhanced occurrence rates for a thin plasmapause, indicated by a high ap index, and predicts that there is likely to be an activity dependence on the MLT of events (explored in section 5.4.3).
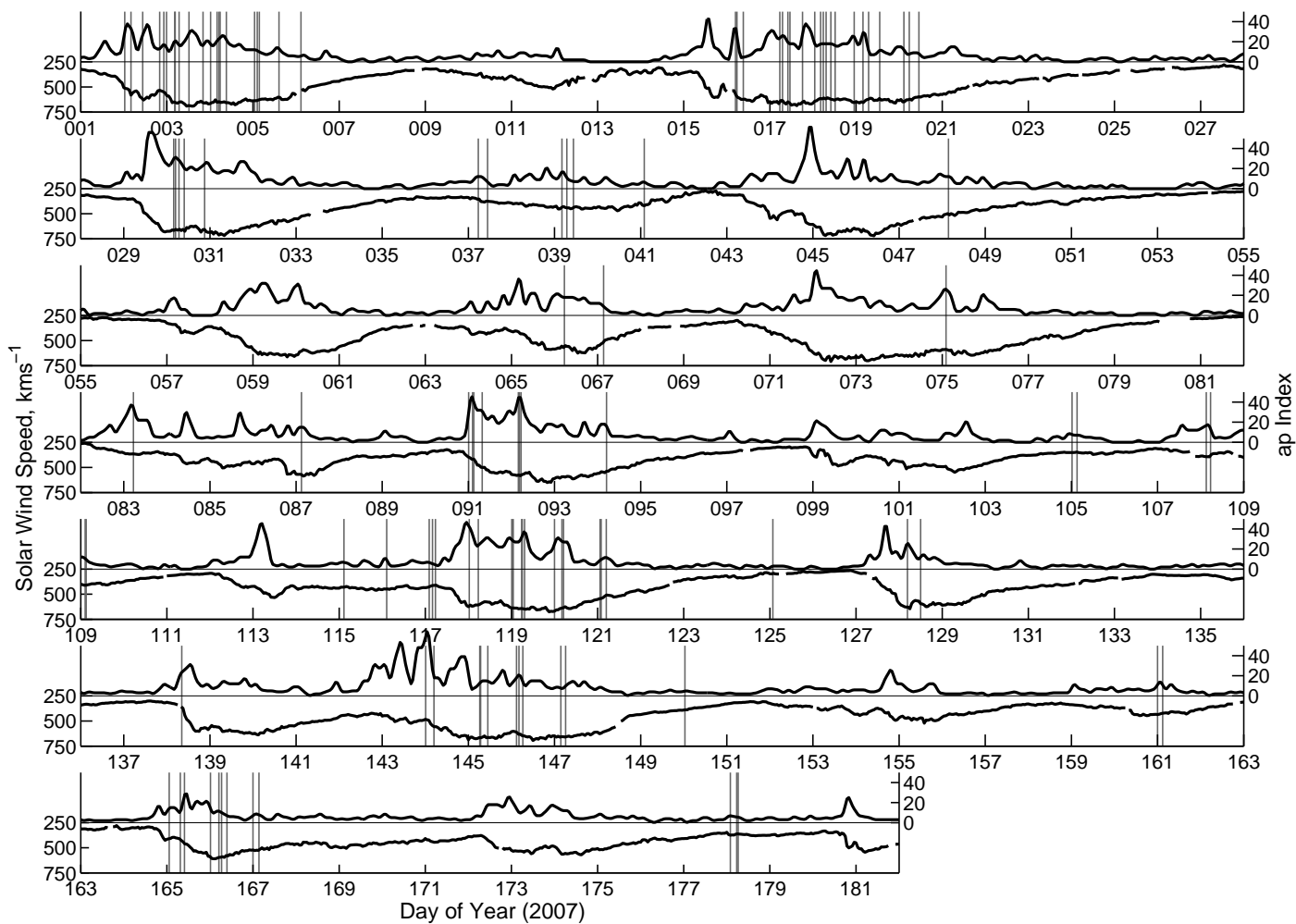
Figure 5.8: Occurrences of high azimuthal wave number ($|m| \geq 60$) events in ARIES, during the first six months of 2007.

5.4   Analysis of ARIES results

5.4.1   Dispersion relation of high m number waves

The dispersion relations of high m number waves observed by ARIES between
7.5 and 14 MLT, (figure 5.9), have distinct features consistent with secondary
waves driven by large scale MHD waves through Landau followed by inverse-
Landau damping of the magnetospheric proton population, as described in
section 5.3.2. All have ionospheric velocities of less than $1\,\mathrm{kms^{-1}}$.

The frequency values of driving waves used in the calculation (equation
5.8) of the fitted lines are $f_D/N_D = 0.8, 8, 11.5, 16, 23, 30.5, 38.5\,\mathrm{mHz}$. It is
not possible to differentiate between resonance orders, N_D; since it is the
value of f_D/N_D that determines the energy of the resonant protons, and the
dispersion relation of the secondary waves. The same is not generally true
of N_S, for which there are events of $N_S = 1$ and $N_S = 2$. Consequently,
events associated with $f_D/N_D = 8\,\mathrm{mHz}$ and $11.5\,\mathrm{mHz}$, for example, could be
$16\,\mathrm{mHz}$ and $23\,\mathrm{mHz}$ cavity modes, respectively, with $N_D = 2$.

Lower frequencies, f_D, and higher resonance orders, N_D and N_S, are
capable of producing higher m number secondary waves. For an $f_D = 16\,\mathrm{mHz}$
driving wave, the $N_D\,1\,N_S\,1$ case may generate up to $m \sim 200$ waves, whereas
the $N_D\,2\,N_S\,1$, and $N_D\,1\,N_S\,2$ cases are capable of producing waves of up to
$m \sim 400$. The highest m number observed (380), is attributed to $N_D\,1\,N_S\,2$.
An m number of 380 corresponds to an azimuthal wavelength (λ_{Az}) of $697\,\mathrm{km}$
at geostationary orbit, and $37.4\,\mathrm{km}$ in the ionosphere above ARIES.

Given the invariance of $v_\perp^2/B$ over the bounce period of a charged particle in a dipole field, it can be shown that the ratio of the azimuthal wavelength to the Larmor radius (λ_{Az}/ρ) is smallest in the equatorial plane. Drift bounce resonance, with $N \neq 0$, strongly favours particles of small equatorial pitch angle (Southwood and Kivelson, 1982; Baddeley et al., 2002). Assuming a pitch angle of $10°$, for a resonant proton in the $m = 380$ event, provides a ratio of $\lambda_{Az}/\rho \approx 15$, in the equatorial plane.

Three data points below $1\,\text{mHz}$ do not appear to match the linear relations for cavity mode frequencies. It could be that the same (Landau followed by inverse Landau damping) mechanism is acting on a lower frequency group of magnetospheric waves, for example, the slow magneto-sonic (SMS) oscillations described by Leonovich et al. (2006). The SMS waves resonate with fundamental frequencies between 0.1 and $1\,\text{mHz}$, and have amplitudes that fall rapidly upon approaching the ionosphere. This implies that the ionosphere cannot absorb a significant amount of the wave energy, and led Leonovich et al. (2006) to conclude: "SMS wave damping in the magnetosphere must be caused by other mechanisms, probably by their resonant interaction with the background plasma particles." Figure 5.9 includes a linear secondary wave function calculated for a $0.8\,\text{mHz}$ large scale driving wave. However, it should be noted that the fit of few data points is improved following this inclusion.

Eastward high m wave events are observed in reduced numbers as early as 2.5 MLT, but those occurring before 7.5 MLT do not to fit the dispersion relation functions of the day-side events, and are excluded from figure 5.9. This is to be expected, due to the MLT variation in the size of the magnetospheric cavity away from the day-side, which alters the frequencies of cavity modes, and subsequently, the dispersion relation functions. Additionally, pulsations in the flanks of the magnetosphere driven by the Kelvin-Helmholtz instability are predicted to have similar frequencies (5–10 mHz), with varying m numbers (typically $m \sim 15$), (Claudepierre, 2008). If such waves are driving sources in the generation of high m waves, either by the mechanism under consideration, or otherwise (e.g. Allan et al. (1997)), evidence in the dispersion relations of any secondary waves will be difficult to find. Analysis is restricted to eastward waves observed around local noon, a stagnation point for the solar wind, where velocity shear is minimized, and clear patterns in the dispersion relations are found. It should be noted that, although the waves have velocities in the eastward direction, the events do not propagate. The wave is generated and decays within a fixed MLT, evidenced by observations on successive days.
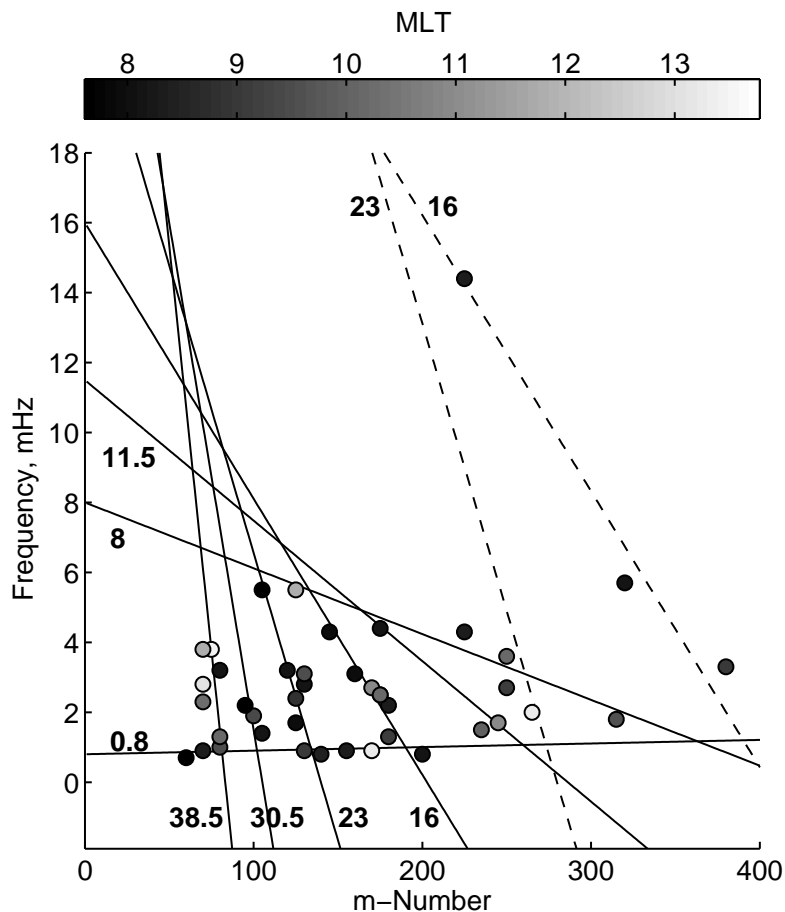
Figure 5.9: The dispersion relation of wave structures found in ARIES with
$m \geq +60$, between 7.5 and 14 MLT. Solid lines are $N_S = 1$ resonance, dashed
are $N_S = 2$. The adjoined numbers are the values of f_D/N_D, in mHz, used
in the equation of each line.

Cavity Mode Frequency/N_D (mHz)	Resonant H$^+$ Energy (keV)
0.8	0.087
8	8.7
11.5	18
16	35
23	72
30.5	127
38.5	202

5.4.2 Phase reversal at field line resonance

An event on 18 May 2007, figure 5.10, displays an apparent phase reversal between the northern and southern halves of the ARIES field of view. This is especially clear in the east, where an imagined straight line following a northern crest would continue along a southern trough, and vice versa.

A phase reversal is expected at the L value of a field line resonance, theoretically (see section 5.3.5), and as a well known feature of magnetometer FLR observations. Physically, it is interpreted as a reversal in the bouncing phase of resonant ions, spread over a finite radial distance due to damping and a finite electric field perturbation.

The frequency and azimuthal wave number of this event suggest a cavity mode driving wave of $f_D/N_D = 11.5\,\mathrm{mHz}$, for which the box model calculation, calibrated by magnetometer FLR observation, predicts a phase reversal centred at $X = 6.44R_E$. Using the Tsyganenko T01 model (Tsyganenko, 2002), with suitable inputs for the time of the event, agreement is found in tracing the magnetic field from the ionosphere directly above ARIES to an equatorial distance of $6.52R_E$.

5.4.3 Location of high m number waves

It was discussed in section 5.3.5 that cavity mode waves depend on various magnetospheric parameters. Of particular importance are likely to be the Alfvén speed profile, and the location and thickness of the plasmapause. In figure 5.8, a correlation is found between times of enhanced ap index and solar wind speed, and the observations of high m number events. Although
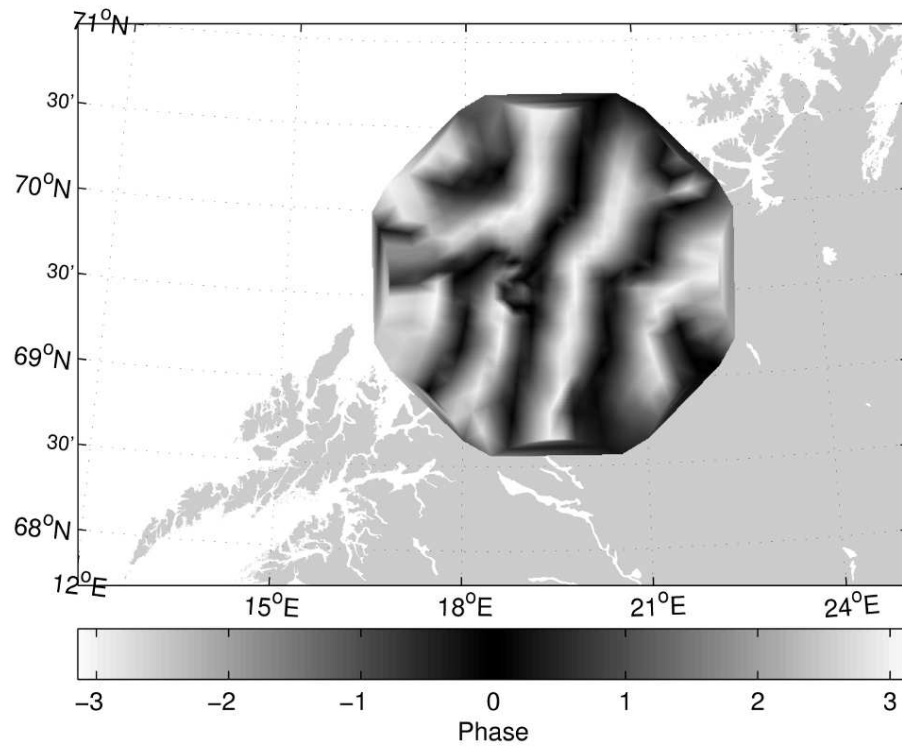
Figure 5.10: The phase map of an event on 18 May 2007 08:20 UT, associated with the resonant cavity mode of frequency $f_D/N_D = 11.5\,\mathrm{mHz}$.

this could be due to an increase in particle flux following substorm activity, a heightened ap index is indicative of a thin plasmapause, conducive to the existence of cavity modes. Furthermore, the events occur exclusively with $ap \geq 5$, while between 1 January 2007 and 30 June 2007, the period from which the data set is taken, $48.5\,\%$ of ap values are below 5. This could be suggestive of a limit in plasmapause thickness, above which the mechanism can not operate.

Following Chappell et al. (1970), a basic empirical estimate for the plasma-pause location may be obtained from the maximum ap index of the preceding 12 hours:

$$X_{pp} = 3.2 + 2.8 \exp\left(-kp/3\right) \tag{5.15}$$

where kp is the geomagnetic activity index directly related to ap (see section 2.6.2). In figure 5.11, the distribution of the events in MLT is plotted against this estimated plasmapause location, for which a correlation is found.
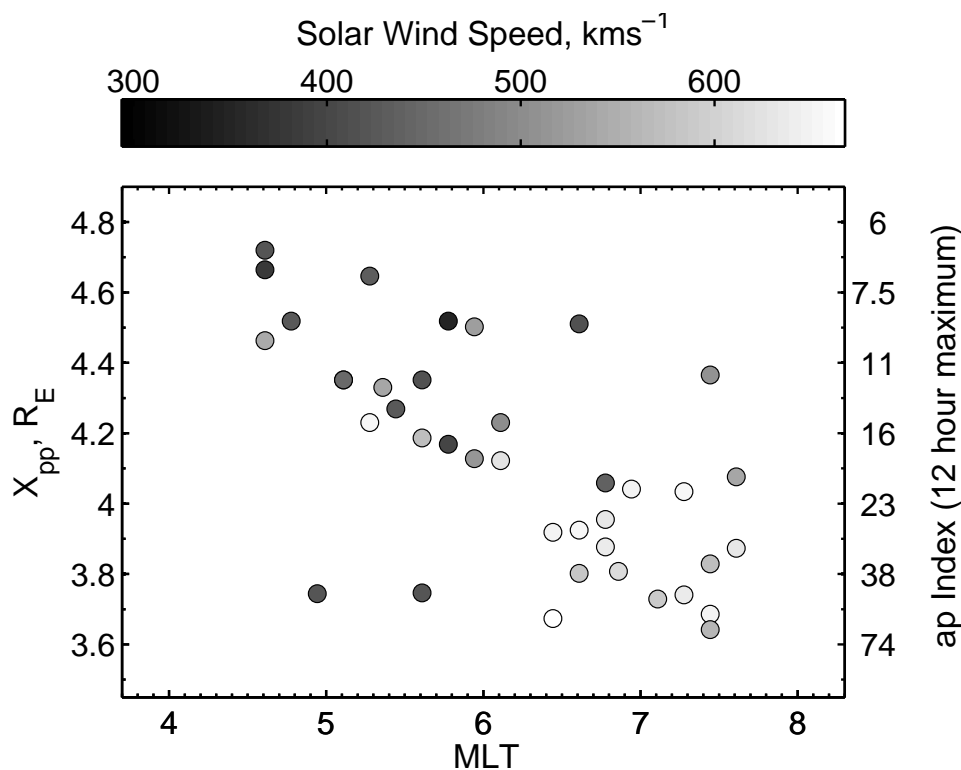
Figure 5.11: The effect of ap index, and the corresponding estimated plasmapause position, on the local time of high m number events. The correlation coefficient is -0.69.

It is probable that the coherence of day-side cavity mode waves over a range of MLT is key in the formation of a significant bump on the tail of the proton energy distribution. High m number CNA pulsations with approximately identical properties are often observed on consecutive days at the same MLT, indicating a long lived nature. In conjunction with the typically small (~ 1 hour) MLT range, this suggests that the local time distribution may be determined at a stage after the Landau damping of cavity modes, perhaps at the location of a threshold in the number of electrons available for modulated precipitation. It could be further speculated that beyond the location of this threshold, the loss rate of bump-on-tail energy from the westward drifting proton distribution to the modulated electron precipitation may determine the local time extent of the pulsations.

In figure 5.12A, the normalized power of detected waves is given as a function of MLT, and in figure 5.12B as a function of X, the radial distance in R_E, traced for each event along the magnetic field, using the Tsyganenko magnetic field model, (Tsyganenko, 2002). It is not possible to separate local time variations in power from those of radial distance, however, a peak in the wave power is found where the riometer location is traced to 7 R_E, at 8 MLT and 12.5 MLT.
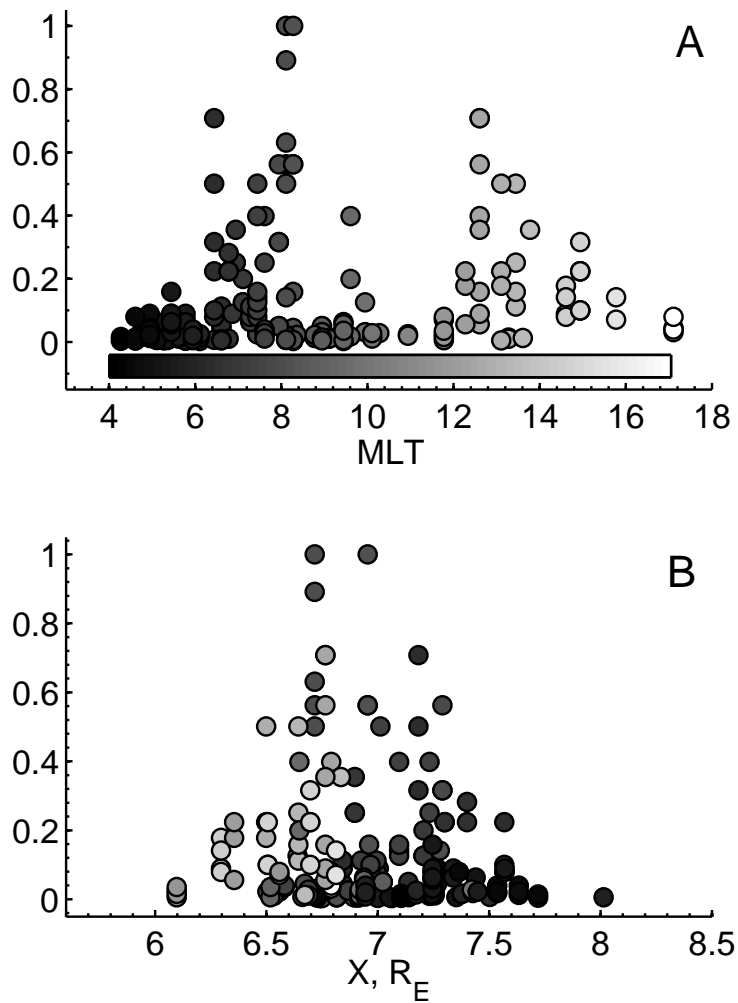
Figure 5.12: **A:** Normalized wave power versus MLT. **B:** Normalized wave
power as a function of radial distance. Shade represents MLT.

5.5   CAMMICE (MICS) Results

The proposed mechanism makes a testable prediction of the proton energy distribution in the day-side magnetosphere. Positive gradient regions should commonly exist at discrete energy values corresponding to Landau damping of the magnetospheric cavity modes. These energy values are given in the table attached to figure 5.9.

Previously, Baddeley et al. (2002) conducted a survey of bumps-on-the-tails of proton energy distributions near geosynchronous orbit, using Polar CAMMICE data from 1996 through 2001. Positive gradient regions were found to exist predominantly between 05 and 14 MLT, with occurrence rates peaking above 40%. The explanation of this MLT distribution is quite straightforward: protons drift westward from the night-side injection region; on reaching the day-side magnetopause, those near resonance are accelerated by Landau damping of cavity mode waves. They continue to drift westward into the morning sector, until the free energy in the distribution is lost to the inverse Landau damping of secondary MHD waves.

Figure 5.13 shows the occurrence rate of detected enhancements in the proton distribution function as a function of energy. The data spans the years 1996 – 2000, and is restricted to times when the Polar spacecraft is located within L values of 5–9 and MLT of 05–14.

The logarithm of the mean proton distribution function in the tail is approximately linear in $\sqrt{E}$, with a gradient

$$\frac{d(\log_{10} F)}{d(\sqrt{E})} \approx -0.1 \tag{5.16}$$
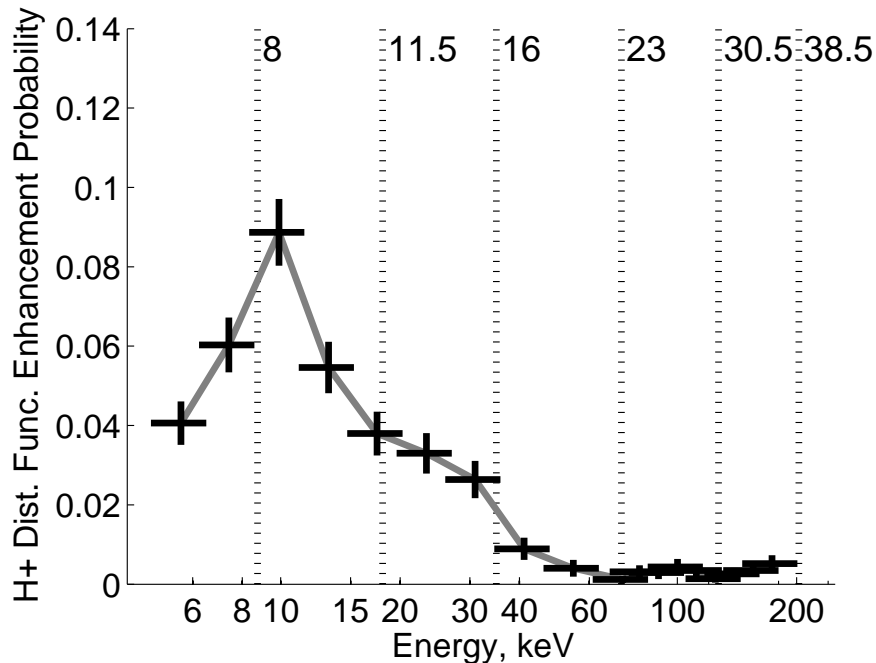
Figure 5.13: The occurrence rate of detected enhancements in the proton distribution function. The data set is restricted to the times when Polar is within $5 < L < 9$ and $5 < MLT < 14$. Dotted lines indicate the energies of resonant protons for each cavity mode frequency (labels are f_D/N_D in mHz). Horizontal bars represent energy bin widths, vertical bars indicate the standard error in the mean.

For the present purposes, an enhancement is said to be detected in a channel if this gradient is greater than -0.05 between the channel and it's lower energy neighbour, and less than -0.15 between the channel and it's higher energy neighbour. These values are somewhat arbitrary; taking values closer to -0.1 would provide more detected enhancements, together with more false detections due to noise in the data. However, this increased sensitivity should not result in a bias towards any particular channels.
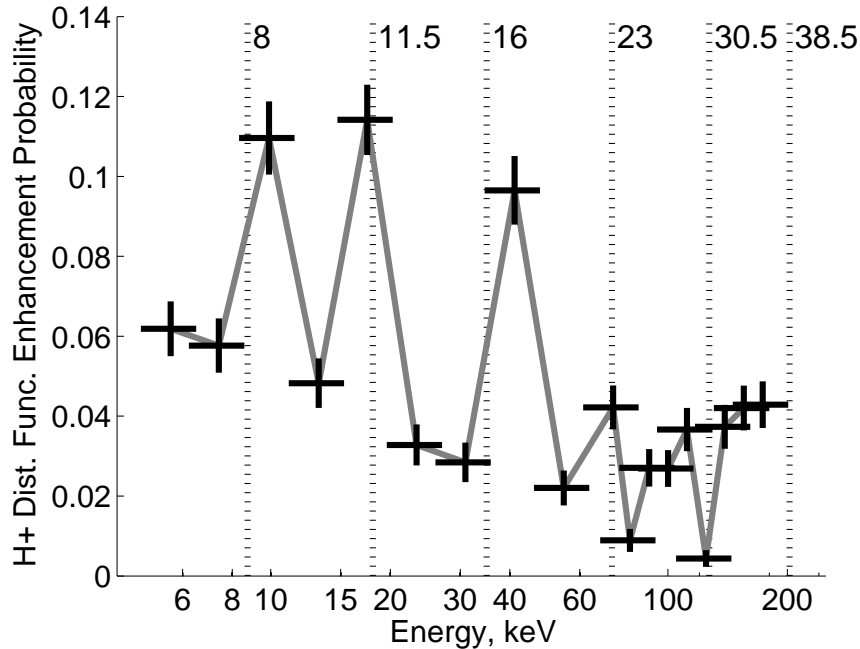
Figure 5.14: As figure 5.13, with the inclusion of single energy channel flagged data.

In figure 5.13, the same detected enhancements are shown, with the inclusion of singular unexplained bad data points. It is suspected that real enhancements occupying single energy channels are being flagged as bad data during the processing of CAMMICE data. Bad data values, for example following a loss of synchronization, should be independent of the ESA stepping pattern, and therefore independent of energy channel. However, cases in which single channels are flagged are found to strongly favour those channels closest to the expected energies of the $f_D/N_D = 11.5$, 16 and 23 mHz resonances. At lower energies, corresponding to $f_D/N_D = 8$ mHz, enhancements occupy more than one of the logarithmically spaced energy channels, and are more properly detected as bumps in the energy distribution function,

seemingly unaffected by the CAMMICE quality control processing. For this
reason, flagged data is included as positive detections of enhancements if the
values in neighbouring energy channels are valid. At energies above $70\,\mathrm{keV}$,
the widths of the energy channels are significantly greater than their spacing,
and the detection of enhancements in the distribution becomes problematic.

5.6   Energy Considerations

If Landau damping of magnetospheric cavity-mode waves is the source of high
m number waves, the energy available in the cavity modes must be greater
than that observed in the high m waves. In the proposed mechanism the
cavity modes are excited by pressure pulses on the day-side magnetosphere.
A first order approximation for the energy imparted by the solar wind in
compressing the magnetosphere is:

$$\mathrm{E} = \mathrm{P_{dyn}} \cdot \sigma_{\mathrm{M}} \cdot \Delta \mathrm{X_{pp}}, \qquad\qquad (5.17)$$

where $\mathrm{P_{dyn}}$ is the solar wind dynamic pressure, σ_{M} is the effective cross
sectional area of the magnetosphere, and $\Delta \mathrm{X_{pp}}$ is the change in the sub-solar
plasma pause distance. Inserting some reasonable values: $\mathrm{P_{dyn}} = 2\,\mathrm{nPa}$,
$\sigma_{\mathrm{M}} = 60\sigma_{\mathrm{Earth}}$, and $\Delta \mathrm{X_{pp}} = 1R_E$, the energy transferred from the solar wind
is found to be $10^{14}\,\mathrm{J}$.

Utilizing the particle instruments aboard the Polar spacecraft, Baddeley et al. (2004) calculated the magnitude of free energy density within the ion distribution functions associated with high m events. Estimates of total free energy were then obtained by spatial integration: typically $\sim 10^9$ J, and up to 3.4×10^{11} J. With an entirely different approach, Allan and Poulter (1984) estimated the ionospheric energy dissipation of two particle driven waves using the STARE radar, and reported values of a similar magnitude, $\sim 10^{10}$ J, and $\sim 10^{11}$ J. The process is not expected to be an efficient one, so an efficiency of $\sim 0.1\%$, implied by these estimates of input and output energy, does not seem wholly unreasonable.

More thorough attempts have been made to estimate the input of solar wind energy, and its partitioning in the magnetosphere – ionosphere system (see e.g. Koskinen and Tanskanen (2002); Turner et al. (2009)). Since there are no known means to directly measure the input energy, this is not a trivial problem. Turner et al. (2009) utilize the Akasofu epsilon parameter (Akasofu, 1981) in quantifying the median energy input during CIR and CME storm events, as 6.38×10^{16} J, and 8.07×10^{16} J, respectively.

Given the early formulation of the epsilon parameter, before it was understood that the ionosphere exceeds the ring current as a major sink of storm and substorm energy, the estimates of total energy input into the magnetosphere it provides are remarkable when scaled by a factor of $1.5 - 2$ (Koskinen and Tanskanen, 2002). A considerable proportion of this energy (27% during CIR, and 37.3% during CME events,) remains unaccounted

for after Turner et al. (2009) sum the corresponding output energy through the ring current, Joule heating, and auroral precipitation sinks. It is clear from the energies associated with high m waves, that these are a very minor energy sink, and would not greatly affect the partitioning of energy within the magnetosphere.

5.7 Discussion and Conclusion

The primary result of this study is in the dispersion relations of day-side, high m number, eastward propagating waves (figure 5.9). These show clear structure, matching well with functions expected from cavity mode (i.e. large scale) sources, with frequencies of 8, 11.5, 16, 23, 30.5 and 38.5 mHz. Several of these frequencies appear in previous studies. Yumoto et al. (1994) reported global magnetometer observations of cavity-like oscillations at 15.5, 25, and 31 mHz, following interplanetary impulses. Sibeck et al. (1989) observed ringing at a period of 2 minutes (8.3 mHz) in the outer magnetospheric magnetic field, following a step function increase in solar wind pressure. Furthermore, quasi-monochromatic 2 minute oscillations in the magnetic field, ion number density, temperature and velocity in the dawn-side magnetosphere have been encountered by the Equator-S spacecraft (Rae et al., 2007).

Spectral analysis of ringing within a model magnetosphere following a solar wind pressure pulse, (Lee et al., 2004), provided similar frequencies: 8, 16-23, 30, 40 mHz, and so on. Claudepierre (2009) conducted global solar wind–magnetosphere 3D MHD simulations and reported a fundamental cavity mode frequency close to 10 mHz. Whereas, Fujita and Itonaga. (2003) calculate an eigenmode frequency of 14 mHz at dawn, and 18 mHz at dusk, for resonance within the plasmaspheric cavity. It becomes increasingly clear that the cavity mode frequencies inferred herein are commonplace in the day-side magnetosphere, with the probable exception of 11.5 mHz, which is taken to be the 23 mHz cavity mode, resonating with $N_D = 2$.

The well known global modes of 1.3, 1.9, 2.6, and 3.4 mHz (Samson et
al., 1991; Samson and Rankin, 1994), are notably absent. There is growing
opinion that such frequencies are too small to be day-side magnetospheric
cavity modes, and may be forced oscillations at frequencies present in the
solar wind (Leonovich and Mazur (2001); Eriksson et al. (2006), and refer-
ences therein). Simulations of < 5 mHz fluctuations in solar wind dynamic
pressure have been found not to excite cavity modes, but undergo evanescent
decay earthward of the magnetopause (Claudepierre, 2009). If waves of these
frequencies exist with the capacity to generate significant bumps on the tail
of the proton distributions, secondary waves could be generated with m
numbers beyond the observable limit of ARIES. At $f_D/N_D < 2$ mHz, m_S
is not constrained, and finite Larmor radius effects should be considered.
In such cases it could be that Alfvén modes with azimuthal wavelengths of
double the Larmor radius are favoured (see Dettrick et al. (2003)).

In a detailed case study of a single day-side event using the CUTLASS
HF radars, Yeoman and Wright (2000) split the event duration into three
intervals. During the first interval, Fourier components of 5.7 and 16 mHz
were observed, with low azimuthal wave numbers of $m = 6 \pm 3$. The second
interval contained a dominant 3.8 mHz component, with $m = -35 \pm 6$,
and the final interval was dominated by a 14.3 mHz wave, also with $m = -35 \pm 6$. The present study has neglected westward (negative m number)
waves, because the numerous and varied modes of resonance would not be
expected to show clear dispersion relation patterns. However, Yeoman and
Wright (2000) inferred the proton energies that would be required to drive
the observed westward waves through drift bounce resonance interactions.

These were $47 \pm 10\,\text{keV}$ for the second interval, and $34 \pm 10\,\text{keV}$ for the third. Agreement is found with the $35\,\text{keV}$ proton energy derived in this chapter for a $16\,\text{mHz}$ cavity mode (low m number) wave, which may have been directly observed during the first interval of the event.

A possible reason why this mechanism has been previously overlooked can be found in the early theory of drift-mirror instability (Hasegawa, 1969), in which Landau damping is assumed to be prevented by the lack of parallel electric fields. Clearly, this is not the case where drift-bounce resonance exists between waves and a particle population. That is not to say however, that other mechanisms, such as pressure anisotropy, do not play a role in the acceleration of particles, and subsequent generation of MHD waves.

Further work needs to be done with regard to the data from CAMMICE (Polar), before it can conclusively be claimed that enhancements in the magnetospheric proton distribution function occur at energies corresponding to the cavity mode frequencies, but the early results appear promising.

Other mechanisms are known to result in structured ion and electron distribution functions. Injections of energetic particles from tens to hundreds of keV are a major feature of substorms, and on reaching the day-side, dispersion can separate particles of different energies, drifting at different velocities (Liu, 2009). Loss processes may also add structure to the distribution functions. For example, Su et al. (2009) utilized the Fokker-Planck equation to show that whistler waves can scatter keV electrons into the loss

cone, with preference to certain electron energy ranges depending on the whistler frequency. However, it seems very unlikely that such a loss process would remove all but one particle energy, and thus form a bump on the tail of the distribution function, and that the bumps formed would be repeated at quantized values, as seen in the results of CAMMICE and ARIES. The mechanism of Landau damping followed by inverse Landau damping not only allows for this, but predicts the quantized energy values that match with those observed.

The sum of evidence suggests that the high m number waves observed in the morning sector cosmic noise absorption are caused by electron precipitation modulation by drift-bounce resonant toroidal MHD waves, which are generated by cavity mode waves through a process of Landau damping followed by inverse Landau damping with the magnetospheric proton population.

Opportunities for Future Research

In chapter 3 a new method is demonstrated to find the effective electron-neutral collision frequency profile in the D-region. For the period and location involved, the NRLMSISE-00 model provides values correct to within the errors of the deduced values, which are around 10%. The largest source of error is thought to in the large size, and oblique angle, of the intersecting riometer beam (IRIS beam 9). A marked improvement should be found in utilizing the high resolution ARIES riometer, which is located closer to the EISCAT radar site, and has a more comparable beam size. However, at the time of writing, accurate absolute values of absorption are unavailable, primarily due to a sensitivity of the instrument to the ambient temperature. A more certain way to increase accuracy would be to use a larger dataset, or to repeat the procedure over a number of different periods and combine the results. As a more thorough test of NRLMSISE-00, repetitions should be made at different times of the year to ensure that the model correctly represents seasonal variation.

Simulation of the deposition of X-ray energy in the ionosphere, and the corresponding electron/ion production rates, have allowed the SIC model to be extended to include the effects of X-ray solar flares. This has enabled the model to be used to estimate the D-region density profile of the highly variable NO constituent. It is likely that the largest source of error associated with this estimate stems from the knowledge, or lack thereof, of the underlying particle precipitation. At the active times often surrounding solar flares, this can be especially variable. In-situ measurements of NO, or a better awareness of the coincident particle precipitation, would help to determine the accuracy of the model results.

The generation mechanism of high m number waves, described in chapter 5, provides a number of opportunities for future research. Events are observed following a minimum level of geomagnetic activity, $(ap \geq 5)$, and the level of activity above this minimum correlates with the MLT distribution of events. Possible reasons for this behaviour are discussed within the chapter. Other unresolved questions concern the existence of high m number waves beyond the range of ARIES observation: are they restricted to L-values near ARIES, and what is their extent in radial distance? Are low frequency cavity modes in the night-side capable of generating waves with m numbers beyond the spatial aliasing limit of ARIES? What is the lower bound in driving wave frequency, below which the gradient of the proton distribution function precludes a significant bump-on-the-tail? In order to find answers it will be necessary to conduct case studies combining high resolution riometer data with in-situ particle measurements from satellites.

Bibliography

Abhyankar, K.D., "A Survey of the Solar Atmospheric Models" , *Bull. Astr. Soc. India* **5**, (1977): 40–44.

Acuña, M.H. et al., "The global geospace science program and its investigations" , *Space Sci. Rev.,* **71**, (1995): 5–21.

Allan, W. and Poulter, E.M., "The spatial structure of different ULF pulsation types: A review of STARE radar results" *Rev. Geophys. and Space Phys.,* **22**, (1984): 85–97.

Allan, W. et al., "Large m waves generated by small m field line resonances via the non-linear Kelvin-Helmholtz instability" , *J. Geophys. Res.,* **102**(A9), (1997): 19927–19934.

van Allen, J.A. and Frank, L.A., "Radiation Around the Earth to a Radial Distance of 107,400 km" *Nature,* **183**(4659), (1959): 430–434.

Akasofu, S., "The development of the auroral substorm" , *Planet. Space Sci.,* **12**(4), (1964): 273–282.

Akasofu, S., "Energy coupling between the solar wind and the magnetosphere" , *Space Sci. Rev.,* **28**, (1981): 121.

Baddeley, L.J. et al., "Morning sector drift-bounce resonance driven ULF waves observed in artificially induced HF radar backscatter" , *Ann. Geophysicae,* **20**, (2002): 1487–1498.

Baddeley, L.J. et al., "A statistical study of the unstable particle populations in the global ring current and their relation to the generation of high m ULF waves." , *Ann. Geophysicae,* **22**, (2004): 4229–4241.

Bailey, S.M. et al., "Measurements of the solar soft X-ray irradiance by the Student Nitric Oxide Explorer: First analysis and under-flight calibrations" , *J. Geophys. Res.,* **105**, (2000): 27179–27193.

Banks, P., "Collision Frequencies and Energy Transfer" , *Planet. Space Sci.,* **14**, (1966): 1085–1103.

Barakat, A.R. et al., "Ion escape fluxes from the terrestrial high-latitude ionosphere" , *J. Geophys. Res.,* **92**, (1987): 12255–12266.

Baron, M., "EISCAT Progress 1983-1985" , *J. Atmos. Terr. Phys.,* **48**, (1986): 767–772.

Bartels, J. et al., "The three-hour range index measuring geomagnetic activity" , *Geophys. Res.,* **44**, (1939): 411–454.

Barth, C.A., "Nitric oxide in the lower thermosphere" , *Planet. Space Sci.,* **40**, (1992): 315–336.

Barth, C.A., "Reference models for thermospheric nitric oxide, 1994" , *Adv. Space Res.,* **18**, (1996): 179–208.

Barth, C.A. et al., "Global observations of nitric oxide in the thermosphere" , *J. Geophys. Res.,* **108**(A1), (2003) doi:10.1029/2002JA009458.

Barth, C.A. and Bailey, S.M., "Comparison of a thermospheric model with student nitric oxide explorer (SNOE) observations of nitric oxide" , *J. Geophys. Res.,* **109**(2003JA010227), (2004).

Bastian, T.S. et al., "Radio Emission from Solar Flares" , *Annual Review of Astronomy and Astrophysics,* **36**, (1998): 131–188.

Berger, M. J. et al., "XCOM: Photon Cross Sections Database" , *http://physics.nist.gov/PhysRefData/Xcom/Text/XCOM.html* , (Copyright by the United States Secretary of Commerce, 1998).

Boyd, T.J.M. and Sanderson, J.J., "The Physics of Plasmas" *Cambridge University Press, Cambridge, UK.,* (2003).

Brodrick, D. et al., "X-ray magnitude of the 4 November 2003 solar flare inferred from the ionospheric attenuation of the galactic radio background" , *J. Geophys. Res.,* **110**, doi:10.1029/2004JA010960, (2005).

Browne, S. et al., "An Imaging Riometer for Ionospheric Studies" , *J. Elect. Comm. Eng.,* **7**, (1995): 209–217.

Bush, B.C. and Chakrabarti, S., "Analysis of Lyman α and He I 584-A airglow measurements using a spherical radiative transfer model" , *J. Geophys. Res.,* **100**, (1995): 19609–19625.

Butler, J. and Lowe R., "Beam-forming matrix simplifies design of electronically scanned antennas" , *Electron. Des.,* **9**, (1961): 170–173.

Callis, L.B. and Lambeth, J. D., "NOy formed by precipitating electron events in 1991 and 1992: Descent into the stratosphere as observed by ISAMS" , *Geophys. Res. Lett.,* **25**, (1998): 1875–1878.

Carpenter, D.L. et al., "Plasmasphere dynamics in the duskside bulge region: A new look at old topic" , *J. Geophys. Res.,* **98**(A11), (1993): 19243–19271.

Castel, F., "Arecibo: Celestial Eavesdropper" , *space.com http://www.space.com/scienceastronomy/astronomy/arecibo_profile_000508.html* (2000).

Chapman, S., Cowling, T.G., "The Mathematical Theory of Non-Uniform Gases" , *Cambridge Uni. Press.,* (1970)

Chappell, C.R. et al., "A study of the influence of magnetic activity on the location of the plasmapause as measured by OGO 5" , *J. Geophys. Res.,* **75**, (1970): 50–56.

Chen, Z.S. et al., "Ionospheric scintillation of cosmic radio noise" , *Chinese Journal of Space Science,* **12**(3), (1992): 192–204.

Cheng, C.C. et al., "Evidence of the Coupling of a Fast Magnetospheric Cavity Mode to Field Line Resonances" , *Earth Planets Space,* **50**, (1998): 683–697.

Chisham, G., "Giant Pulsations: An Explanation for Their Rarity and Occurrence During Geomagnetically Quiet Times" , *J. Geophys. Res.,* **101**, (1996): 24755.

Claudepierre, S.G. et al., "Solar wind driving of magnetospheric ULF waves: Pulsations driven by velocity shear at the magnetopause" , *J. Geophys. Res.,* **113**, (2008): A05218.

Claudepierre, S.G. et al., "Magnetospheric cavity modes driven by solar wind dynamic pressure fluctuations" , *Geo. Res. Let.,* **36**, (2009): L13101.

Coroniti, F.V. and Kennel, C.F., "Electron precipitation pulsations" , *J. Geophys. Res.,* **75**, (1970): 1279–1289.

Cowley, S.W.H., "The structure and length of tail-associated phenomena in the solar wind downstream from Earth" , *Planet. Space Sci.,* **39**, (1991): 1039.

Culhane, J.L. and Acton, L.W, "A simplified thermal continuum function for the X-ray emission from coronal plasmas" , *Mon. Not. R. astr. Soc.* **151**, (1970): 141–147.

Danielson, E.W. et al., "Meteorology" , *McGraw-Hill Education, ISBN 0-07-242072-3,* (2003).

Davies, K., "Ionospheric Radio Propagation" , *Dover Publications Inc., New York.,* (1966).

Davies, K., "Ionospheric Radio" , *Peter Peregrinus Ltd.,* (1990).

Dettrick, S. et al., "Kinetic theory of geomagnetic pulsations: 4.Hybrid gyrokinetic simulation of drift-bounce resonant excitation of shear Alfvén waves" , *J. Geophys. Res.,* **108**(A4), (2003): 1150.

Detrick, D.L. and Rosenberg T.J., "A phased-array radiowave imager for studies of cosmic noise absorption" , *Radio Sci.,* **25**(4), (1990): 325–338.

Dobbin, A.L. et al., "3-D GCM modelling of thermospheric nitric oxide during the 2003 Halloween storm" , *Ann. Geophysicae,* **24**, (2006): 2403–2412.

Drob, D.P., Picone, J.M, "Statistical Performance Measures of the HWM-93 and MSISe-90 Empirical Atmospheric Models and the Relation to Infrasonic CTBT Monitoring" , *22nd Annual Seismic Research Symposium, New Orleans, Louisiana, USA.,* (2000).

Dulk, G.A., "Radio emission from the sun and stars" , *Annual review of astronomy and astrophysics, Palo Alto, CA, Annual Reviews, Inc.,* **23**, (1985): 169–224.

Dungey, J.W., "Interplanetary Magnetic Field and the Auroral Zones" , *Phys. Rev. Lett.,* **6**, (1961): 47–48.

Dungey, J.W., "Electrodynamics of the outer atmospheres" , *Rep. 69, Ions. Res. Lab. Pa. State Univ., University Park,* (1954).

Ecklund, W.L., Balsley, B.B, "Long-Term Observations of the Arctic Mesosphere with the MST Radar at Poker Flat, Alaska" , *J. Geophys. Res.,* **86**, (1981): 7775–7780.

Emmert, J.T. et al., "Global Change in the Thermosphere: Compelling Evidence of a Secular Decrease in Density" , *J. Geophys. Res.,* **109**(A02301), (2004).

Enell, C.F. et al., "Case study of the mesospheric and lower thermospheric effects of solar X-ray flares: Coupled ion-neutral modelling and comparison with EISCAT and riometer measurements" , *Ann. Geophysicae,* **26**, (2008): 2311–2321.

Eriksson, P.T.I. et al., "A statistical correlation of Pc5 pulsations and solar wind pressure oscillations" , *Adv. in Space Res.,* **38**, (2006): 1763–1771.

van Eyken, T. et al., "EISCAT Scientific Association. Multi-annual report: 1998–2001" , *http://www.eiscat.se/groups/Documentation/AnnualReport/* (2001).

Feldman, U. et al., "On the sources of fast and slow solar wind" , *J. Geophys. Res.,* **110**(A02301), (2005): A07109.1–A07109.12.

Flemming, E., "On the Origin of the Cosmic Radiation" , *Physics Review,* **75**, (1949): 1169–1174.

Flemming, E.S. et al., "Monthly Mean Global Climatology of Temperature, Wind, Geopotential Height and Pressure for 0-120 km" , *NASA Technical Memorandum,* (1988): 100697.

Fukuyama, K. and Kofman, W., "Incoherent scattering of an electromagnetic wave in the mesosphere: A theoretical consideration" , *J. Geomag. Geoelectr.,* **32**, (1980): 67–81.

Fujita, S. and Itonaga, M., "A plasmaspheric cavity resonance in a longitudinally non-uniform plasmasphere" , *Earth Planets Space,* **55**, (2003): 219–222.

Garcia, H.A., "Temperature and emission measure from GOES soft X-ray measurements" , *Solar Physics,* **154**, (1994): 275–308.

Garrett, A.J.M., "Multi-species Kinetic Generalization of the Appleton-Hartree Dispersion Formula" , *J. Plasma Phys.,* **33**(2), (1985): 265–284.

Glassmeier, K.H. et al., "Concerning the Generation of Geomagnetic Giant Pulsations by Drift Bounce Resonance Ring Current Instabilities" , *Ann. Geophysicae,* **17**, (1999): 338.

Gokov, A.M. et al., "Simultaneous Measurement of the Density and Frequency of Electron Collisions with Molecules in the Ionospheric D-region" , *Radiophys. and Quantum Elec.,* **34**(3), (1991): 275–277.

Grill, M. et al., "A New Imaging Riometer based on Mills Cross Technique" , *7th International Symposium on Communication Theory and Applications. Ambleside, UK.,* (July 2003): 26–31.

Grill, M., "Technological Advances in Imaging Riometry" , *PhD Thesis, University of Lancaster, UK,* (2007).

Hargreaves, J.K., "Auroral absorption of HF radio waves in the ionosphere: a review of results from the first decade of riometry" , *Proc. IEEE,* **57**(8), (1969): 1348–1373.

Hargreaves, J.K., "Conjugate and closely-spaced observations of auroral radio absorption IV" , *Earth. Planet. Space,* **18**, (1970): 1691–1705.

Hargreaves, J.K., "The solar-terrestrial environment" , *Cambridge University Press, Cambridge, UK,* (1992).

Hargreaves, J.K., "A new method of studying the relation between ionization rates and radio-wave absorption in polar-cap absorption events" , *Annales Geophysicae,* **23**(2), (2005): 359–369.

Hargreaves, J.K., "On the relations between proton influx and D-region electron densities during the polar-cap absorption event of 28-29 October 2003" , *Annales Geophysicae,* **23**(10), (2005): 3267–3276.

Harris, M.J., "A new coupled middle atmosphere and thermosphere general circulation model: Studies of dynamic, energetic and photochemical coupling in the middle and upper atmosphere" , *Ph.D. thesis, University College London, UK,* (2001).

Hasegawa, A., "Drift mirror instability in the magnetosphere" , *The Physics of Fluids,* **12**, (1969): 2642–2650.

Hastings, W.K., "Monte Carlo sampling methods using Markov chains and their applications" , *Biometrika,* **57**, (1970): 97–109.

Haugstad, B.S., "Modification of a theory of electron precipitation pulsations" , *J. Atmos. Terr. Phys.,* **27**, (1975): 257–272.

Hedin, A.E., "Extension of the MSIS Thermosphere Model into the Middle and Lower Atmospheres" , *J. Geophys. Res.,* **96**(A2), (1991): 1159–1172.

Henry, R.J.W., McElroy, M.B., "The Atmospheres of Venus and Mars" , *Gordon & Breach, New York.,* (1968): 251.

Hess, W.N., "The radiation Belt and Magnetosphere" , *Blaisdell,* (1968).

Hughes J.W., "Magnetospheric ULF waves: A tutorial with a historical perspective" , *Solar Wind Sources of Magnetospheric Ultra-Low-Frequency Waves. Geophysical Monograph 81, AGU,* (1994): 1–11.

Itikawa, Y., "Effective Collision Frequency of Electrons in Atmospheric Gases" , *Planet. Space Sci.,* **19**, (1971): 993–1007.

Jasperse, J.R., "Boltzmann-Fokker-Planck Model for the Electron Distribution Function in the Earth's Ionosphere" , *Planet. Space Sci.,* **24**, (1976): 33–40.

Kainuma, S. et al., "Drift motion of ionospheric arc-like absorption regions observed with 256-beam imaging riometer in Alaska" , *Earth. Planet. Space,* **53**, (2001): 753–760.

Kikuchi, T., "Eastward propagation of Pc4-5 range CNA pulsations in the morning sector observed with scanning narrow beam riometer at L = 6.1" , *Geo. Res. Let.,* **15**, (1988): 168–171.

Kim, Y.K. et al., "Electron-impact cross sections for ionization and excitation" , *http://www.nist.gov/physlab/data/ionization/index.cfm* , (Copyright by the United States Secretary of Commerce, 2010).

King, J.H. and Papitashvili, N.E., "Solar wind spatial scales in and comparisons of hourly Wind and ACE plasma and magnetic field data" , *J. Geophys. Res.,* **110**(A2), (2005): A02209.

Kivelson, M.G. and Russel, C.T., "Introduction to Space Physics" , *Cambridge University Press, UK,* (1995).

Kivelson, M.G. and Bagenal, F., "Planetary magnetospheres" , *The Encyclopedia of the Solar System, Academic Press,* (1998): 477.

Kopp, G. et al., "The Total Irradiance Monitor (TIM): Science Results" , *Solar Physics,* **20**, (2005): 129–139.

Koskinen, H.E.J. and Tanskanen, E.I., "Magnetospheric energy budget and the epsilon parameter" , *J. Geophys. Res.,* **107**(A11), (2002): 1415.

Lee, D.H. et al., "Effects of Ionospheric Damping on MHD Wave Mode Structure" , *Earth Planets Space,* **56**, (2004): e33–e36.

Lemaire, J., "A brief panorama" , *Advances in Space Research,* **2**(1), (1982): 3–10.

Leonovich, A.S. et al., "Magnetosonic resonance in a dipole-like magnetosphere" , *Ann. Geophysicae,* **24**, (2006): 2277–2289.

Leonovich, A.S. and Mazur, V.A., "On the spectrum of magnetosonic eigenoscillations of an axisymmetric magnetosphere" , *J. Geophys. Res.,* **106**, (2001): 3919–3928.

Little, C.G. and Leinbach, H., "The riometer – a device for the continuous measurement of ionospheric absorption" , *Proc. IRE,* **147**, (1959): 315–320.

Liu, W.L. et al, "Observation and modeling of the injection observed by THEMIS and LANL satellites during the 23 March 2007 substorm event" , *J. Geophys. Res.,* **114**, (2009): doi:10.1029/2008JA013498.

Maeda, S. et al., "Heat budget of the thermosphere and temperature variations during the recovery phase of a geomagnetic storm" , *J. Geophys. Res.,* **97**(A10), (1992): 14947–14957.

Makarevitch, R.A. et al., "Imaging riometer observations of drifting absorption patches in the morning sector" , *Ann. Geophysicae,* **22**, (2004): 3461–3478.

Marple, S.R. and Honary, F., "Determination of Riometer Quiet Day Curves and Removal of Solar Radio Emissions" , *31st Annual European Meeting on Atmospheric Studies by Optical Methods and 1st International Riometer Workshop. Ambleside, UK,* (2004): 46.

McIlwain C.E., "Coordinates for mapping the distribution of magnetically trapped particles" , *J. Geophys. Res.,* **66**, (1961): 3681–3691.

Menk, F.W. et al., "Coordinated observations of forced and resonant field line oscillations at high latitudes." , *ANARE Rep. Australian Antarctic Division,* **146**, (2001): 383–404.

Miyazaki, S., "Relation between Lower Ionospheric Electron Density Profiles and Cosmic Noise Absorption during Auroral Zone Disturbances" , *J. Geomag. Geoelectr.,* **27**, (1975): 113–129.

Mlynczak, M. et al., "The natural thermostat of nitric oxide emission at 5.3 μm in the thermosphere observed during the solar storms of April 2002" , *Geophys. Res. Lett.,* **30**(21), (2003): 2100.

Morrison, M. et al., "Ultrasimple Calculation of Very Low Energy

Momentum-Transfer and Rotational-Excitation Cross Sections: $e - N_2$ Scattering" , *Physical Review A.,* **55**(4), (1997): 2786–2798.

Nosé, M. et al., "Electron precipitation accompanying Pc 5 pulsations observed by the DE satellites and at a ground station" , *J. Geophys. Res.,* **103**(A8), (1998): 17587–17604.

Nagata, T. et al., "Geomagnetically conjugate relationships of giant pulsations at Syowa Base, Antartica, and Reykjavik, Iceland" , *J. Geophys. Res.,* **68**, (1963): 4621.

Nakamura, R., "Substorms and their solar wind causes" , *Space Science Reviews,* **124**, (2006): 91–101.

Nielsen, E., "Dynamics and spatial scale of auroral absorption spikes associated with the substorm expansion phase" , *J. Geophys. Res.,* **85**, (1980): 2092–2098.

Pant, T.K. and Sridharan, R., "A case-study of the low-latitude thermosphere during geomagnetic storms and its new representation by improved MSIS model" , *Ann. Geophysicae,* **16**, (1998): 1513–1518.

Picone, J.M. et al., "NRLMSISE-00 Empirical Model of the Atmosphere: Statistical Comparisons and Scientific Issues" , *J. Geophys. Res.,* **107**(A12), (2002): 1468.

Piddington, JH., "Cosmic electrodynamics" , *Wiley-Interscience,* (1969).

Press, W.H. et al., "Numerical Recipes in C, Second Edition" , *Cambridge Uni. Press,* (1992).

Press, W.H. et al., "Numerical Recipes in Fortran 77, Second Edition" , *Cambridge Uni. Press,* (1996).

Rae, I.J. et al., "Equator-S observations of drift mirror mode waves in the dawnside magnetosphere" , *J. Geophys. Res.,* **112**, (2007): A11203.

Ravishankara, A.R. et al., "Nitrous Oxide (N2O): The Dominant Ozone-Depleting Substance Emitted in the 21st Century" , *Science,* **326**, (2009): 123.

Rees, M.H., "Physics and Chemistry of the Upper Atmosphere" , *Cambridge University Press, Cambridge, UK,* (1989).

Reid, G.C., "Polar-Cap Absorption – Observations and Theory" , *Fundamentals of Cosmic Physics.,* **1**, (1974): 167–202.

Rishbeth, H. and Williams, P.J.S., "The EISCAT ionospheric radar - The system and its early results" , *Royal Astronomical Society, Quarterly Journal (ISSN 0035-8738)* **26**, (1985): 478–512.

Roble, R.G. et al., "On the global mean structure of the thermosphere" , *J. Geophys. Res.,* **92**, (1987): 8745.

Rusch, D.W. and Barth, C.A., "Satellite measurements of nitric oxide in the polar region" , *J. Geophys. Res.,* **80**, (1975): 3719–3721.

Saetre, C. et al., "Energetic electron precipitation and the NO abundance in the upper atmosphere: A direct comparison during a geomagnetic storm" , *J. Geophys. Res.,* **109**(A09), (2004): 302.

Saetre, C. et al., "Thermospheric nitric oxide at higher latitudes: Model calculations with auroral energy input" , *J. Geophys. Res.,* **112**(A08), (2007): 306.

Samson, J.C. et al., "Magnetometer and radar observations of magnetohydrodynamic cavity modes in the Earths magnetosphere" , *Can. J. Phys.,* **69**, (1991): 929–937.

Samson, J.C. and Rankin, R., "The Coupling of Solar Wind Energy to MHD Cavity Modes, Waveguide Modes, and Field Line Resonances in the Earth's Magnetosphere" , *Solar Wind Sources of Magnetospheric Ultra-Low-Frequency Waves. Geophysical Monograph 81, AGU,* (1994): 253–264.

Schunk, R.W., Nagy, A.F., "Electron Temperatures in the F Region of the Ionosphere: Theory and Observations" , *Rev. Geophys. and Space Phys.,* **16**(3), (1978): 355–399.

Sen, H.K., Wyller, A.A., "On the Generalization of the Appleton-Hartree Magnetoionic Formulas" , *J. Geophys. Res.,* **65**(12), (1960): 3931–3950.

Senior, A. and Honary, F., "Observations of the spatial structure of electron precipitation pulsations using an imaging riometer" , *Ann. Geophysicae,* **21**(4), (2003): 997–1003.

Seppälä, A. et al., "Arctic and Antarctic polar winter NOx and energetic particle precipitation in 20022006" , *Geophys. Res. Lett.,* **34**(12), (2007): 810.

Serafimova, M., Serafimov, K., "On a Possibility for Continuous Ground-Based Measurements of the Collision Frequency in the Ionosphere" , *B'lgarska Akademiia na Naukite, Dokladi.,* **44**(10), (1991): 35–38.

She, C.Y. et al., "Vertical structure of the midlatitude temperature from stratosphere to mesopause (30-105 km)" , *Geophys. Res. Lett.,* **22**(4), (1995): 377–380.

Shimazaki, T., "Minor Constituents in the Middle Atmosphere" , *Developments in Earth and Planetary Physics, D. Reidel Publishing Company,* **6**, (1984).

Shin'ichi, W. et al., "Comparison between F10.7 and E10.7 Indices using Upper-atmosphere Models" , *Proceedings of the Space Sciences and Technology Conference,* **46**(2), (2002): 510–513.

Sibeck, D.G. et al., "Solar wind dynamic pressure variations and transient magnetospheric signatures" , *Geo. Res. Let.,* **16**, (1989): 13–16.

Siskind, D.E. et al., "The Response of Thermospheric Nitric Oxide to an Auroral Storm: 2. Auroral Latitudes" , *J. Geophys. Res.,* **94**(A12), (1989): 16899–16911.

Siskind, D.E. et al., "Two-dimensional model calculations of nitric oxide transport in the middle atmosphere and comparison with Halogen Occultation Experiment data" , *J. Geophys. Res.,* **102**, (1997): 3527–3546.

Siskind, D.E. et al., "A climatology of nitric oxide in the mesosphere and thermosphere" , *Adv. Space Res.,* **21**, (1998):1353–1362.

Solomon, J., "Drift of particles and wave-particle interactions" , *The magnetospheres of the earth and Jupiter; Proceedings of the Neil Brice Memorial Symposium, Frascati, Italy, May 28-June 1, 1974. Dordrecht, D. Reidel Publishing Co.,* (1975): 153–159.

Southwood, D. et al., "Bounce Resonant Interaction Between Pulsations and Trapped Particles" , *Planetary Space Science,* **17**, (1969): 349–361.

Southwood, D.J. and Kivelson, M.G., "Charged particle behavior in low-frequency geomagnetic pulsations. II - Graphical approach" , *J. Geophys. Res.,* **87**, (1982): 1707–1710.

Spanswick E. et al., "Pc5 modulation of high energy electron precipitation: particle interaction regions and scattering efficiency" , *Ann. Geophysicae,* **23**, (2005): 1533–1542.

Su, Z. et al., "Evolution of electron pitch angle distribution due to interactions with whistler mode chorus following substorm injections" , *J. Geophys. Res.,* **114**, (2009): doi:10.1029/2009JA014269.

Sullivan, J.P. et al., "Low Energy Electron Scattering from O_2" , *J. Phys B: At. Mol. Opt. Phys.,* **28**, (1995): 4319–4328.

Svalgaard, L. and Hudson, H.S., "The Solar Microwave Flux and the Sunspot Number" , *SOHO23 Conference Proceedings, Astronomical Society of the Pacific,* arXiv:1003.4281v1 [astro-ph.SR], (submitted: 22 March 2010)

Sylwester, J. et al., "Quantitative interpretation of GOES soft X-ray measurements" , *Astronomy and Astrophysics,* **293** (1995): 577–585.

Tereshchenko V.D. et al., "Modeling of the D-region behavior in the polar ionosphere during the solar flare of April 5, 2004" , *Geomagnetism and Aeronomy,* **47**(4), (2007): 496–501.

Thomas, L.D. and Nesbet, R.K., "Low Energy Electron Scattering by Atomic Oxygen" , *Physical Review A.,* **12**(4), (1975): 1729–1730.

Thomson, N. R. et al., "Ionosphere gives size of greatest solar flare" , *Geophys. Res. Lett.,* **31**, (2004): 6803.

Tobiska, W., et al., "The SOLAR2000 empirical solar irradiance model and forecast tool" , *J. Atmos. Sol. Terr. Phys.,* **62**, (2000): 1233–1250.

Tsyganenko, N.A., "A model of the near magnetosphere with a dawn-dusk asymmetry. 1. Mathematical structure" , *J. Geophys. Res.,* **107**, (2002a): 1179.

Tsyganenko, N.A., "A model of the near magnetosphere with a dawn-dusk asymmetry. 2. Parametrization and fitting to observations" , *J. Geophys. Res.,* **107**, (2002b): 1176.

Tu, C.Y. et al., "Solar Wind Origin in Coronal Funnels" , *Science,* **308**, (2005): 519.

Turner, N.E. et al., "A two-dimensional model of thermospheric nitric oxide sources and their contributions to the middle atmospheric chemical balance" , *J. Atmos. Sol.-Terr. Phys.,* **71**, (2009): 1023–1031.

Turunen, E., "High latitude D-region studies by incoherent scatter radar

measurements" , *Ph.D. thesis, Report No.52, Sodankylä Geophysical Observatory, Finland,* (1993).

Turunen, E., et al., "D-Region Ion Chemistry Model" , *STEP Handbook of Ionospheric Models, edited by Schunk, R. W., Scientific Committee on Solar-Terrestrial Physics* (1996): 1–25.

Ulich, T. et al., "EISCAT 3D: the European three-dimensional imaging radar for atmospheric and geospace research" , *COSPAR Scientific Assembly, Bremen, Germany.* (2010).

Verronen, P.T. et al., "Diurnal variation of ozone depletion during the OctoberNovember 2003 solar proton event" , *J. Geophys. Res.,* **110**(A09S32), (2005).

Verronen, P.T., "Ionosphere-atmosphere interaction during solar proton events" , *Ph.D. thesis, Finnish Meteorological Institute, Finland,* ISBN: 951-697-650-6, (2006).

Vitt, F.M. et al., "A two-dimensional model of thermospheric nitric oxide sources and their contributions to the middle atmospheric chemical balance" , *J. Atmos. Sol.-Terr. Phys.,* **62**, (2000): 653–667.

Vuthaluru, R.A. et al., "Collision Frequencies in the D-region" , *J. Atmos. Sol. Terr. Phys.,* **64**, (2002): 2043–2054.

Walt, M., "Introduction to Geomagnetically Trapped Radiation" , *Cambridge University Press, UK,* ISBN 9780521431439, (1994).

Wilken, B. et al., "Magnetospheric ion composition spectrometer aboard the CCRES spacecraft" , *J. Spac. Rock.,* **29**, (1992): 585–591.

Williams, D.R., "Sun Fact Sheet" , *NASA. http://nssdc.gsfc.nasa.gov/planetary/factsheet/sunfact.html* (2004).

Wilson, R.C. et al., "Observations of solar irradiance variability" , *Science,* **211**, (1981): 700.

Woods, T.N. et al., "Early results from the TIMED solar EUV experiment" , *4th (Virtual) Thermospheric/Ionospheric Geospheric Research (TIGER) Symposium, Fraunhofer Institute for Physical Measurement Techniques,* (2002).

Woolfson, M., "The origin and evolution of the solar system" , *Astronomy and Geophysics,* **41**, (2000): doi: 10.1046/j.1468-4004.2000.00012.x

Yeoman T.K. and Wright D.M., "ULF Waves with Drift Resonance and Drift-Bounce Resonance Energy Sources as Observed in Artificially-Induced HF Radar Backscatter" , *Annales Geophysicae,* **19**, (2000): 159-170.

Yumoto, K. et al., "Global Cavity Mode-Like and Localized Field-Line Pc 3-4 Oscillations Stimulated by Interplanetary Impulses (Si/Sc): Initial Results From the 210° MM Magnetic Observations" , *Solar Wind Sources of Magnetospheric Ultra-Low-Frequency Waves. Geophysical Monograph 81, AGU,* (1994): 335–344.

Xu, J. et al., "Mesopause structure from Thermosphere, Ionosphere, Mesosphere, Energetics, and Dynamics (TIMED)/Sounding of the Atmosphere

Using Broadband Emission Radiometry (SABER) Observations" , *J. Geophys. Res.,* **112**(D9), (2007): D09102.

Zinn, J. et al., "The solar flare of August 18, 1979 – Incoherent scatter radar data and photochemical model comparisons" , *J. Geophys. Res.,* **95**, (1990): 16705–16718.